Ludwig-Maximilians-Universität München

Magnetic properties of iron-nickel alloys under high pressure with relevance to planetary cores

Dissertation
zur Erlangung des Doktorgrades
der Fakultät für Geowissenschaften der
Ludwig-Maximilians-Universität München

vorgelegt von
Qingguo Wei

am
01. 04. 2015

1. Gutachter: Prof. Dr. Stuart Gilder
2. Gutachter: Prof. Dr. Christian Pfleiderer
Tag der mündlichen Prüfung: 17.07.2015

Summary

This dissertation explores the effects of pressure on the magnetic remanence of iron-nickel and iron-silicon alloys relevant to the solid inner cores of the terrestrial planets and Earth's moon. The Earth's inner core likely comprises mostly pure iron in a hexagonal close packed (*hcp*) structure. Experiments on pure iron powder and foil were carried out up to 21 GPa at room temperature. The most important conclusion from this work is that either *hcp*-iron is ferromagnetic or that a poorly understood, intermediate *hcp* phase of iron is ferromagnetic. It was also determined that the results must be corrected for magnetic shape anisotropy, which is related either to the original sample material (foil) or how the bulk sample volume changes shape due to increasing oblateness of the chamber during pressurization. Fe-Ni alloys in the face centered cubic (*fcc*) phase with compositions around $Fe_{64}Ni_{36}$, called Invar, exhibit near-null thermal expansion, making them useful for technological applications. Models explaining the Invar effect evoke magnetovolume effect that compensate for thermal expansion. Previous work suggested that the Curie temperature of $Fe_{64}Ni_{36}$ decreases 35 K per GPa, which predicts that around 5 GPa, $Fe_{64}Ni_{36}$ will turn paramagnetic. Our experiments on $Fe_{64}Ni_{36}$ found a marked decrease in magnetization between 5-7 GPa, consistent with former studies, but that it remains ferromagnetic until 16 GPa. The magnetic remanence of low Ni Invar alloys increases faster with pressure than for other body-centered-cubic compositions due to the higher magnetostriction of the low Ni Invar metals. Experimental results on body centered cubic (*bcc*) Fe-Ni alloys match well with those for pure iron-- again leading to the conclusion that either an intermediate *hcp* phase, or that the *hcp* phase itself, is ferromagnetic. The ubiquitous enhancement in magnetization under pressure, or during pressure release, of the Fe-Ni and Fe-Si alloys is associated with strain-induced martensitic effects. Finally, a defocused laser heating technique was developed to measure the Curie temperature in diamond or moissanite anvil cells. Preliminary results on titanomagnetite ($Fe_{2.4}Ti_{0.6}O_4$) are broadly consistent with previous work.

Contents

List of Figures

List of Tables

Acknowledgments

I would like to give thanks to many people for their support about this dissertation:

- First, I thank Prof. Dr. Stuart Gilder, who gave me the opportunity to do this research. With his guidance I was able to create this thesis.
- Fe-Ni alloys synthetic support from Dr. Werner Ertel-Ingrisch; X-ray analysis support from Prof. Wolfgang Schmahl, Dr. Bernd Maier and Dr. Sohyun Park; sample SEM analysis from Prof. Karl Thomas Fehr; experiments help from master student Nicolas Zander; mechanical support from the workshop group are highly appreciated.
- In addition, I thank my colleagues in our research group Linder Julia, Mao Xuegang, Wack Michael, Volk Michael, Eitel Michael, Zhao Xiangyu, Lhuillier Florian, Cheng Yanjun, and He Kuang, e.g. I am very glad to study with them.
- I thank my parents for their encouragement; and special thanks give to my wife Zhang Yan who is accompanying me in Germany and gave birth and taking care of our lovely daughter Wei Xinyi.

Introduction and Outline

Introduction

Iron is one of the most widely used elements in human life, which spawned the so-called "iron age" of human civilization. The main reason for this is that iron is abundant in nature, and has a relatively high hardness and strength. Another fascinating property of iron is that it is ferromagnetic-- most of the magnetic materials encountered by humans are related to iron. Since the last century, the magnetic properties of iron have been the subject of intense research because of its widespread usage and the high demand for better magnets.

The magnetic field of the Earth resembles a dipole field that emanates from a bar magnet. Mercury also has an internally-generated magnetic field, yet its total field intensity is much weaker than the Earth (surface fields on Earth= 50 μT; Mercury= 0.3 μT). Venus, Mars and Earth's Moon have no internally-generated magnetic fields today, yet surface rocks on Mars and the Earth's Moon possess remnant magnetizations, implying that these bodies likely had internally-generated magnetic fields in the past.

It is broadly accepted that magnetohydrodynamic processes in the Earth's core generate the Earth's magnetic field. Moreover, it is widely assumed that the solid inner core material is paramagnetic at the high pressure/temperature conditions in planetary cores, where temperatures well exceed the Curie temperature of iron. But the fact is that very few experimental results exist to constrain the magnetic properties of iron alloy materials at core conditions. The goal of this thesis is to measure the magnetic properties of iron alloys relevant to the solid inner cores of the terrestrial planets.

Chondritic meteorites, which represent the composition of the solar nebula, contain ~18.4 wt% Fe (White, 2013). Through differentiation of chondritic material during planetary formation, iron will sink into the planet's center, forming a core. Iron meteorites thus serve as proxies for the core material of former planets. For terrestrial planets and the moon, metallic cores comprise a significant portion (Figure 0.1) of the total volume (Sohl and Schubert, 2007). The radius of the

Earth's core is 3486 km (radius of solid inner core 1216 km), hence 16% of Earth’s volume and 33% of Earth’s mass; Venus is slightly smaller than the Earth, 85% of Earth’s volume, and is believed to have a similar structure as Earth; the volume of core to planet is about 12.5% for Mars and 42% for Mercury; volume of core to the moon is about 0.1%. Earth’s solid inner core is thought to be slowly growing from liquid outer core due to the gradual cooling of the Earth’s interior. Earth’s solid inner core is believed to consist primarily of iron-nickel alloy; and liquid outer core is believed to have more light elements.

Iron is the major, but not the only, element in cores. Nickel concentrations in iron meteorites vary from 5 and 60 wt%-- most are between 5 and 12 wt% (Albertsen et al., 1983). Seismological, experimental and theoretical calculations show that the density of Earth’s outer core is ~10% lower than the density of iron at the core pressure and temperatures (Anderson and Isaak, 2002; Birch, 1952, 1964; Jeanloz, 1979; Mao et al., 1990), which means the Earth’s outer core should have lighter elements than iron-- H, C, O, S, Si and P are potential candidates (McDonough and Sun, 1995; Poirier, 1994; Vocadlo, 2013), with cosmochemical abundances and metallurgical solubility being the major consideration. Among them, Si and S are preferred, because of their relative depletion in Earth’s silicates (Allègre et al., 1995; Georg et al., 2007; Javoy, 1995), which indicates that some silicon and sulfur entered into the core. The depleted Si could be present in Earth’s core as high as 14.4 wt % (Wanke and Dreibus, 1988). The MESSENGER satellite mission to Mercury found 1-4 wt% FeO and S on the surface, suggesting the core of Mercury could be composed of Fe-Si-S (Chabot et al., 2014) in order to achieve equilibrium with silicate melts. A sulfur content of 14% in Martian meteorites also suggests sulfur is a major alloying element in Mars’ core.

We chose pure iron as a standard reference for the terrestrial planets’ cores, as well as Fe-Ni alloys with Ni compositions between 5-20 % (*bcc* structure), which is the common composition in iron meteorites; Fe-Ni alloys (*fcc* structure) with Ni composition between 30-60 % are chosen as core materials in the *fcc* structure (Mars, Mercury and the moon). Fe-Si alloys with Si compositions between 5-20% were also chosen as potential core material for Mercury and Mars. Fe-S alloys were not studied in this thesis, although S has been suggested as an alloying element in some cores. Fe-S alloys are unstable at room temperature, which makes working with them problematic.

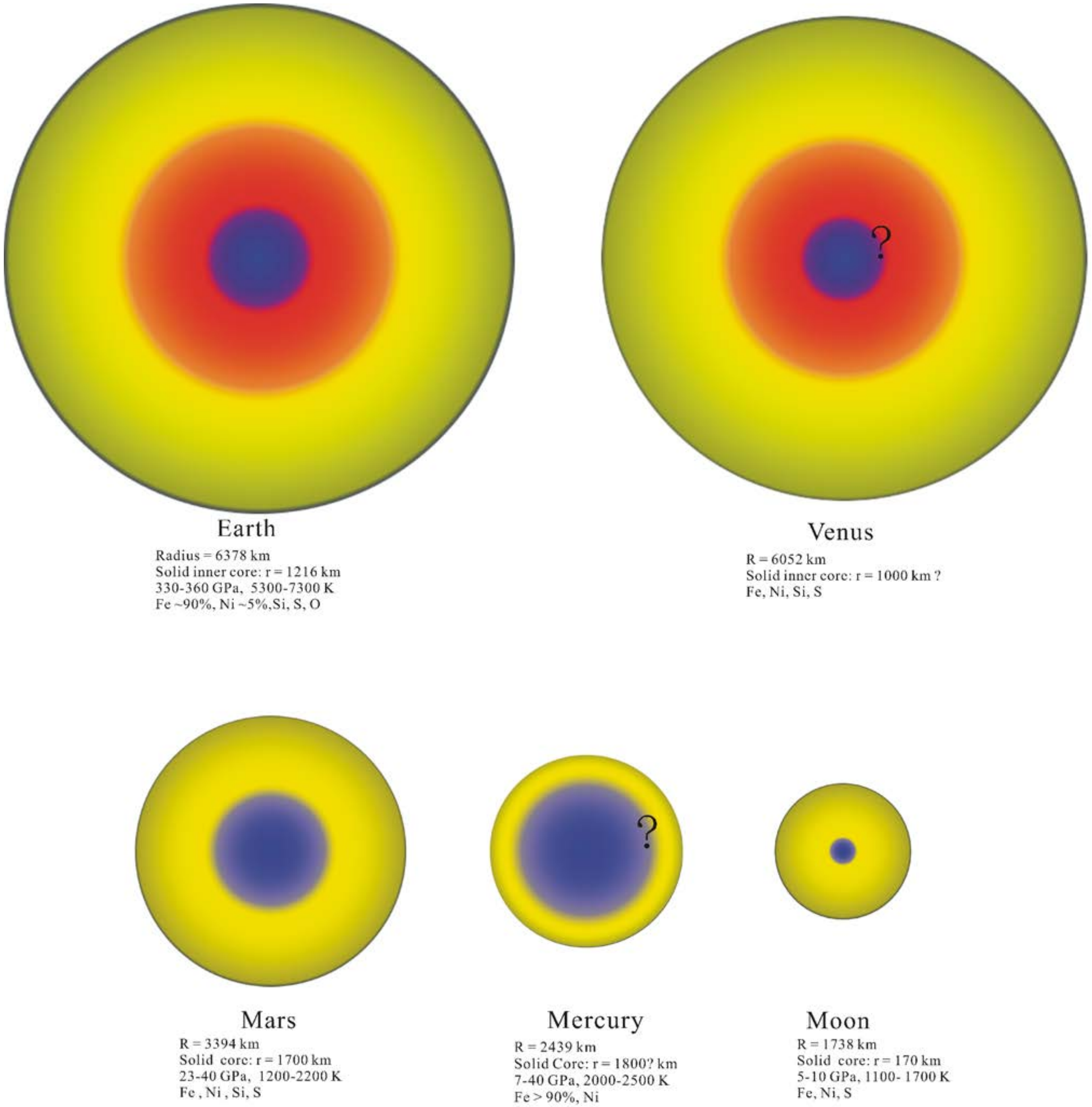

Figure 0.1 Interior structure of Mercury, Venus, Earth, Mars and the moon. Information from (Alfè et al., 2007; Bullen, 1952, 1973; Melchior, 1986; Monnereau et al., 2010; Stevenson, 1981).

Because magnetism and the crystallographic structure of a material are related through electron exchange between atoms, structural changes induced by pressure modify the crystal lattice, which in turn influences magnetic properties. At ambient conditions, iron has a body-centered cubic (*bcc*) structure (Figure 0.2); it transforms to a hexagonal-close-packed (*hcp*) structure at 13 GPa (Takahashi and Bassett, 1964) at room temperature; iron transforms to a face-centered cubic (*fcc*) crystal structure at ambient pressure at temperatures >1183 K (Figure 0.2). The phase diagram of iron changes with the addition of alloying elements (nickel, silicon and sulfur). Nickel expands the stability range of the *fcc* phase (Huang et al., 1988; Kuwayama et al., 2008) and lowers the *bcc* to *hcp* transition pressure at room temperature. Silicon can largely increase the stability range of the *bcc* phase up to 80 GPa (Hirao et al., 2004; Lin et al., 2002).

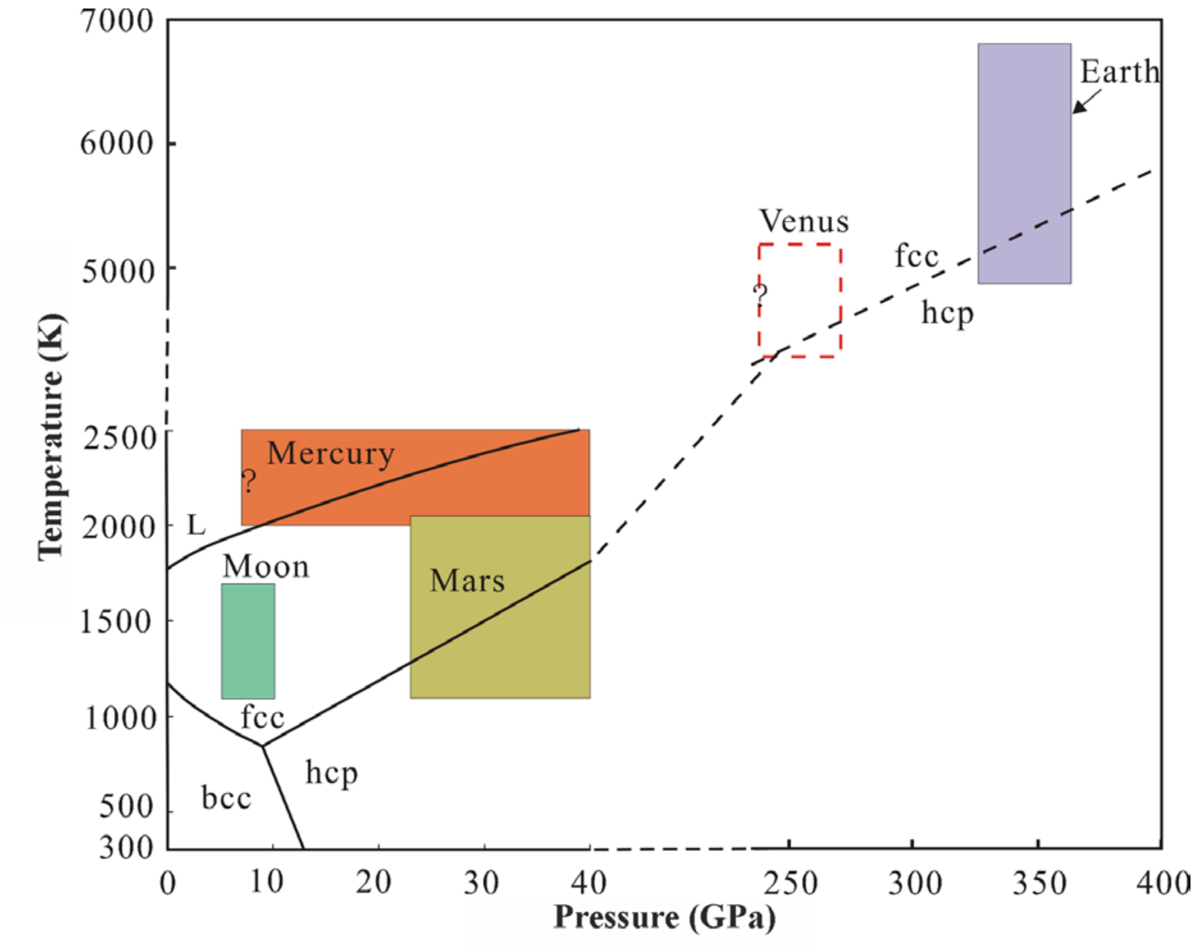

Figure 0.2 Phase diagram of iron. Modified from (Tateno et al., 2010) with approximate P-T conditions for solid cores of Mercury, Venus, Earth, Mars, and the moon.

Pressure at the Earth's inner core is 330-360 GPa with temperatures exceeding 5000 K (Anzellini et al., 2013). The phase of iron in Earth's inner core is debated. Several studies concluded that the *hcp* phase is the best candidate (Brown and McQueen, 1986; Mao et al., 1990; Merkel, 2000; Tateno et al., 2012; Tateno et al., 2010), while others argue for *bcc* or double hexagonal closed packed phase (Andrault, 1997; Boehler, 1993; Dubrovinsky et al., 2007; Dubrovinsky et al., 2000a).

Experiments with iron alloyed with 4% and 10% nickel that attained Earth's inner core pressures at both room temperature and 4700 K identified the stable structure as hcp (Tateno et al., 2012). The phase of iron in Venus's inner core is largely unknown; it is probable that iron is in the *fcc* phase in the solid cores of Mercury and Moon (Jackson et al., 2013; Siegfried and Solomon, 1974; Wieczorek, 2006); *fcc* and *hcp* phases may both exist in the core of Mars (Stevenson, 2001). Among the *bcc*, *fcc* and *hcp* phases, the magnetic properties of the *hcp* phase is the most debated yet is of the greatest relevance to the Earth's core.

Probing the magnetic properties of samples under high pressure is challenging: there are both direct and indirect measurements to do so. For indirect measurements, Mössbauer spectroscopy is commonly used to study the magnetic moment at the nucleus, which causes hyperfine splitting (Pipkorn et al., 1964; Taylor, 1982). X-ray magnetic circular dichroism, X-ray absorption spectroscopy and X-ray emission spectroscopy (Baudelet et al., 2005; Rueff et al., 2001; Rueff et al., 2008) have also been used to study magnetic moment of atoms, yet like Mössbauer, these techniques are based on complex influences between magnetism and electron energy levels. On the other hand, the signals from Mössbauer and X-ray related spectroscopy are mass independent, which makes these techniques favorable to study magnetism at high pressure due to the very small ($<1*10^{-3}$ mm^3) sample used in the diamond cell chamber. However, these methods can be thought of as indirect, due to electromagnetic effects at the nucleus; they thus do not provide physical quantities relevant to the Earth sciences like saturation magnetization (Ms), remanent saturation magnetization (Mrs), the bulk coercivity (Bc) and the coercivity of remanence (Bcr), which are the basic magnetic parameters describing the quality of ferromagnets. There exists a stark discrepancy concerning the magnetic state of *hcp* Fe between Mössbauer spectroscopy, which suggests it is non-magnetic (Pipkorn et al., 1964; Taylor et al., 1982) versus direct observations of the interaction of *hcp* Fe with an applied field (Gilder and Glen, 1998), consistent with a ferromagnetic interpretation.

This thesis concerns direct magnetic measurements of materials relevant to planetary cores. The intention of this work is to measure magnetic parameters such as remnant saturation moment (Mrs), coercivity of remanence (Bcr) and Curie temperature (Tc) of iron and iron alloys (Fe-Ni, Fe-Si and Fe-S) under high pressure up to the *hcp* iron stability range (~20 GPa). To do so, new pressure cells and techniques were developed and materials for the experiments needed to be either purchased (when possible) or synthesized in the lab. All of these steps and the results are described herein.

The outline or the thesis is organized as follows:

Chapter 1 describes the basic experimental methods and procedures used in the experiments. Our experiments used a superconducting quantum interference device (SQUID)-based magnetometer combined with a non-magnetic moissanite or diamond anvil cell. This combination allows one to measure the magnetizations of tiny amounts of ferromagnetic samples up to 25-30 GPa. Pressure in the cell was measured using in-situ ruby fluorescence spectroscopy. An isothermal remanent magnetization (IRM) is applied to the sample using a specially designed electromagnet. Backfield acquisition curves of the sample under pressure permit one to measure two fundamental magnetic parameters: the coercivity of remanence (Bcr), defined as the magnetic field in mT required to null the remanent magnetization and the saturation isothermal remanent magnetization (SIRM). For Curie temperature studies, we developed a new method based on laser heating by controlling the power density.

Chapter 2 reports experiments on remanent magnetization of iron powder and foil in response to applied magnetic fields under pressure up to 21.5 GPa at room temperature. Two independent experiments using different pressure transmission media reveal a higher remanent magnetization at 21.5 GPa than at initial conditions, which could be attributed to a distorted hexagonal closed packed phase grown during the martensitic transition. Upon both compression and decompression, the remanent magnetization of the *bcc* Fe increases several times over initial conditions while the coercivity of remanence remains mostly invariant with pressure. These results were published in: Wei, Q.G., and S.A. Gilder (2013), Ferromagnetism of iron under pressure to 21.5 GPa, Geophysical Research Letters, 40, 5131–5136, doi:10.1002/grl.51004.

Chapter 3 describes the remanent magnetization of *fcc* iron-nickel alloys ($Fe_{64}Ni_{36}$, $Fe_{58}Ni_{42}$, and $Fe_{50}Ni_{50}$) and pure Ni in response to applied magnetic fields under pressures up to 23 GPa at room temperature. Magnetization decreases markedly for $Fe_{64}Ni_{36}$ between 5 and 7 GPa, yet remains ferromagnetic until at least 16 GPa. Magnetization rises by a factor of 2-3 for the other phases during compression to the highest applied pressures. The magnetic remanence of low Ni invar alloys increases faster with pressure than for other body centered cubic compositions due to the higher magnetostriction of the low Ni invar metals. Thermal demagnetization spectra of $Fe_{64}Ni_{36}$ measured after pressure cycling broaden as a function of peak pressure, with a systematic decrease in Curie temperature. Irreversible strain accumulation from the martensitic transition also likely explains the widening of the Curie temperature spectra, consistent with X-ray diffraction analyses. This work was published in: Wei, Q.G., S.A. Gilder, and B. Maier (2014), Pressure dependence on the remanent magnetization of Fe-Ni alloys and Ni metal, Physical Review B, 90, 144425, doi:10.1103/PhysRevB.90.144425.

Chapter 4 focuses on the magnetic properties of *bcc* Fe-Ni alloys ($Fe_{92}Ni_{08}$, $Fe_{87}Ni_{13}$, and $Fe_{84}Ni_{16}$) and *bcc* Fe-Si alloys ($Fe_{91}Si_{09}$, and $Fe_{83}Si_{17}$) under pressures up to 24 GPa. Magnetization of $Fe_{92}Ni_{08}$, $Fe_{87}Ni_{13}$ and $Fe_{84}Ni_{16}$ remain ferromagnetic up to 24.1 GPa, yet show significant hysteresis corresponding to the *hcp*-in to *bcc*-out and *hcp*-out to *bcc*-in transitions. Magnetization of $Fe_{91}Si_{09}$, and $Fe_{83}Si_{17}$ increases with pressure up to 22 GPa with no hint of a magnetic phase transition. These latter results have implications for the solid cores of Mercury and Mars. They are being prepared for publication and should be submitted in the Spring of 2015.

Chapter 5 describes the development of laser heating to measure Curie temperature as a function of pressure. Titanomagnetite ($Fe_{2.4}Ti_{0.6}O_4$ = TM60) and invar ($Fe_{64}Ni_{36}$) were used as test materials due to their relatively low Curie temperatures and because the change in Curie temperature for these phases were previously reported. These results are more preliminary than the room temperature studies and more work will be needed before writing them up for publication.

1. Experimental Methods

1.1 SQUID magnetometer

A superconducting quantum interference device (SQUID)-based magnetometer is a very sensitive instrument used to measure extremely subtle magnetic fields, based on superconducting loops (Figure 1.1a) containing Josephson junctions (wikipedia). A vertical three-axis, DC SQUID magnetometer, 2G Enterprises Inc., is housed in magnetic shielding room for magnetic moment measurements. Its sensitivity is $1.0*10^{-12}$ Am^2 (Figure 1.1b).

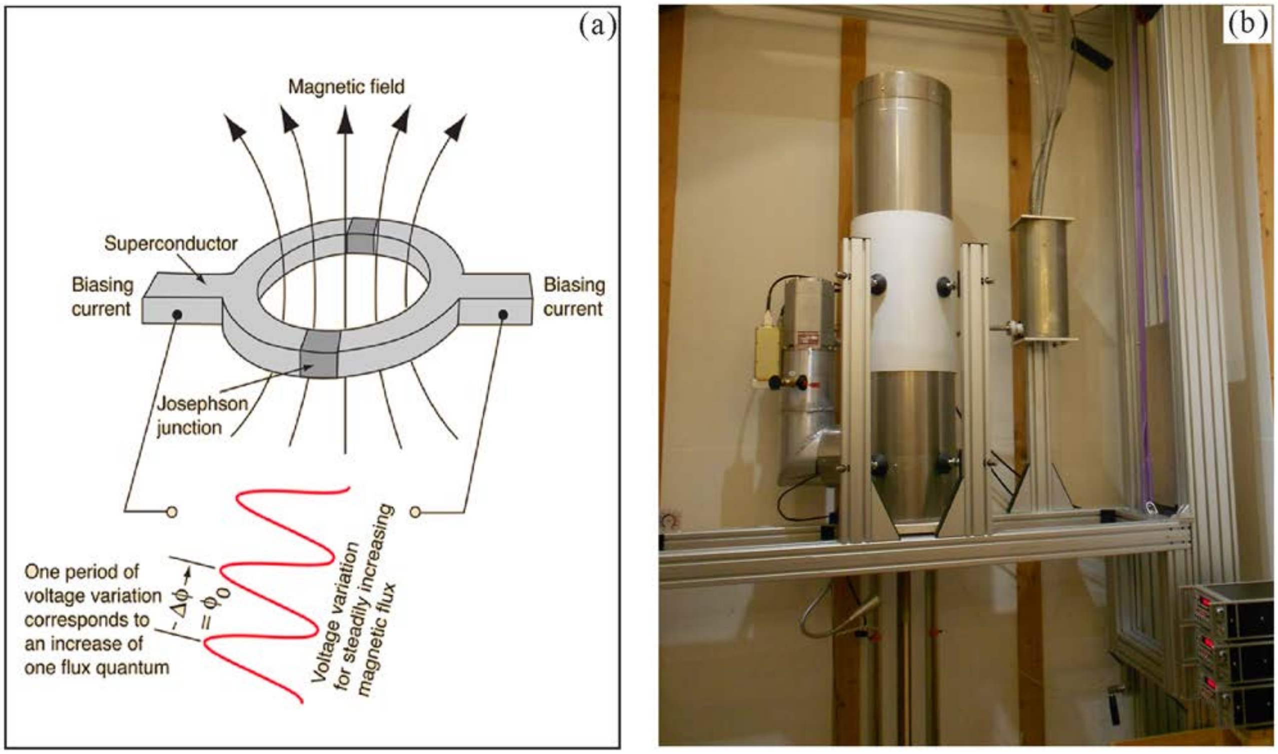

Figure 1.1 Superconducting quantum interference devices - SQUID magnetometer. **(a)** Schematic of a dc SQUID sensor (image from web of HyperPhysics). **(b)** A 2G Enterprises Inc., vertical three-axis, SQUID magnetometer, installed in paleomagnetic laboratory of geophysics LMU.

1.2 Diamond and Moissanite anvil cells

The diamond anvil cell (DAC) is widely used for generating high pressure on small volume samples (Figure 1.2a). Diamonds anvils usually are around 0.2 carat for economic considerations. To support the small diamonds, back seats made of hard materials are needed, usually tungsten carbide which are hard to be made non-magnetic. Like diamond, synthetic moissanite (SiC) is transparent and hard (9.5 on Mohs scale, compared to 10 for diamond). Moissanite is much cheaper than diamond in same size. Larger size (1 carat) single-crystal moissanite (SiC) anvils can be mounted in anvil cell directly without using back seats, which called moissanite anvil cell (MAC). Maximum pressures for MAC can be up to 60 GPa (Xu et al., 2002). In our experiments, moissanite anvils with culet diameter of 400-700 μm were mounted in a non-magnetic cell. The frame of the cell was build out of working hardened beryllium-copper alloy (Figure 1.2b), which has relative high mechanical strength and non-magnetic.

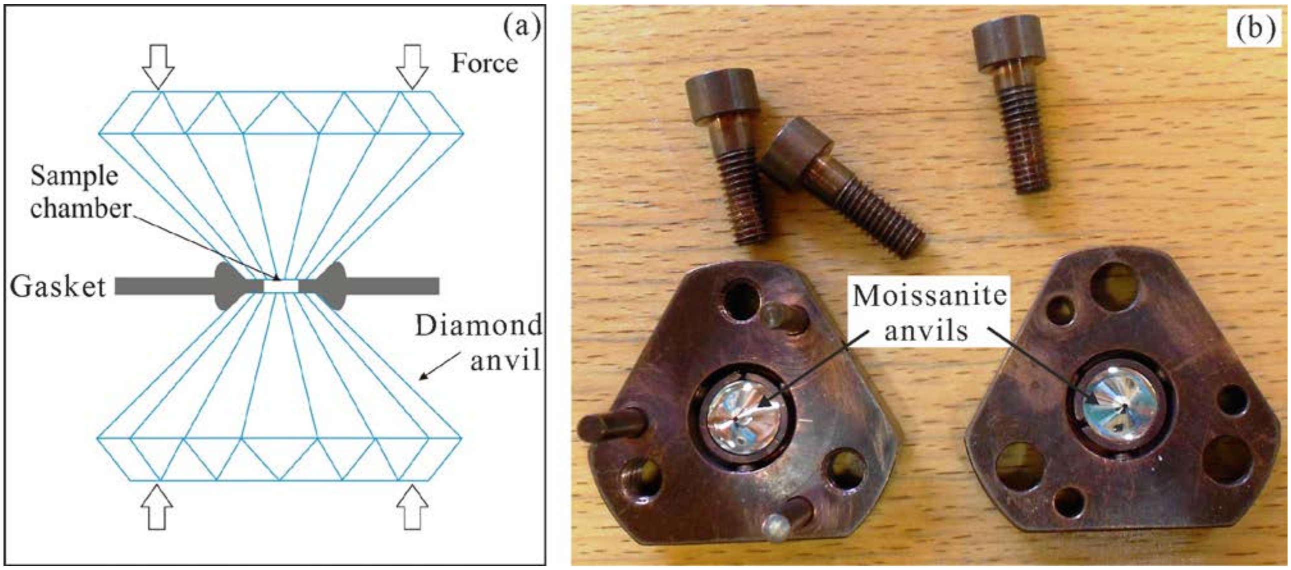

Figure 1.2 Diamond anvil cell or moissanite anvil cell. **(a)** Principle of a diamond anvil cell. **(b)** Nonmagnetic moissanite anvil cell made of working hardened beryllium-copper alloy.

Gaskets made of rhenium and work hardened beryllium-copper, with dimension of 2 mm in diameter and 250 μm in thickness, were used in the experiments. Both rhenium and beryllium-copper are non-magnetic. Small rings with conical shapes, also are 2mm in diameter, placed on tip of each anvil, sandwiching the gasket (Figure 1.3a &1.3b), which can improve the MAC to reach higher pressure without cracking the rhenium gasket. The small rings are made of beryllium-copper alloy; with their support the MAC with anvils culet of 400 μm diameter can provide pressure over 20 GPa in our experiments.

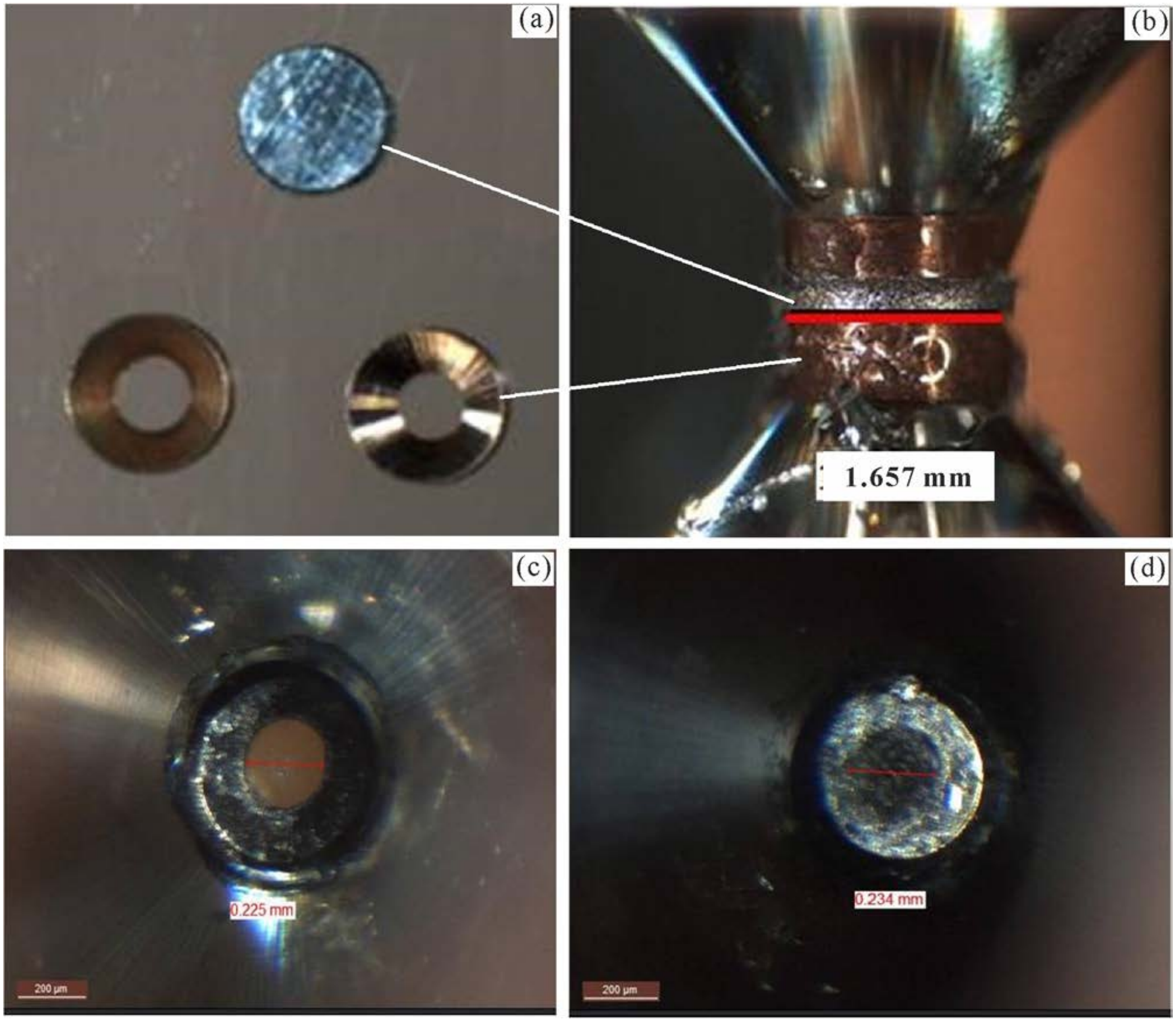

Figure 1.3 Experiment preparation of the moissanite anvil cell. **(a)** Rhenium gasket and support rings. **(b)** Side view of assemblage moissanite anvil cell with gasket was sandwiched between the two support rings. **(c)** A hole was drilled in center of the pre-pressed gasket. **(d)** Sample with pressure medium and tiny ruby spheres were loaded into the hole.

The gasket was pre-pressed for creating an indentation; and after that a hole was drilled in the center (Figure 1.3c), as sample chamber; sample with pressure medium and tiny ruby spheres will be loaded into the hole. To drill a well centered and perfect hole is very crucial for the high pressure studies of using diamond anvil cell. A electrical discharging machine (EMD), BETSA MH20M, is used for drilling holes on rhenium gaskets; mini drill bits made of steel or harder materials can drill holes in work hardened beryllium-copper gasket.

Pressure was measured using R1 peak of ruby fluorescence spectroscopy (Mao et al., 1986; Syassen, 2008) with a Coherent Inc., Cube 405 nm laser and a Princeton Instruments (PIXIS) charged coupled device connected to a 150 mm, ARC SpectraPro spectrometer (Figure 1.4), resolution 0.07 nm. Tiny ruby spheres doped with Cr^{3+} (Chervin et al., 2001) in diameter of ~1 μm were used in experiments. Few ruby spheres placed near the center and edge of the sample chamber helped monitor potential pressure gradients. Silica gel is used as pressure medium in most of our experiments, which behave more hydrostatic than NaCl (Klotz et al., 2009). One advantage of using silica gel is that it is sticky, which can avoid magnetic samples jumping or falling out of the sample chamber during experiment preparation.

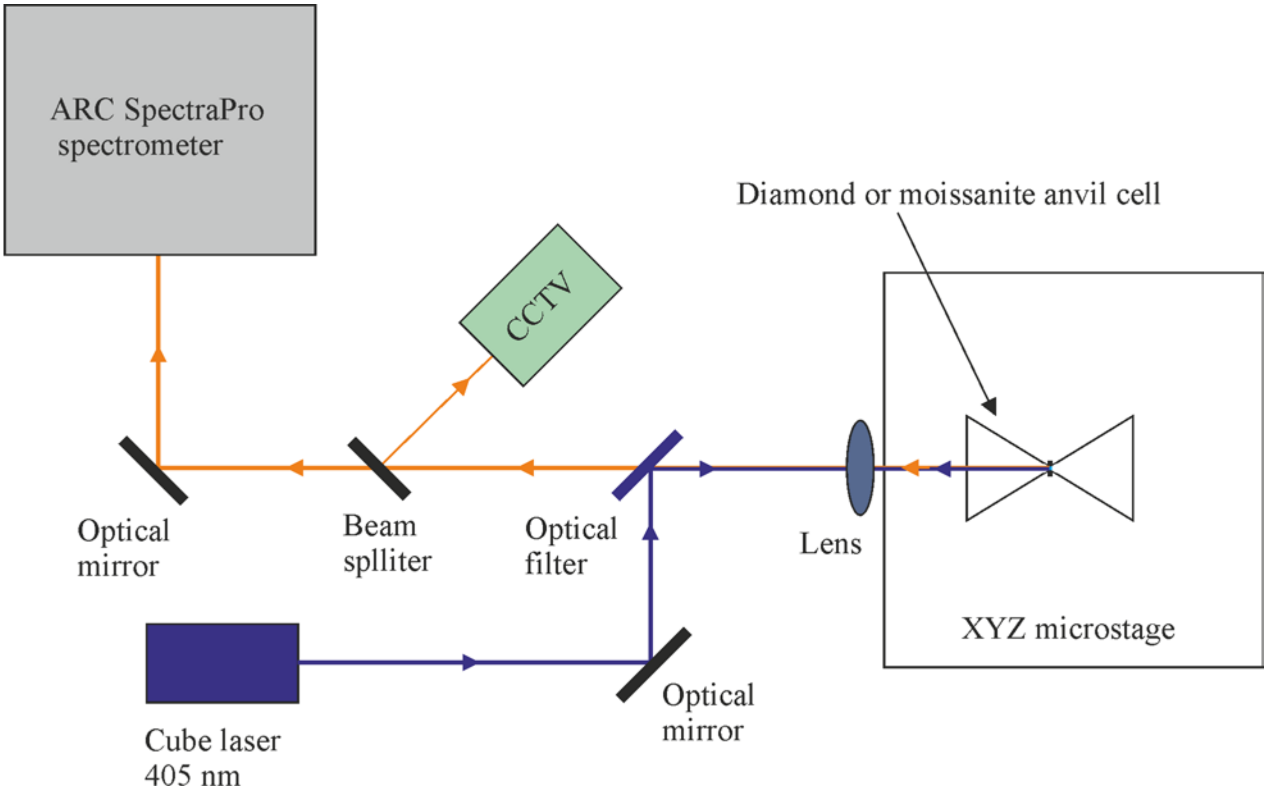

Figure 1.4 Optical setup for ruby fluorescence spectroscopy. Blue line represents the 405 nm blue laser, and orange line represents the fluorescence light from sample, Arrows represents the direction of the light path.

1.3 Isothermal remanent magnetization

A specially designed electromagnet (Figure 1.4a) was used to give an IRM to the sample in the diamond anvil cell while not magnetizing the whole cell (Gilder et al., 2011). A 2 mm gap between tips of the two sleeves is guaranteed by the fixed 2 mm gasket diameter used in the cell. A static field was directed perpendicular to the axis of the moissanite pistons with an electromagnet whose pole pieces slide through the cell's housing until they abut the pistons (Figure 1.5b). In order to acquire a backfield curve for sample in DAC, we proceed as follows. First we applied a magnetic field of 370 mT along the –y-axis direction of the cell (Figure 1.5c). The cell was removed from the electromagnet and then placed into the bore of a 2G Enterprises Inc., three-axis, DC SQUID magnetometer to measure the full magnetic vector. This first data point is considered as the starting point (0 mT) on a backfield acquisition diagram (Figure 1.6). We then stepwise increased the applied field intensity in the +y-axis direction until reaching 370 mT (Figure 1.5c), each time measuring the corresponding remanence with the magnetometer.

Figure 1.6 plots two curves for the empty cell, one at ambient pressure and another at 17 GPa, to demonstrate the precision that the cell's contribution can be ascertained and subtracted; another curve plots the magnetic moment of the sample (Iron foil at 0.9 GPa) after subtracting the magnetization of the empty cell. Two fundamental magnetic parameters can be extracted from the backfield curves: the coercivity of remanence (Bcr), defined as the magnetic field in mT required to null the remanent magnetization, and the saturation isothermal remanent magnetization (SIRM, in units of Am^2), which is defined here as the average moment from the last three steps of the curve.

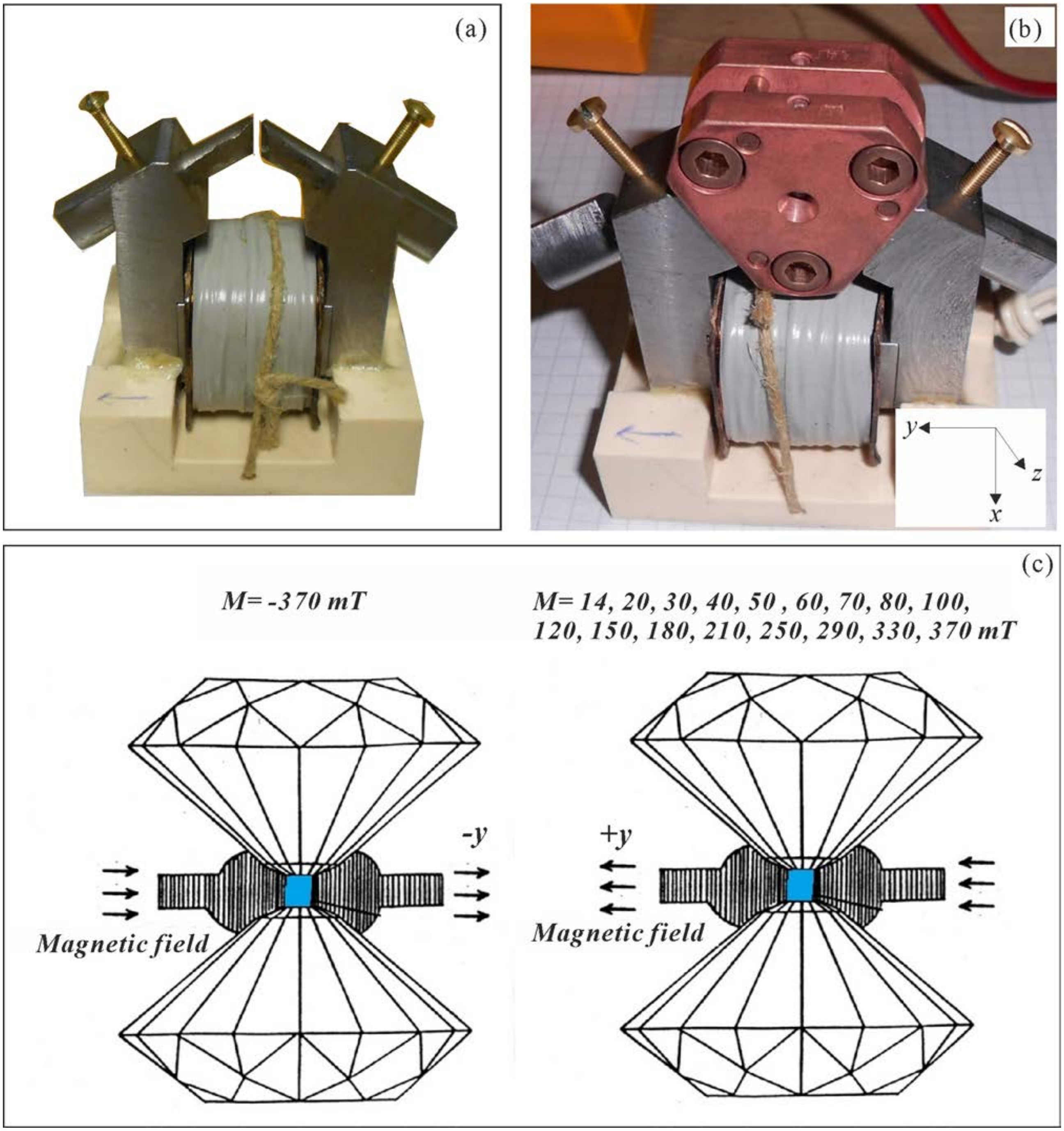

Figure 1.5 Isothermal remanent magnetization. **(a)** A self designed electromagnet, 1613 mA creates a static field of 370 mT at the sleeve joints. **(b)** Setup diamond anvil cell onto the electromagnet with corresponding axis's when measured in SQUID magnetometer. **(c)** Schematic process to acquire a backfield curve, arrow represents the magnetic field.

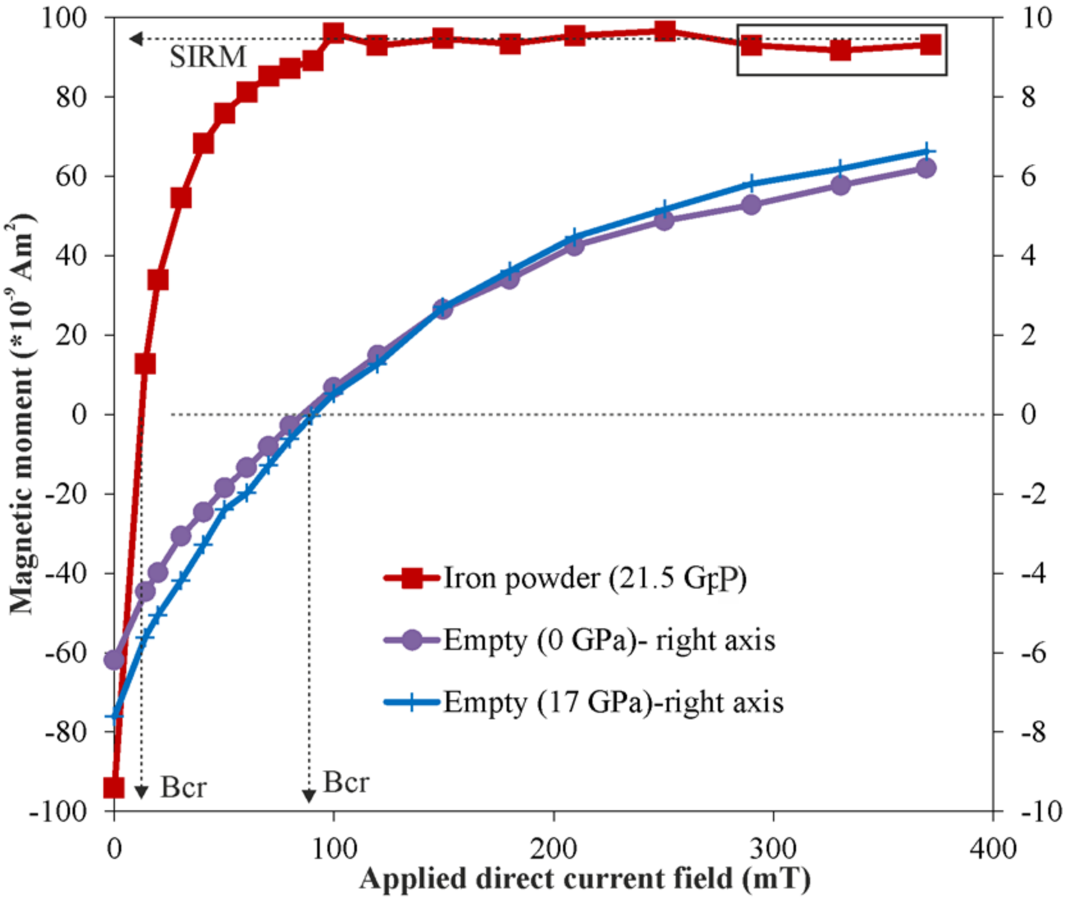

Figure 1.6 Backfield curves of cell with and without sample. Remanent magnetization of empty cell at pressures of 0 GPa and 17 GPa; and iron powder at 21.5 GPa, has been subtracted from the empty cell. Remanent magnetizations at 0 mT were actually -370 mT, which set as “0 mT” as starting point of backfield curves. Bcr- coercivity of remanence; SIRM-saturation isothermal remanent magnetization.

1.4 Laser heating

A JK50FL fiber laser (maximum output power 50 W) is connected with a microscopic focusing laser process head (Figure 1.7) for heating. The power density of the laser spot can be controlled by combination of laser output power and defocusing (Figure 1.7). The off focusing distance is precisely controlled by a XYZ stage (resolution 0.01 mm), and focusing status can be monitored by the camera integrated on the laser process head.

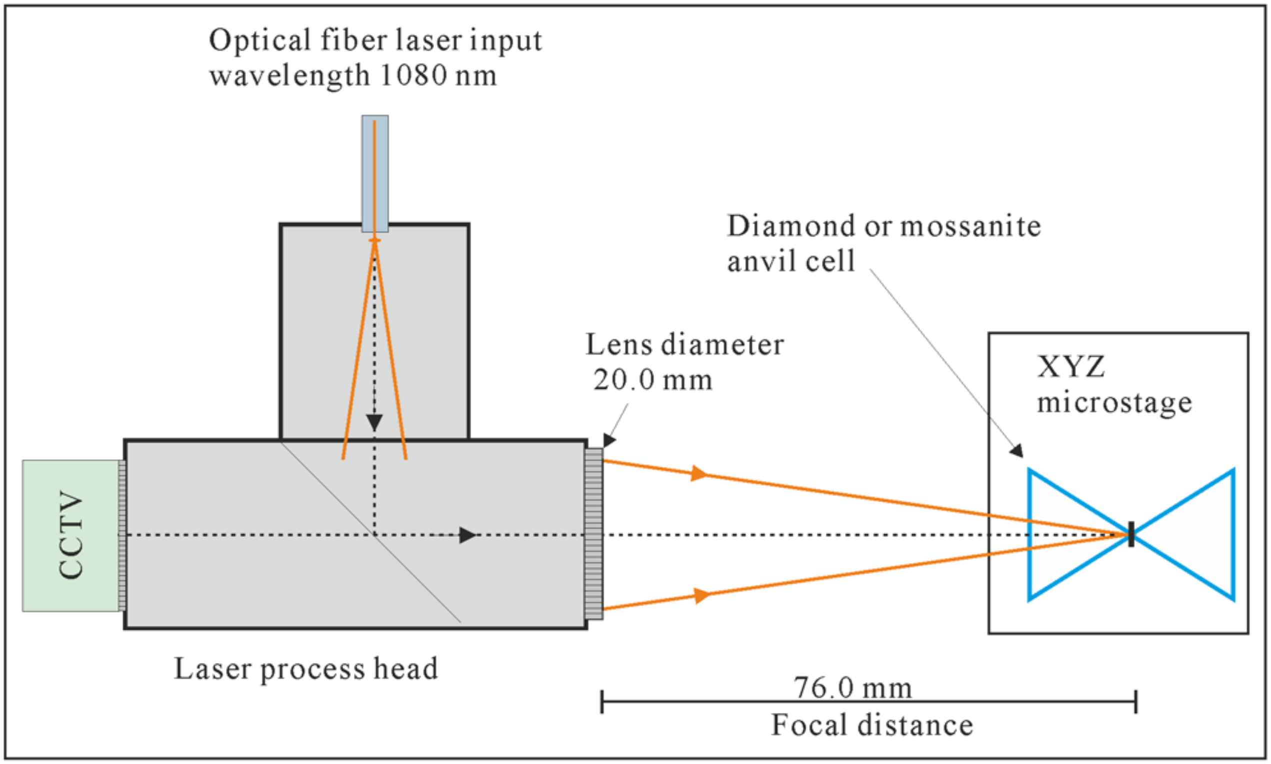

Figure 1.7 Sketch of the laser heating setup. JK50FL fiber laser (max output 50W) with laser process head (lens diameter 20.0 mm and focal distance 76.0 mm); focused laser beam through the diamond or moissanite anvil; focusing and off focus is controlled by a XYZ microstage in precisely (0.01 mm), monitored by the live camera (CCTV).

2. Ferromagnetism of iron under pressure to 21.5 GPa[1]

Computational, Mössbauer and synchrotron radiation experiments arrive at disparate conclusions regarding the magnetic state of the high-pressure, hexagonal closed packed, phase of iron, which likely comprises the bulk composition of Earth's inner core. Using a non-magnetic, moissanite anvil cell together with a superconducting magnetometer, we measured the remanent magnetization of iron in response to applied magnetic fields under pressure up to 21.5 GPa at room temperature. Two independent experiments using different pressure transmission media reveal a higher remanent magnetization at 21.5 GPa than at initial conditions, which could be attributed to a distorted hexagonal closed packed phase grown during the martensitic transition. Upon both compression and decompression, the remanent magnetization of the body centered cubic phase increases several times over initial conditions while the coercivity of remanence remains mostly invariant with pressure.

2.1 Introduction

Iron metal, together with limited contributions from nickel and light alloying elements, is widely believed to be the chief core constituent of the terrestrial planets, as well as Earth's moon and Jupiter's moon, Ganymede. It also comprises the dominant magnetic mineral in Moon rocks and in several meteorite classes. Iron exists in a body centered cubic (*bcc*) state at ambient conditions and in a hexagonal closed packed (*hcp*) state at room temperature above ~13 GPa (Takahashi and Bassett, 1964). Its phase in Earth's inner core is debated. Several studies conclude that the *hcp* phase is the best candidate (Brown and McQueen, 1986; Mao et al., 1990; Merkel et al., 2000; Takahashi and

---

[1] *Part of the contents published as: Wei, Q., Gilder, S.A., 2013. Ferromagnetism of iron under pressure to 21.5 GPa. Geophysical Research Letters 40, 5131-5136. doi:10.1002/grl.51004, 2013.*

Bassett, 1964), while others argue for a *bcc* or double hexagonal closed packed phase (Boehler, 1993; Dubrovinsky et al., 2000b). Experiments with iron alloyed with 4 and 10% nickel that attained Earth’s inner core pressures (340-374 GPa) at both room temperature and 4700 K identified the stable structure as *hcp* (Tateno et al., 2012).

Bcc Fe is ferromagnetic at ambient pressure with a Curie temperature of 780°C. Bezaeva et al. (2010) studied the stress demagnetization effect on iron to 1.2 GPa, yet the piezoremanence of *bcc* Fe is unknown. Such knowledge could be important, for example, for modeling lunar magnetic anomalies or interpreting the magnetic signals in meteorites and lunar samples. The magnetic state of *hcp* Fe is important to understand processes in Earth’s inner core, yet despite its importance for geophysics, as well as for solid-state physics, the magnetic state of *hcp* Fe remains contentious. Mössbauer spectroscopic investigations at room temperature find a broad transition between 9 and 20 GPa where the hyperfine splitting of *bcc* Fe decreases, supposedly as iron transforms progressively from a ferromagnetic to a non-ferromagnetic state (Pipkorn et al., 1964; Taylor et al., 1982). A sharp decrease in x-ray circular diachroism signal across the *bcc-hcp* transition corroborates the Mössbauer data (Baudelet et al., 2005). Density functional theory and full-potential calculations for non-collinear systems, made at 0 K, predict antiferromagnetic ordering of *hcp* Fe (Ono et al., 2010; Steinle-Neumann et al., 2004). X-ray emission spectroscopy shows a finite albeit progressively decreasing magnetism in *hcp* Fe that persists until 30 GPa (Rueff et al., 2008). Iron particles immersed in a fluid inside a diamond anvil cell were directly observed to move in response to an applied field gradient at 17 GPa and 260°C (Gilder and Glen, 1998). It was concluded from these experiments that *hcp* Fe is either ferromagnetic or paramagnetic with an extremely high susceptibility (0.15 to 0.001 SI). Here we present two independent experiments that show the magnetic saturation remanence of Fe increases systematically with pressure in the *bcc* realm and that Fe possesses magnetic remanence within the *hcp* stability field.

2.2 Experimental Procedure and Results

One experiment used iron powder (Sigma-Aldrich, 97% pure, 325 mesh (44 µm)) and the other iron foil (Goodfellow, 99.5% pure) to compare with previous results that routinely use either sample type (polycrystalline aggregate or foil). X-ray diffraction on the starting material of both samples reveals only *bcc* Fe peaks with no measurable contribution from iron oxide (magnetite or hematite) (Figure 2.1a). Hysteresis loops measured at room temperature and pressure with a Petersen Instruments, variable field translation balance yield remanence ratios (remanent magnetization after saturation (Mrs) / saturation magnetization (Ms)) of 0.06 for the powder and 0.006 for the foil; coercivity ratios (coercivity of remanence (Bcr) / bulk coercivity (Bc)) are 17 for the foil and 5 for the powder, indicating that both are in the multidomain state.

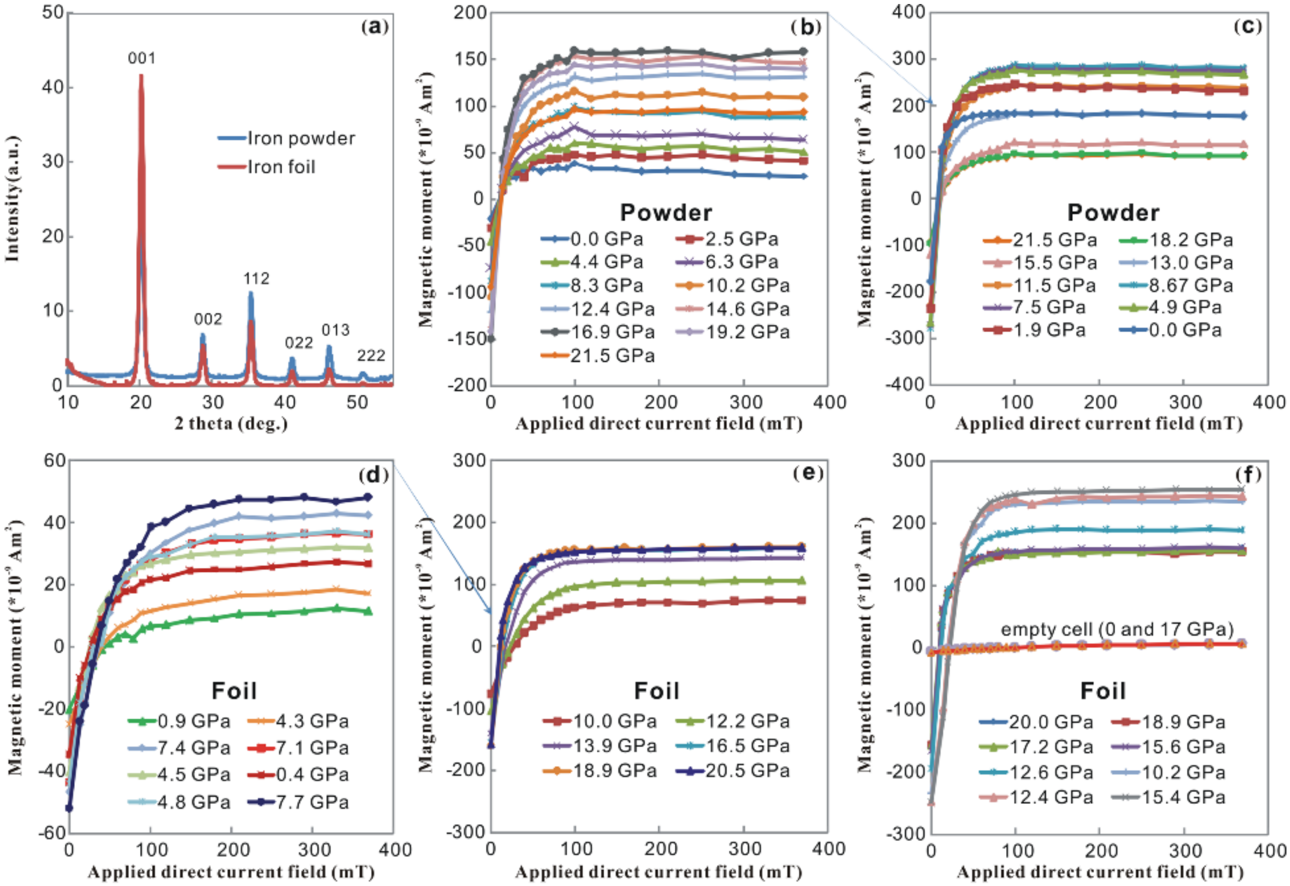

Figure 2.1 X-ray and backfield curves for iron powder and iron foil under pressure. **(a)** X-ray diffraction pattern of the iron powder and iron foil samples used in this study (0 GPa, 298 K) collected using a Mo X-ray source (0.71069 nm wavelength) (intensity scale in arbitrary units [a.u.]). **(b** and **c)** Backfield magnetization curves for iron powder with silica gel pressure medium. **(d-f)** Backfield magnetization curves for iron foil with sodium chloride pressure medium. Figure 2.1f also shows backfield magnetization curves of the empty cell measured at 0 and 17 GPa. Labels showed in figures is in sequence of left to right.

These samples were loaded together with ruby spheres and pressure medium into a hole drilled in a rhenium gasket contained by a moissanite-beryllium copper anvil cell. For pressure medium, the powder was mixed with silica gel whereas two pieces of foil were sandwiched between layers of sodium chloride. Initially, the foil was a square sheet of side = 25 mm and thickness = 0.25 mm, which was presumably fabricated with a rolling machine, so some initial strain could be present. Although less hydrostatic than other pressure media (methanol, etc.), silica gel is preferable because we can load the iron into the cell while insuring no iron remains outside the chamber. Pressure was measured before and after each experiment using ruby fluorescence spectroscopy with a Coherent, Cube 405 nm laser and a Princeton Instruments (PIXIS) charged coupled device connected to a 150 mm, ARC SpectraPro spectrometer. Rubies placed near the center and edge of the sample chamber helped monitor potential pressure gradients; differences reached 10% at 20 GPa. Below we report the average, and not peak, pressures.

At successive pressure steps, we measured the stepwise acquisition of isothermal remanent magnetization. A static field was directed perpendicular to the axis of the moissanite pistons with an electromagnet whose pole pieces slide through the cell’s housing until they abut the pistons. First we applied a magnetic field of 370 mT along the –y-axis direction of the cell. The cell was removed from the electromagnet and then placed into the bore of a 2G Enterprises Inc., three-axis, superconducting magnetometer to measure the full magnetic vector. This first data point is considered as the starting point (0 mT) on a backfield acquisition diagram (Figure 2.1b to 2.1f). We then stepwise increased the applied field intensity in the +y-axis direction until reaching 370 mT, each time measuring the corresponding remanence with the magnetometer. Identical experiments were carried out with the same cell and gasket void of iron. Figure 2.1b to 2.11f plot the magnetic moment of the sample after subtracting the magnetization of the empty cell. Figure 2.1f also plots two curves for the cell void of iron, one at ambient pressure and another at 17 GPa, to demonstrate the precision that the cell’s contribution can be ascertained and subtracted. Two fundamental magnetic parameters can be extracted from the backfield curves: the coercivity of remanence (Bcr), defined as the magnetic field in mT required to null the remanent magnetization, and the saturation isothermal remanent magnetization (SIRM, in units of Am^2), which is defined here as the average moment from the last three steps of the curve.

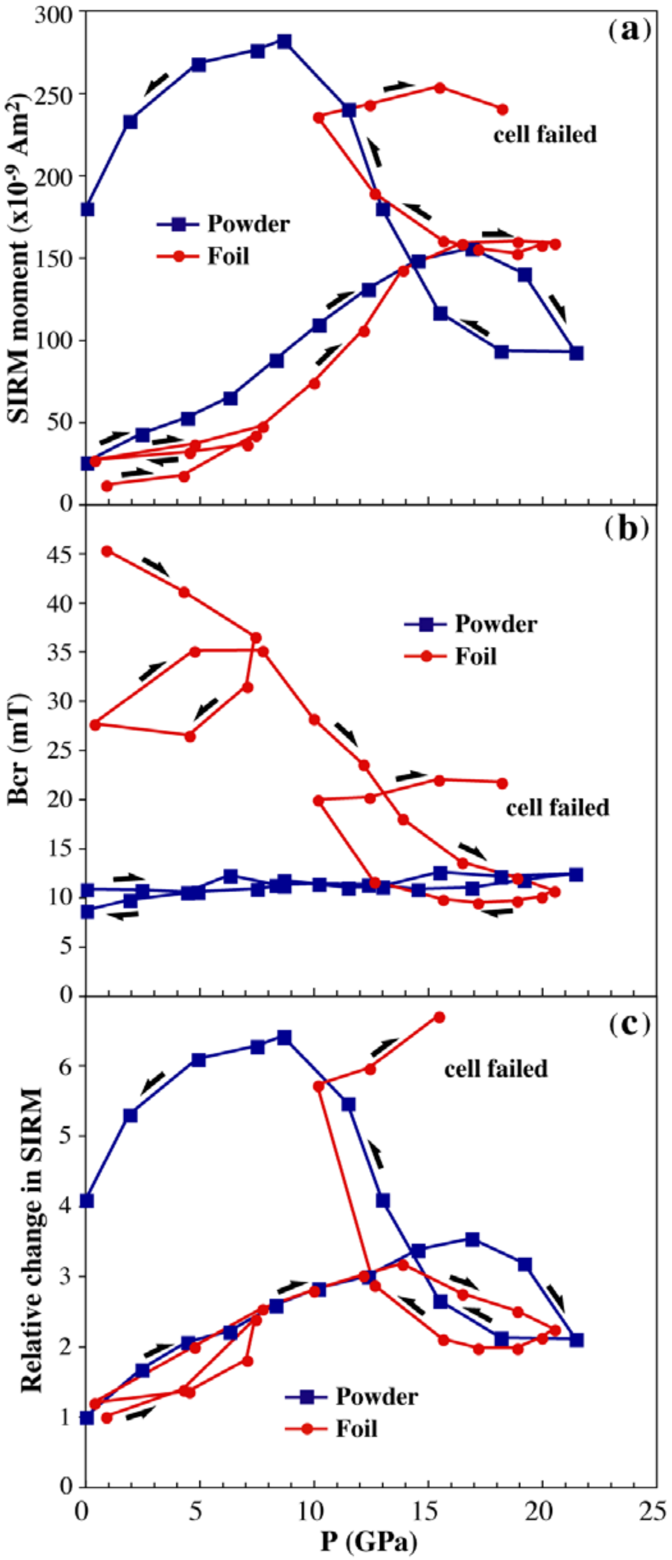

Figure 2.2 SIRM and Bcr as function of pressure for iron powder and foil. **(a)** Saturation isothermal remanent magnetization (SIRM) as a function of pressure. **(b)** Coercivity of remanence (Bcr) as a function of pressure. **(c)** Normalized SIRM (by the initial value) of both the powder and foil samples

after accounting for changes in their shape anisotropy. Arrows show the pressure path; data from Table 2.1.

The powder sample was progressively compressed to 21.5 GPa and then progressively decompressed back to ambient conditions (Figure 2.1b and 2.1c). A more complicated pressure path was used in the experiment with the iron foil. The sample was compressed to 7.4 GPa, decompressed to 0.4 GPa, recompressed to 20.5 GPa, decompressed to 10.2 GPa, and then recompressed to 15.5 GPa where after the cell failed upon further compression (Figure 2.1d to 2.1f). One observes that the iron acquires a magnetic remanence at all pressures in both experiments, with a general tendency that iron becomes more magnetic (i.e., greater moment acquisition at a given field strength) with increasing pressure.

Figure 2.2 plots SIRM and Bcr as a function of pressure for each experiment (Table 2.1). Magnetization is mass dependent whereas coercivity is not; in our case, the samples' masses are unknown. Uncertainties on the magnetization data are greater at low pressures (initially) than at high pressures because SIRM moments increase with pressure, being 6 times more magnetic for iron powder and 13 times more magnetic for iron foil at 17-18 GPa than at initial conditions. Above 17 GPa for the powder and 19 GPa for the foil, SIRM moment decreases, although even at the highest pressures achieved, SIRM moments remain significantly higher than those at starting conditions. SIRM moments further increase upon decompression. Bcr of the iron powder varies little as a function of pressure, slightly increasing from 11 to 12 mT between room pressure and 21 GPa. Bcr upon decompression is fairly reversible, ending up 2 mT less (9 mT) upon full decompression than before compression. The iron foil has a larger coercivity (45 mT) than the powder at starting conditions. Stress decreases Bcr to similar values as the powder (10 mT) above 16 GPa (Figure 2.2b). Bcr increases upon unloading from 17 to 10 GPa and then again upon further compression before the cell failed.

2.3 Shape anisotropy of iron disks

Because of the uniaxial compression in moissanite anvil cell, the shape of the sample chamber will change, the shape changing case for iron powder and foil experiments showed in Figure 2.3. Changes in shape anisotropy in produces changes in magnetization though the demagnetization factor (Dunlop and Özdemir, 1997). In order to find out how the shape change influenced the magnetization a experiment carried out on piled 1, 2, 3 and 10 iron disks (diameter 3mm) with height of 0.25 mm, 0.50 mm, 0.75 mm, and 2.5 mm respectively, dimension of one disk has a diameter (d) of 3 mm and height (h) of 0.25 mm (h/d = 0.083). Coercivity of remanence (Bcr) and ratio of remanent magnetization after saturation (Mrs) / saturation magnetization (Ms) for iron foil disks measured with a Princeton Instruments vibrating sample magnetometer versus the angle between the applied field and the plane of the disk (the two are parallel at 0° and orthogonal at -90° and +90; absolute angular uncertainty is ~10°) (Figure 2.4). Measured data is showed in Table 2.2.

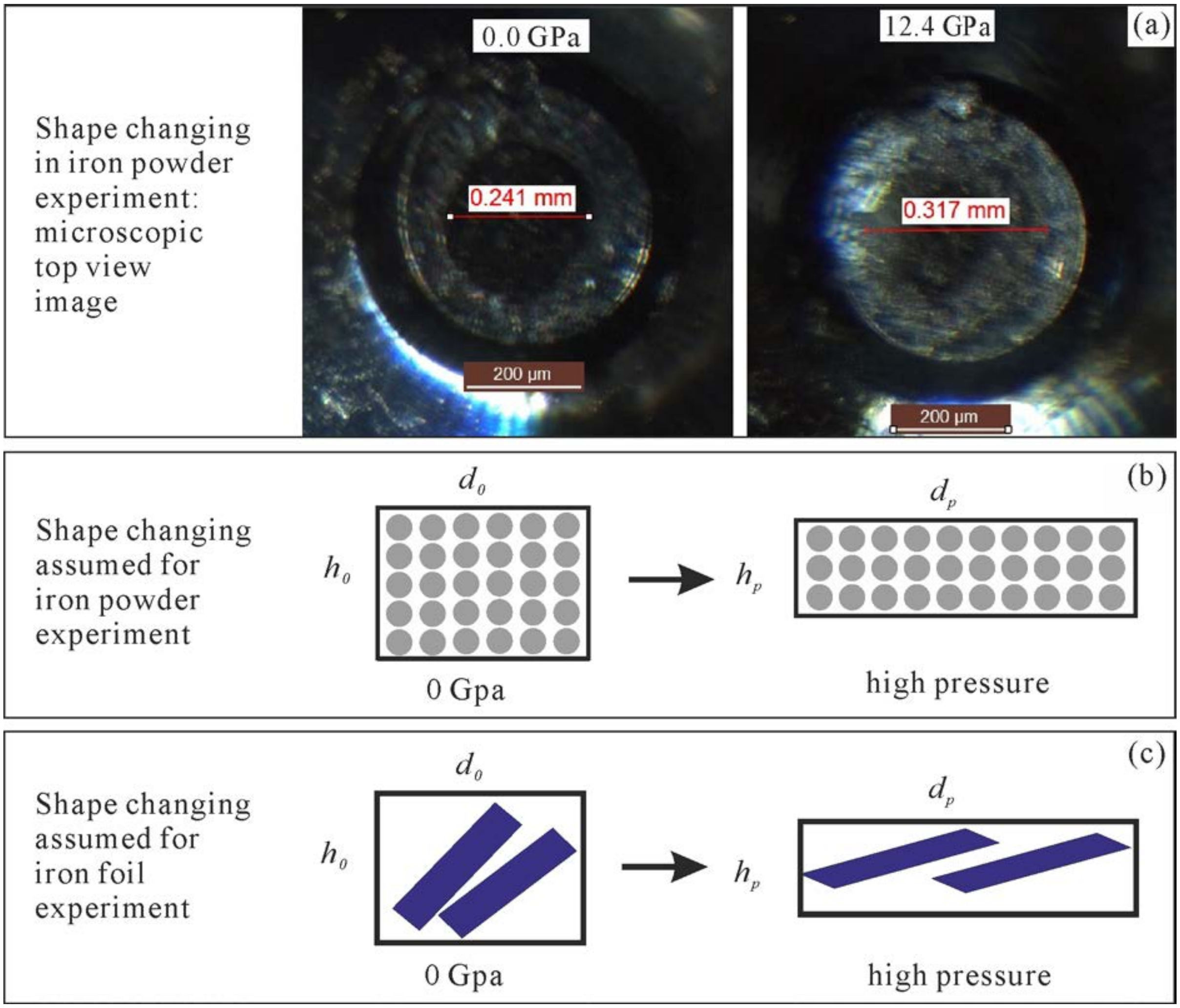

Figure 2.3 Shape changes under uniaxial compression in moissanite anvil cell. **(a)** shape change viewed form microscope for iron powder experiment. **(b)** Assumed shape change for the iron power experiment. **(c)** Assumed shape change for the iron foil experiment. For, h_0 and d_0 represent height

and diameter of sample chamber at initial; and h_p and d_p represent height and diameter of sample chamber at high pressure in moissanite anvil cell.

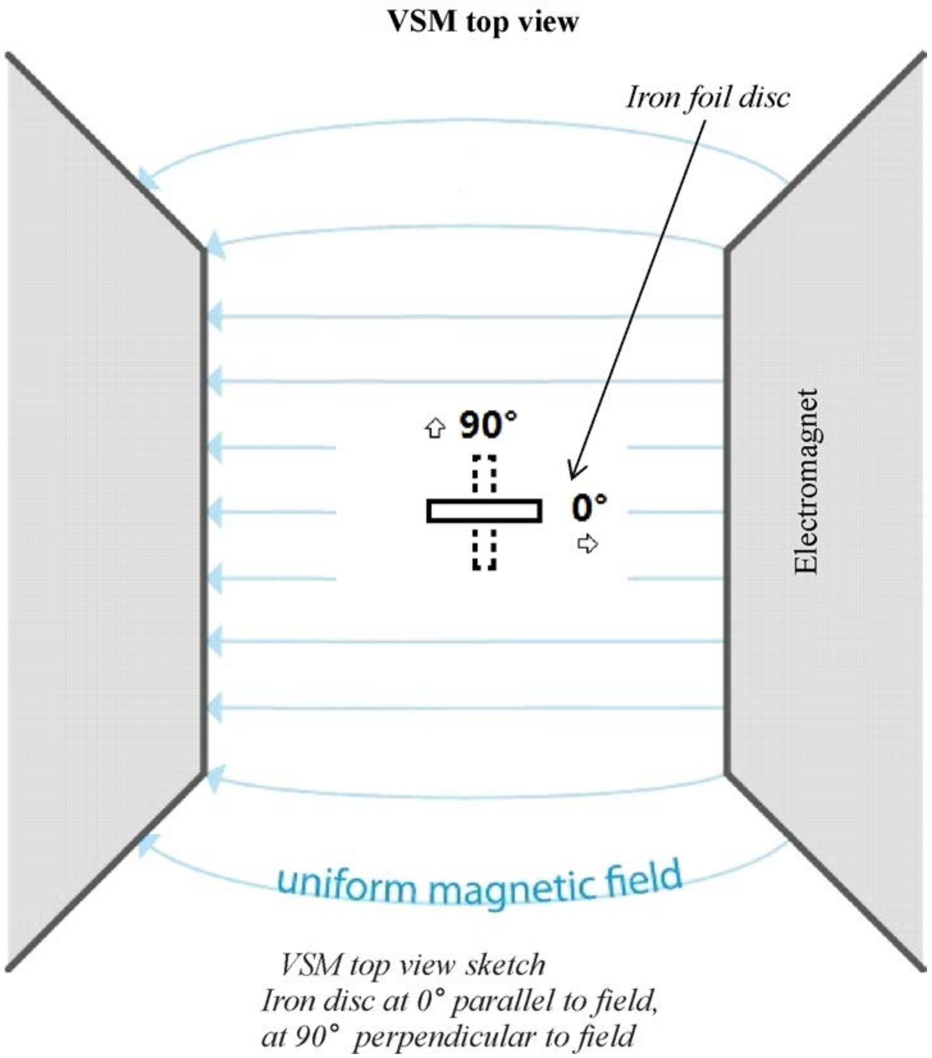

Figure 2.4 Vibrating sample magnetometer measurements of iron disks. Top view sketch, of a Princeton Instruments vibrating sample magnetometer (VSM), arrow represents the magnetic field.

The coercivity of remanence (Bcr) and ratio of remanent magnetization after saturation (Mrs) / saturation magnetization (Ms) versus the angle between the applied field and the plane of the disk showed in Figure 2.4. The results is consistent with theoretical calculations of demagnetization factors for oblate spheroids (Dunlop and Özdemir, 1977).

Remanent magnetization after saturation (Mrs) versus coercivity of remanence (Bcr) for h/d=0.167 and 0.250, data in Table 2.2, fitted in power function of $Mrs = 4.6729*Bcr^{-0.8624}$ (Figure 2.6a), and ratio of remanent magnetization after saturation (Mrs) / saturation magnetization (Ms) for iron foil disks versus h/d at at 0° (Figure 2.5b) fitted in power function of $Mrs/Ms = 8.3628x10^{-4}(h/d)^{-0.6619}$ (Figure 2.6b). The two power function were used as S_{corr} and Bcr_{corr} in Table 2.1, corresponding shape anisotropy correction in ablation for iron powder and foil and angle changing for iron foil.

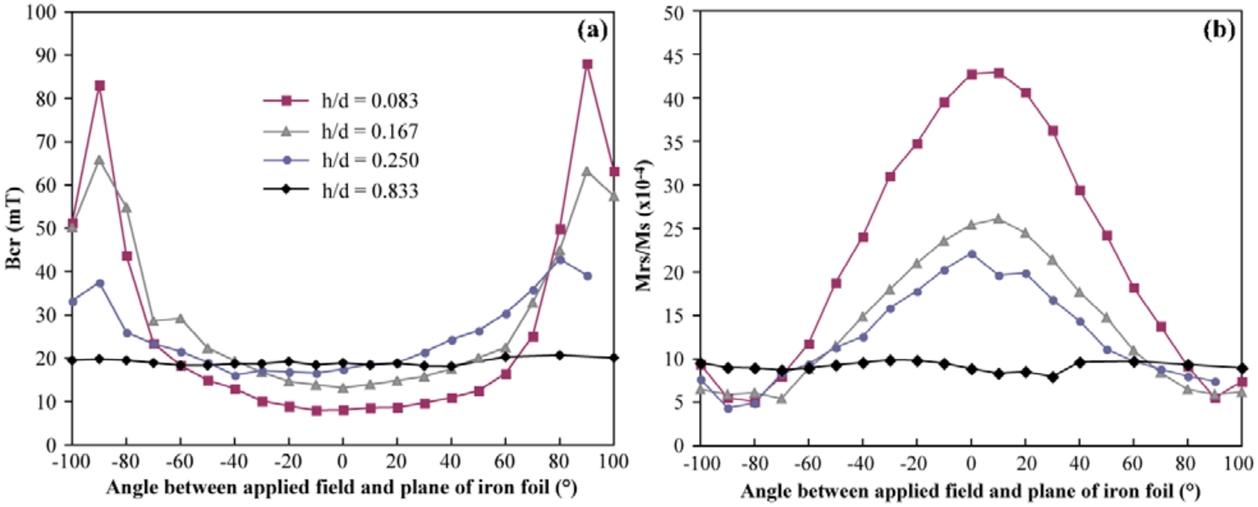

Figure 2.5 Bcr and Mrs/Ms of iron disks for VSM measurement. **(a)** Coercivity of remanence (Bcr) and **(b)** ratio of remanent magnetization after saturation (Mrs) / saturation magnetization (Ms) for iron foil disks measured with a Princeton Instruments vibrating sample magnetometer versus the angle between the applied field and the plane of the disk (the two are parallel at 0° and orthogonal at -90° and +90; absolute angular uncertainty is ~10°). The dimension of one disk has a diameter (d) of 3 mm and height (h) of 0.25 mm (h/d = 0.083). Cylinders have spherical (negligible) shape anisotropy when 0.9 > h/d > 0.8 (Collinson, 1983). Mrs/Ms data were normalized by a fit of the h/d = 0.833 data to remove non-saturation effects at higher angles; maximum field = 800 mT.

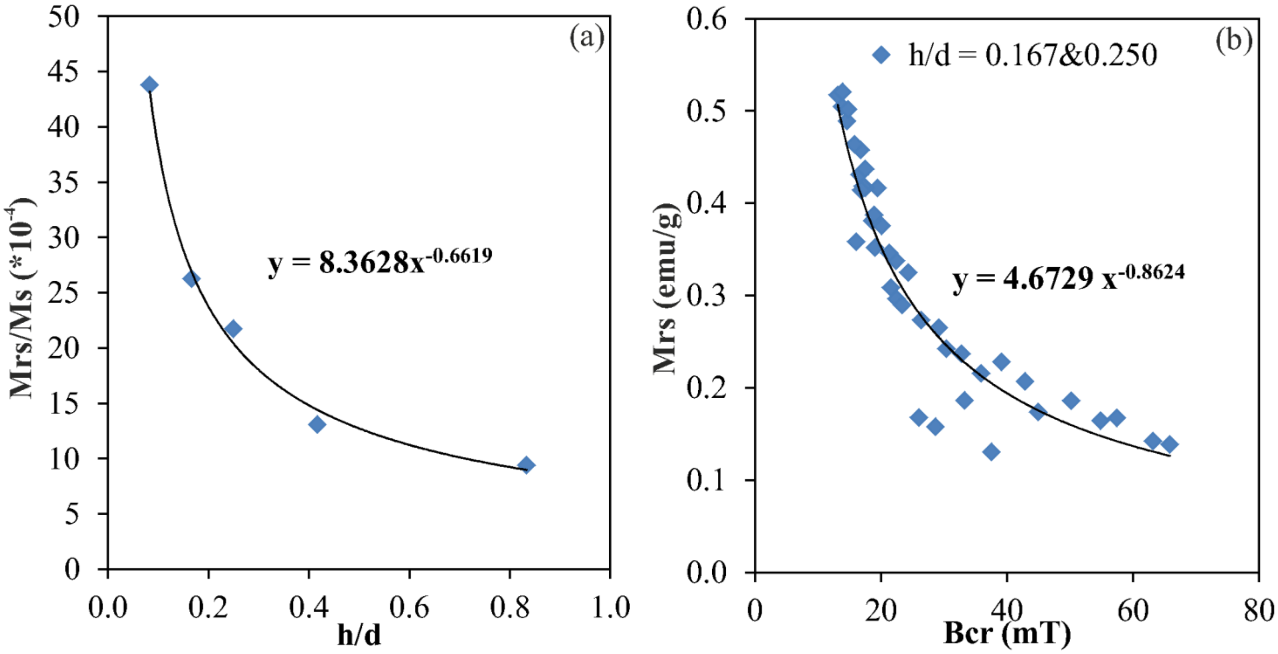

Figure 2.6 Magnetic parameters versus shape for iron disks. **(a)** ratio of remanent magnetization after saturation (Mrs) / saturation magnetization (Ms) for iron foil disks versus h/d fitted in power function of Mrs/Ms = $8.3628\text{x}10^{-4}(\text{h/d})^{-0.6619}$. **(b)** Remanent magnetization after saturation (Mrs) versus coercivity of remanence (Bcr) for h/d=0.167 and 0.250, fitted in power function of Mrs = $4.6729*\text{Bcr}^{-0.8624}$. Data in Table 2.2.

2.4 Discussion

The experimental results demonstrate the presence of a ferromagnetic material until the highest pressures achieved (21.5 GPa). An experimental artifact can be dismissed as the magnetization of the empty cell is <5% than that of the cell with iron at high pressure; moreover, significantly different pressure-dependent magnetic behaviors were observed for titanomagnetite and pyrrhotite using the same cell (Gilder and Le Goff, 2008; Gilder et al., 2011). On the other hand, changes in the shape anisotropy of the sample can partially account for the pressure dependency of the magnetic parameters. The initial dimensions of the sample chamber for the powder are diameter (d) ~248 μm and height (h) ~150 μm (h/d =0.6), which already deviates from spherical (null) shape anisotropy. As pressure increases above ca. 5 GPa, h/d decreases, resulting in higher degrees of oblateness and thus lower demagnetization factors in the long axis direction. By 13 GPa, the sample chamber for the powder has a diameter of ~320 μm and height of ~90 μm (h/d = 0.28); h/d remains fairly constant above 13 GPa until 19.2 GPa (Table 2.1). Because the applied field direction lies along the long axis of the sample, increasing the maximum to minimum axis ratio would result in a slight decrease in Bcr and a roughly two-fold increase in SIRM (Figure 2.5b), consistent with theoretical calculations of demagnetization factors for oblate spheroids (Dunlop and Özdemir, 1977). We can correct for the change in demagnetization factor by normalizing the SIRM values for the change in shape (S_{corr}) directly from the data in Table 2.2 (Figure 2.5b) by fitting a power function to h/d versus SIRM at 0°, which yields $S_{corr} = 8.3628\text{x}10^{-4}(h/d)^{-0.6619}$ (Table 2.1, Figure 2.6a). We assume the cell geometry changes insignificantly from 0 to 5 GPa and above 13 GPa, and remains the same upon decompression according to the highest pressure previously achieved.

Initially, the foil has roughly two times higher (45 mT) coercivity than expected for a sphere. This is likely due to the initial shape of the foil sample and how it was positioned inside the cell relative to the applied field direction, which would lead to SIRM values at low pressures that are actually underestimated (Figure 2.5). During loading, the foil sample would be flattened out, becoming more like an oblate spheroid with its long axis parallel to the field direction like in the case with the powder. The resulting change in sample geometry with increasing pressure would lower Bcr and increase SIRM above that due solely to an increase in oblateness following a trend from high to low angles in Figure 2.5, also explaining why the relative increase in SIRM moment of the foil is greater than that of the powder and why Bcr values between foil and powder become comparable at higher pressures. We did not measure the sample chamber geometry in the foil experiment, but the gasket was prepared in the same way, so we assume the same change in geometry following the powder experiment and apply the same correction factor (S_{corr}) to the SIRM data accordingly (Table 2.1). To make the additional correction, we fit a power function relating Bcr to Mrs in Table 2.2 (Figure 2.5a) for h/d of 0.17 and 0.25 where $\text{SIRM} = 4.6729 * \text{Bcr}^{-0.8624}$ (Figure 2.6b). We then calculate the SIRM normalization factor from the experimental Bcr data by assuming Bcr of the foil should be constant with pressure as in the powder experiment (Bcr_{corr} in Table 2.1). Figure 2.2c shows the change in SIRM relative to the initial (0 GPa) value following the correction procedure. The curves now match relatively well; the peak in SIRM moments are shifted to lower pressures, yet SIRM moments remain significantly above starting values well into the *hcp* Fe stability region.

Can the remanence exhibited in the *hcp* stability field be due to unconverted *bcc* Fe? SIRM and Bcr will also vary as a function of pressure among experiments depending on the pressure gradient (degree of non-hydrostaticity) in the cell since the gradient will determine the relative proportion of the two phases. In a study of the *bcc-hcp* transition pressure, (Patrick, 1954) found significant hysteresis depending on the shear strength of the pressure medium. Their room temperature experiments on iron with NaCl pressure medium, like in our foil experiments, identified the starting pressure for the transition at 12.4±0.3 GPa, with complete transformation to *hcp* at 17.8±0.8 GPa. Although they did not perform an experiment with silica gel, silica gel should behave more hydrostatic than NaCl (Klotz et al., 2009), implying that the starting and completion transition pressures should be lower than those for NaCl. Moreover, we report mean and not peak pressures, so one should add ~5% to our pressures when comparing with other studies.

If one assumes that *hcp* Fe is non-magnetic, then as the volume of *bcc* Fe decreases with increasing pressure, the magnetization of *bcc* Fe must increase proportionally to explain our results. Assuming that Ms stays constant as a function of pressure for *bcc* Fe, then the maximum possible increase in SIRM, which is equivalent to the saturation remanent magnetization (Mrs), is 16 and 167 times for the powder and foil, respectively, since the remanence ratio (Mrs/Ms) cannot exceed 1. At 19.2 GPa for the powder and 20.5 GPa for the foil, SIRM increases 5 and 13 times initial conditions (non-corrected), respectively, implying that the cell could contain up to 32% and 8% unconverted *bcc* Fe and 18% and 1% according to the corrected values. However, because coercivity remains constant, a remanence ratio of one is a gross overestimate as the Fe must be well below the single domain threshold. Given a remanence ratio of 0.3 (still unrealistically high), the required proportion of *bcc* Fe in the cell triples these estimates, which seems implausible, especially for the powder.

That the SIRM moments begin decreasing around the transition pressure into the *hcp* Fe stability field (Figure 2.2c) is consistent with the X-ray emission spectroscopy results (Rueff et al., 2008). They show magnetization persists above the structural *bcc-hcp* transition, yet diminishes with increasing pressure, with measurable signal until 30 GPa. Ultra-fast x-ray emission spectroscopy detects remanent magnetization up to 40 GPa (Monza et al., 2011). Thus, together with our results, it appears possible *hcp* Fe could be ferromagnetic initially (intermediate *hcp* Fe), and then become non-ferromagnetic as pressure increases (Figure 2.7). However, x-ray emission, as well as x-ray absorption (Mathon et al., 2004), data show a marked discontinuity across the transition boundary whereas our new findings do not, which raises the question on the role of hydrostaticity and hysteresis across the transition. Pressure gradients would make the transition appear more diffuse when averaged over the bulk sample. The experiments of Gilder and Glen (1998) were done under perfectly hydrostatic conditions—motion of iron in response to an external magnet to 18.4 GPa would then unlikely be due to *bcc* Fe.

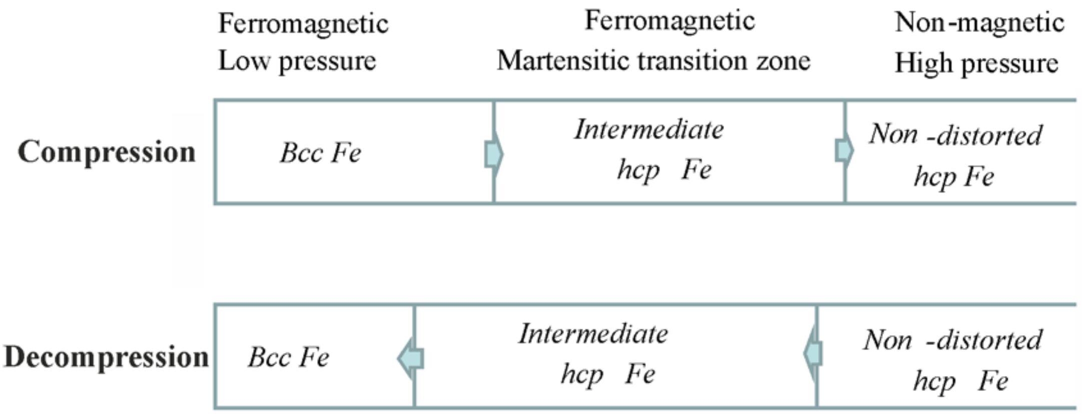

Figure 2.7 Simple demonstration of the phase and magnetic transition of iron under pressure in our experiments.

Alternatively, energy dispersive x-ray diffraction (Bassett and Huang, 1987) and x-ray absorption fine structure (Wang and Ingalls, 1998) experiments find that the *bcc* and *hcp* lattice constants behave anomalously in the hysteretic part of the martensitic transition (a diffusionless, structural transition produced by internal shear); the *hcp* phase is structurally distorted with an anomalously large c/a ratio. One way to reconcile the results would be if this intermediate *hcp* phase is ferromagnetic while the non-distorted *hcp* phase is not. An intermediate *hcp* phase would also explain why the magnetization decreases in our experiments during decompression from ca. 8 GPa.

A few explanations can resolve the inconsistency with Mössbauer spectrometry of iron under pressure. In the presence of type-II antiferromagnetic coupling (Steinle-Neumann et al., 2004), the hyperfine field would be significantly reduced in *hcp* Fe (Rueff et al., 2008). Increased shape anisotropy (this study) together with rotation of the magnetization perpendicular to the maximum stress direction, and thus perpendicular to the incident gamma ray, will additionally modify the absorption spectra (Gilder and Le Goff, 2008). Pressure also creates a preferred alignment of the crystallographic axes of *hcp* Fe, with c-axes oriented orthogonal to the compression axis (Merkel et al., 2004).

2.5 Conclusions

Our experiments show that saturation isothermal remanent magnetization (SIRM) of iron powder and foil is enhanced 3-4 fold during compression, and enhanced even higher, about 7 fold, during decompression. Coercivity of remanence (Bcr) of iron is relatively constant with pressure.

Iron is still ferromagnetic up to 21.5 GPa, into the stability region of *hcp* phase, assumption of non-magnetic *hcp* Fe is impossible. It is possible that *hcp* Fe could be ferromagnetic initially, and then become non-ferromagnetic as pressure increases.

Table 2.1 Magnetic data for iron under pressure. P, average pressure; SIRM, saturation isothermal remanent magnetization; Bcr, coercivity of remanence; S_{corr} correction made to the SIRM data to account for the change in demagnetizing factor due to the increasing degree of oblateness. Ave D, the average diameter of the sample chamber.

Iron powder					
P (GPa)	SIRM (x10^9 Am^2)	Bcr (mT)	S_{corr} x10^{-3}	SIRM$_{norm}$	Ave D (µm, SD)
0.0	25.5	10.8	1.15	1.0	248(17)
2.5	42.8	10.8	1.15	1.5	243(19)
4.5	52.6	10.5	1.15	1.8	248(24)
6.3	64.9	12.3	1.32	2.0	261(31)
8.3	88.0	11.3	1.53	2.6	286(41)
10.2	109.3	11.4	1.74	3.1	306(43)
12.4	130.8	11.3	1.96	3.5	319(40)
14.5	148.3	10.8	1.98	3.9	334(74)
16.9	155.4	11.0	1.98	4.1	319(55)
19.2	140.2	11.8	1.98	3.7	323(43)
21.5	92.6	12.4	1.98	2.4	
18.2	93.4	12.1	1.98	2.4	
15.5	116.7	12.5	1.98	3.1	
13.0	179.9	11.1	1.98	4.7	
11.5	240.1	11.0	1.98	6.3	
8.7	281.6	11.7	1.98	7.4	
8.7	282.2	11.2	1.98	7.4	
7.5	275.8	10.9	1.98	7.2	
4.9	267.8	10.6	1.98	7.0	
1.9	232.9	9.8	1.98	6.1	
0.0	179.7	8.6	1.98	4.7	

To be continued

Continuing

Iron foil					
P (GPa)	SIRM (x10^9 Am^2)	Bcr (mT)	S_{corr}	Bcr_{corr}	$SIRM_{norm}$
0.9	11.8	45.3	1.15	0.17	1.0
4.3	17.7	41.2	1.15	0.19	1.2
7.4	42.3	36.5	1.43	0.21	2.3
7.1	36.4	31.5	1.43	0.24	1.7
4.5	31.8	26.5	1.43	0.28	1.4
0.4	27.0	27.7	1.43	0.27	1.4
4.8	36.7	35.1	1.43	0.22	2.1
7.7	47.6	35.1	1.47	0.22	2.5
10.0	74.1	28.2	1.72	0.26	2.9
12.1	105.8	23.6	1.94	0.31	3.3
13.9	142.5	18.1	1.98	0.39	3.3
16.5	158.4	13.6	1.98	0.49	2.8
18.9	159.9	12.0	1.98	0.55	2.5
20.5	158.8	10.7	1.98	0.61	2.2
20.0	157.6	10.1	1.98	0.64	2.1
18.9	152.5	9.7	1.98	0.66	1.9
17.2	155.2	9.5	1.98	0.67	1.9
15.6	160.4	9.8	1.98	0.65	2.0
12.6	189.2	11.6	1.98	0.56	2.8
10.2	235.8	20.0	1.98	0.35	6.1
12.4	242.9	20.2	1.98	0.35	6.3
15.5	253.6	22.0	1.98	0.33	7.2

Note: Ave D, the average diameter measured with a Leica DFC295 camera mounted on a Leica MZ12.5 stereomicroscope. Four length measurements, two along the maximum and minimum axes from the front and back sides of the cell, were made at each pressure. Standard deviations are in parentheses. Bcr_{corr}, Bcr correction made to the SIRM data for the foil assuming Bcr should be invariant with pressure following the empirical fit of the data in Figure 2.5 for h/d of 0.17 and 0.25-- $Bcr_{corr} = 4.6729*Bcr(P)^{-0.8624}$. $SIRM_{norm}$ is the SIRM normalized by the initial value after accounting for S_{corr} and Bcr_{corr}; e.g., $(SIRM_{P=n}/(S_{corr}*Bcr_{corr}))/(SIRM_{P=i}/(S_{corr}*Bcr_{corr}))$. Bcr_{corr} is 1 for the powder at all pressures.

Table 2.2 Magnetic data for iron disks measured with VSM. Angle, degree between the applied field and the plane of the disk; Bcr, coercivity of remanence; Mrs/Ms, ratio of remanent magnetization after saturation (Mrs) / saturation magnetization (Ms); Mrs, remanent magnetization after saturation, in units of emu/g. Dimension of one disk has a diameter (d) of 3 mm and height (h) of 0.25 mm (h/d = 0.083), measurement carried out on piled 1, 2, 3 and 10 iron disks.

Angle (°)	Bcr (mT)	Mrs/Ms (*10^{-4})	Mrs (emu/g)	Bcr (mT)	Mrs/Ms (*10^{-4})	Mrs (emu/g)	Bcr (mT)	Mrs/Ms (*10^{-4})	Mrs (emu/g)	Bcr (mT)	Mrs/Ms (*10^{-4})	Mrs (emu/g)
	h/d=0.083			h/d=0.167			h/d=0.250			h/d=0.833		
-100	51.2	9.4	0.19	50.2	6.5	0.19	33.3	7.7	0.19	19.5	9.6	0.31
-90	83.1	5.5	0.14	65.9	5.9	0.14	37.6	4.4	0.13	19.9	9.0	0.31
-80	43.8	5.1	0.16	54.9	6.1	0.16	26.0	4.9	0.17	19.5	9.0	0.31
-70	23.5	8.0	0.16	28.7	5.4	0.16	23.4	8.3	0.29	19.0	8.8	0.30
-60	18.4	11.7	0.26	29.2	8.9	0.26	21.6	9.4	0.31	18.4	9.0	0.29
-50	15.0	18.8	0.34	22.4	11.5	0.34	19.1	11.3	0.35	18.4	9.3	0.28
-40	13.0	24.0	0.42	19.5	14.8	0.42	16.1	12.6	0.36	18.8	9.6	0.27
-30	10.1	31.0	0.46	16.8	18.0	0.46	17.2	15.9	0.42	18.7	9.9	0.25
-20	9.0	34.7	0.49	14.7	21.0	0.49	16.9	17.8	0.41	19.3	9.8	0.22
-10	8.1	39.5	0.50	13.8	23.5	0.50	16.6	20.3	0.43	18.5	9.5	0.19
0	8.1	42.7	0.52	13.2	25.4	0.52	17.5	22.1	0.44	19.0	8.9	0.17
10	8.6	42.9	0.52	13.9	26.1	0.52	18.6	19.6	0.38	18.5	8.4	0.16
20	8.7	40.7	0.50	14.8	24.5	0.50	19.0	19.9	0.39	18.9	8.6	0.17
30	9.6	36.3	0.46	15.8	21.4	0.46	21.4	16.8	0.35	18.3	8.0	0.17
40	11.0	29.5	0.42	17.6	17.7	0.42	24.4	14.4	0.33	18.2	9.7	0.24
50	12.6	24.3	0.38	20.2	14.8	0.38	26.4	11.2	0.27			
60	16.5	18.2	0.30	22.5	11.0	0.30	30.4	9.7	0.24	20.4	9.8	0.30
70	25.1	13.8	0.24	32.8	8.4	0.24	35.9	8.9	0.22			
80	49.9	9.2	0.17	45.0	6.5	0.17	42.9	8.1	0.21	20.7	9.4	0.33
90	88.1	5.6	0.14	63.2	5.9	0.14	39.2	7.5	0.23			
100	63.2	7.4	0.17	57.5	6.2	0.17				20.1	9.0	0.33

3. Pressure dependence on the remanent magnetization of Fe-Ni alloys and Ni metal[2]

We measured the acquisition of magnetic remanence of iron-nickel alloys ($Fe_{64}Ni_{36}$, $Fe_{58}Ni_{42}$, and $Fe_{50}Ni_{50}$) and pure Ni under pressures up to 23 GPa at room temperature. Magnetization decreases markedly for $Fe_{64}Ni_{36}$ between 5 and 7 GPa yet remains ferromagnetic until at least 16 GPa. Magnetization rises by a factor of 2 - 3 for the other phases during compression to the highest applied pressures. Immediately upon decompression, magnetic remanence increases for all Fe-Ni compositions while magnetic coercivity remains fairly constant at relatively low values (5 - 20 mT). The amount of magnetization gained upon complete decompression correlates with the maximum pressure experienced by the sample. Martensitic effects best explain the increase in remanence rather than grain-size reduction, as the creation of single domain sized grains would raise the coercivity. The magnetic remanence of low Ni invar alloys increases faster with pressure than for other body centered cubic compositions due to the higher magnetostriction of the low Ni invar metals. Thermal demagnetization spectra of $Fe_{64}Ni_{36}$ measured after pressure cycling broaden as a function of peak pressure, with a systematic decrease in Curie temperature. Irreversible strain accumulation from the martensitic transition also likely explains the widening of the Curie temperature spectra, consistent with our X-ray diffraction analyses.

3.1 Introduction

After iron, metallic nickel comprises the second major constituent in the cores of terrestrial planets, as well as Earth’s moon and Jupiter’s moon Ganymede (Anderson, 1989; Bottke et al., 2006;

---

[2] *Part of the content published as: Wei, Q., Gilder, S.A., Maier, B., 2014. Pressure dependence on the remanent magnetization of Fe-Ni alloys and Ni metal. Physical Review B 90, 144425. doi:10.1103/PhysRevB.90.144425, 2014.*

Ringwood, 1966). Nickel concentrations vary from 5 to 60% in iron meteorites, which once formed the cores of differentiated proto-planets (Albertsen et al., 1983; Goldstein et al., 2009). As summarized by Reuter et al. (1989) and Goldstein et al. (2009), the phase diagram of Fe-Ni alloys at Earth-like ambient conditions depends largely on the cooling rate and the concentration of lighter elements (P, C, etc.). Iron-nickel metals with Ni concentrations lower than ~12% by weight have a body-centered cubic (*bcc*) structure while those above 51% Ni have face-centered cubic (*fcc*) structures. Phases in between 5-12% Ni and 51% Ni are metastable; they form in a miscibility gap with mixed *bcc* and *fcc* phases, although single *bcc* or *fcc* phases can be stabilized in the gap region when rapidly quenched. Compositions around $Fe_{64}Ni_{36}$ (*fcc*), called invar, exhibit near-null thermal expansion, making them useful for technological applications.

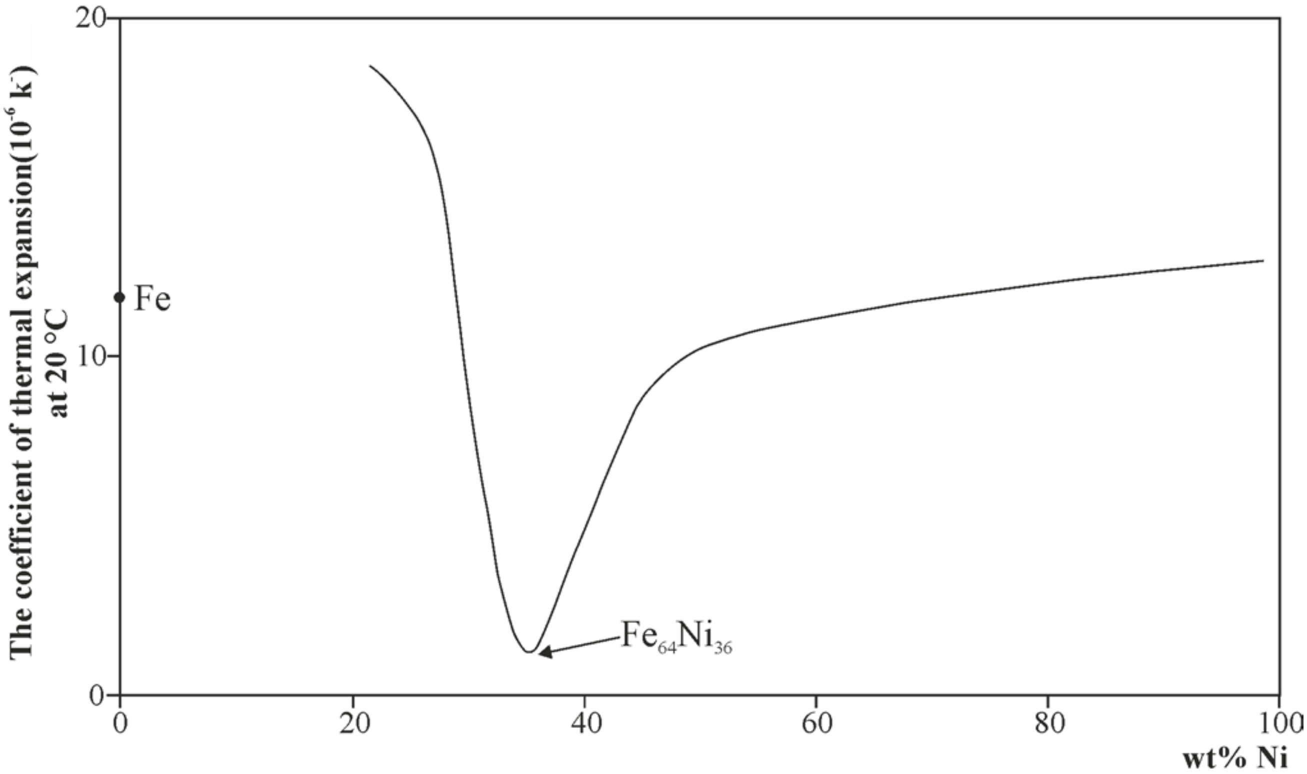

Figure 3.1 The thermal expansion coefficient of Fe-Ni alloys. (Based on image from http://de.academic.ru/pictures/dewiki/73/Invar-Graph-CTE-composition.png).

The magnetic moments of the Fe-Ni alloys systematically decrease from ca. 2.2 Bohr magnetons for pure Fe to ~0.6 in pure Ni, with a deflection at the invar compositions (Crangle and Hallam, 1963; Glaubitz et al., 2011). Magnetic susceptibility mimics this trend (Figure 3.2a). Curie temperatures of the *bcc* phases decrease from 770°C for pure Fe to 740°C for ~$Fe_{92}Ni_{10}$ then drop steeply above ca. 10% Ni (Figure 3.2b). Curie temperatures of the *fcc* phases are below room temperature for invar compositions with <30% Ni, then increase until attaining a maximum of ~570°C at $Fe_{30}Ni_{70}$, and then drop to ~370°C at Ni_{100} (Figure 3.2b) (Asano, 1969; Dubovka, 1974). Magnetocrystalline anisotropy and magnetostriction attain maxima at around 40% Ni in the *fcc* alloys (Bozorth and Walker, 1953).

Models explaining the invar effect (Figure 3.1) evoke magnetovolume effects (volume dependence on exchange interaction) that compensate for thermal expansion (Hausch, 1973; van Schilfgaarde et al., 1999; Weiss, 1963). Such models bear on the magnetic behavior of invar under pressure, as evinced by several experiments—most notably on the Curie temperature. Indeed, changes in Curie temperature with pressure goes from sharply negative at the low Ni invar compositions (-35 K/GPa for $Fe_{64}Ni_{36}$) to negative yet lower slopes as Ni increases (-29 and -21 K/GPa for $Fe_{58}Ni_{42}$ and $Fe_{50}Ni_{50}$); the slope becomes positive for *fcc* compositions above ca. 65% Ni and is 4 K/GPa for Ni_{100} (Hausch, 1973; Kouvel and Wilson, 1961; Leger et al., 1972b; Patrick, 1954). Mössbauer spectroscopy measured at 4.2 K on $Fe_{68.5}Ni_{31.5}$ and $Fe_{65}Ni_{35}$ show that hyperfine field distributions break down under pressure until collapsing by 5.8 GPa and 7 GPa, respectively (Abd-Elmeguid et al., 1988). X-ray emission spectroscopy of $Fe_{64}Ni_{36}$ under pressure at ambient temperature reveals that the amplitude of the Fe local magnetic moment changes in a two-step manner, once at 5 GPa and another at 15 GPa, above which any trace of ferromagnetic character was lost (Rueff et al., 2001). Orbital magnetic moments measured with X-ray magnetic circular dichroism (XMCD) under pressure on $Fe_{64}Ni_{36}$ decrease by 50% around 3-4 GPa then remain at that level until 10 GPa (Nataf et al., 2009). Using the extended X-ray absorption fine structure technique on $Fe_{65}Ni_{35}$, Matsumoto et al. (2011) found that the magnetic dichroic amplitude is highly suppressed by 6 GPa and disappears around 7 GPa. Matsumoto et al. (2011) ascribed the discrepancy with the results of Nataf et al. (2009) due to the martensitic nature of the transition.

In this paper, we document magnetic remanence measurements made under compression and decompression on $Fe_{64}Ni_{36}$, $Fe_{58}Ni_{42}$, $Fe_{50}Ni_{50}$ and Ni_{100} powders up to maximum pressures of 23.0 GPa. Because magnetovolume effects are greatest at invar compositions around $Fe_{64}Ni_{36}$, we anticipated finding magnetic remanence near that composition to be more pressure-sensitive than the rest. We also sought to confirm the negative slope in the Curie temperature by testing whether magnetization was lost at prescribed pressures. For example, $Fe_{64}Ni_{36}$ has a Curie temperature of

208°C at ambient pressure. Given that its Curie temperature decreases by 35 K/GPa, one would predict a complete loss in magnetization at about 5.2 GPa at room temperature.

3.2 Experimental Procedure and Results

Our experiments used polycrystalline samples of $Fe_{64}Ni_{36}$, $Fe_{58}Ni_{42}$, $Fe_{50}Ni_{50}$ and Ni_{100} (*Goodfellow*, purity >99.5%, max particle size 45 µm). Magnetic hysteresis loops measured on all samples with a Petersen Instruments, variable field translation balance at ambient conditions yield remanence ratios (remanent magnetization after saturation (Mrs) / saturation magnetization (Ms)) <0.1 and coercivity ratios (coercivity of remanence (Bcr) / bulk coercivity (Bc)) >7, characteristic of multidomain material. Curie temperatures measured with the same balance in a 30 mT field, and defined by the second derivative of the data, are 208°C, 343°C, 516°C and 358°C for $Fe_{64}Ni_{36}$, $Fe_{58}Ni_{42}$, $Fe_{50}Ni_{50}$ and Ni_{100}, respectively (Figure 3.2c and Figure 4.1). The decrease in magnetization occurs over several 10s of degrees for $Fe_{64}Ni_{36}$ and $Fe_{58}Ni_{42}$ (Figure 3.2c), which could indicate non-stoichiometry, yet their Curie temperatures are consistent with published values at the average compositions (Figure 3.2b) (Chuang et al., 1986; Crangle and Hallam, 1963; Dubovka, 1974; Swartzendruber et al., 1991). The other phases show sharper drops in moment with increasing temperature near the Curie temperature. Magnetic susceptibility (Bartington MS2) of the samples diluted in silica gel (~15% weight percent metal) decrease linearly from pure Fe ($50x10^{-5}$ m^3/kg) to pure Ni ($31x10^{-5}$ m^3/kg) with a deflection at $Fe_{64}Ni_{36}$ (Figure 3.2a), following the trend

in magnetic moment of the Fe-Ni alloys (Li et al., 1997; Swartzendruber et al., 1991). Powder x-ray diffraction using an x-ray source wavelength of 0.709 Å (Mo $k\alpha_1$) identifies solely *fcc* structures in all samples with no evidence for *bcc* or oxide phases (Figure 3.2d).

In each experiment, polycrystalline material was loaded together with ruby spheres and silica gel into a cylindrical chamber drilled in a work-hardened gasket that was contained within a pressure cell consisting of Be-Cu metal and moissanite anvils. Three independent experiments were made for $Fe_{64}Ni_{36}$-- two of them using 700 µm diameter culets with beryllium-copper gaskets (chamber size = diameter 390 µm, height 250 µm) and the third using 400 µm diameter culets with a rhenium gasket whose initial chamber dimensions were diameter 250 µm and height 175 µm. Experiments on $Fe_{58}Ni_{42}$, $Fe_{50}Ni_{50}$ and two on Ni_{100} (Ni-1 and Ni-2) used 400 µm culet diameter moissanite anvils

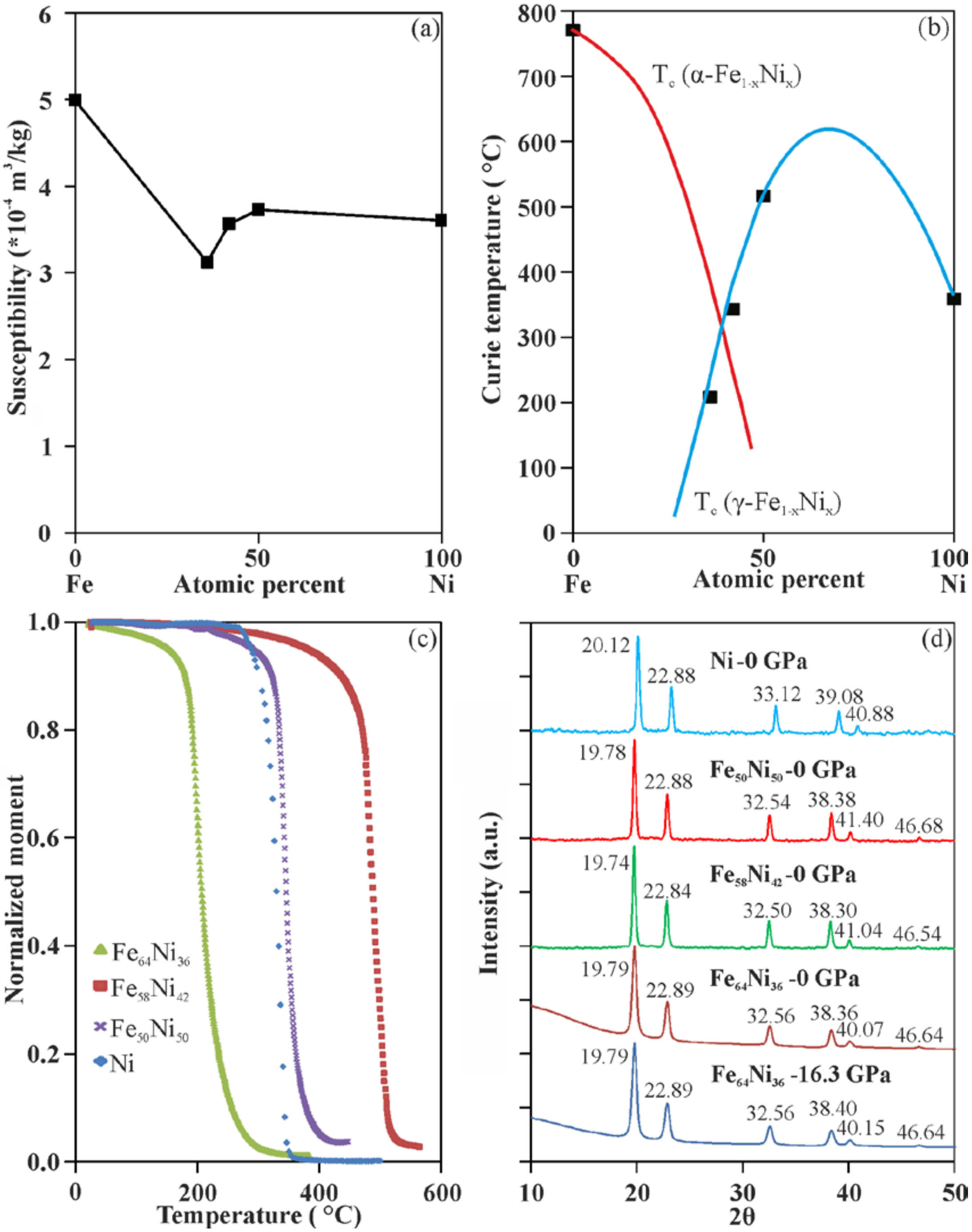

Figure 3.2 Magnetic and physical properties of the iron-nickel alloys. (**a**) Magnetic susceptibility; (**b**) Curie temperature trends for *bcc*, α-$Fe_{1-x}Ni_x$ (red curve- Chuang et al. (1986)) and *fcc*, γ-$Fe_{1-x}Ni_x$ (blue curve-Crangle and Hallam (1963)). Black squares represent the data from our samples derived from the second derivative of the curves in Figure 3.2c; (**c**) Magnetization normalized to the initial (room temperature) value versus temperature for the four Fe-Ni metals used in this study; (**d**) X-ray powder diffraction using a Mo-Kα_1 source (wavelength 0.709 Å) (top 3 spectra measured with a Stoe diffractometer; bottom two with an Agilent-Oxford Gemini A-Ultra diffractometer).

with rhenium gaskets containing cylindrical chambers of diameter 200 µm and height 160-180 µm. In each experiment, polycrystalline material was loaded together with ruby spheres and silica gel into a cylindrical chamber drilled in a work-hardened gasket that was contained within a pressure cell consisting of Be-Cu metal and moissanite anvils. Three independent experiments were made for $Fe_{64}Ni_{36}$-- two of them using 700 µm diameter culets with beryllium-copper gaskets (chamber size = diameter 390 µm, height 250 µm) and the third using 400 µm diameter culets with a rhenium gasket whose initial chamber dimensions were diameter 250 µm and height 175 µm. Experiments on $Fe_{58}Ni_{42}$, $Fe_{50}Ni_{50}$ and two on Ni_{100} (Ni-1 and Ni-2) used 400 µm culet diameter moissanite anvils with rhenium gaskets containing cylindrical chambers of diameter 200 µm and height 160-180 µm. Although less hydrostatic than some pressure media (methanol, etc.), silica gel is preferable because the sample can be loaded into the cell while insuring none rests outside the chamber. Pressure was measured before and after each experiment using ruby fluorescence spectroscopy with a Coherent, Cube 405 nm laser and a Princeton Instruments (PIXIS) charged coupled device connected to a 150 mm, ARC SpectraPro spectrometer. Rubies placed near the center and edge of the sample chamber helped monitor potential pressure gradients. Discussion below reports the average, not peak, pressures.

For each experiment at successive pressure steps, we measured the stepwise acquisition of isothermal remanent magnetization (Figure 3.3). A static field was directed perpendicular to the axis of the moissanite pistons with an electromagnet whose pole pieces slide through the cell's housing until they abut the pistons. First we applied a magnetic field of 370 mT along the –y axis direction. The cell was removed from the electromagnet and then placed into the bore of a 2G Enterprises Inc., three-axis, superconducting magnetometer to measure the full magnetic vector. This first data point is considered as a starting point (0 mT). We then stepwise increased the applied field intensity in the +y axis direction until reaching 370 mT, each time measuring the corresponding remanence with the magnetometer. The same type of experiment is made before loading the sample into the gasket in order to measure the contribution from the empty cell. These data are subtracted from the back-field curves measured with the loaded cell (Figure 3.3). Once completed, the pressure is raised or lowered and then the process is repeated on the same sample. Two magnetic parameters can be extracted from the backfield curves: the coercivity of remanence (Bcr), defined as the magnetic field in mT required to null the remanent magnetization, and the saturation isothermal remanent magnetization (SIRM, in units of Am^2), which is defined here as the average moment from the last three steps of the backfield curves. This definition assumes the sample becomes fully saturated by the last three steps, consistent with the data. The goal is to see how Bcr and SIRM change as a function of pressure.

In the first experiment on $Fe_{64}Ni_{36}$, pressure was progressively raised to 7.5 GPa and then progressively decompressed to ambient conditions. In the second experiment, we again progressively compressed to 7.2 GPa, whereafter the pressure was lost and the experiment was aborted (no decompression path). In the third experiment, we stepwise compressed the sample to 16.3 GPa and then stepwise decompressed to ambient conditions. $Fe_{58}Ni_{42}$ and $Fe_{50}Ni_{50}$ were progressively compressed to 20.3 and 23.0 GPa respectively and then progressively decompressed back to ambient conditions. For Ni_{100}, the two experiments reached maximum pressures of 11.0 GPa and 17.2 GPa (Ni-1 and Ni-2) that were progressively decompressed to ambient conditions. A secondary pressure cycle between 17.2 and 13.2 GPa was made for Ni-2.

Figure 3.4 plots the relative change in SIRM ($SIRM_{norm}$ in Table 3.1) and the absolute change in Bcr as function of pressure at room temperature. Magnetization is mass dependent whereas coercivity is not. Because the samples' masses are unknown in our experiments, relative values are used for SIRM in order to compare the results. The SIRM data require a shape correction because sample geometry influences magnetization intensity depending on the degree of oblateness and the direction of the applied field relative to the plane of the oblate spheroid (Wei and Gilder, 2013). For this reason we measured the horizontal cell dimensions (front and back sides) at each pressure step with a Leica MZ12.5 microscope fitted with a DSC295 digital camera (1 µm resolution) (Table 3.1).

The initial height to diameter ratio (h/d) of the sample chambers ranged from 0.5-0.9. Those <0.8 already deviate from spherical isotropy. Higher pressures decrease h/d, resulting in higher degrees of oblateness and lower demagnetization factors in the long axis direction. Because the applied field direction lies along the long axis of the sample, increasing the maximum to minimum axis ratio will have the apparent effect of decreasing Bcr while increasing SIRM (Dunlop and Özdemir, 1997). We can correct for the change in demagnetization factor by normalizing the SIRM values for the change in shape (S_{corr}) via a power function $S_{corr}= 8.36\text{x}10^{-4}(h/d)^{-0.66}$ (Wei and Gilder, 2013). In other words, if h/d is flattened from 0.8 to 0.3, a sample will have 1.9 times greater SIRM and 20% lower Bcr in the long axis plane. Sample geometry changes insignificantly during decompression with respect to that obtained at the highest pressure, so changes in magnetization observed along the decompression path can be directly compared with respect to the highest pressure step. The shape contribution was accounted for in all SIRM data in Figure 3.4. Those data are used in the subsequent discussion.

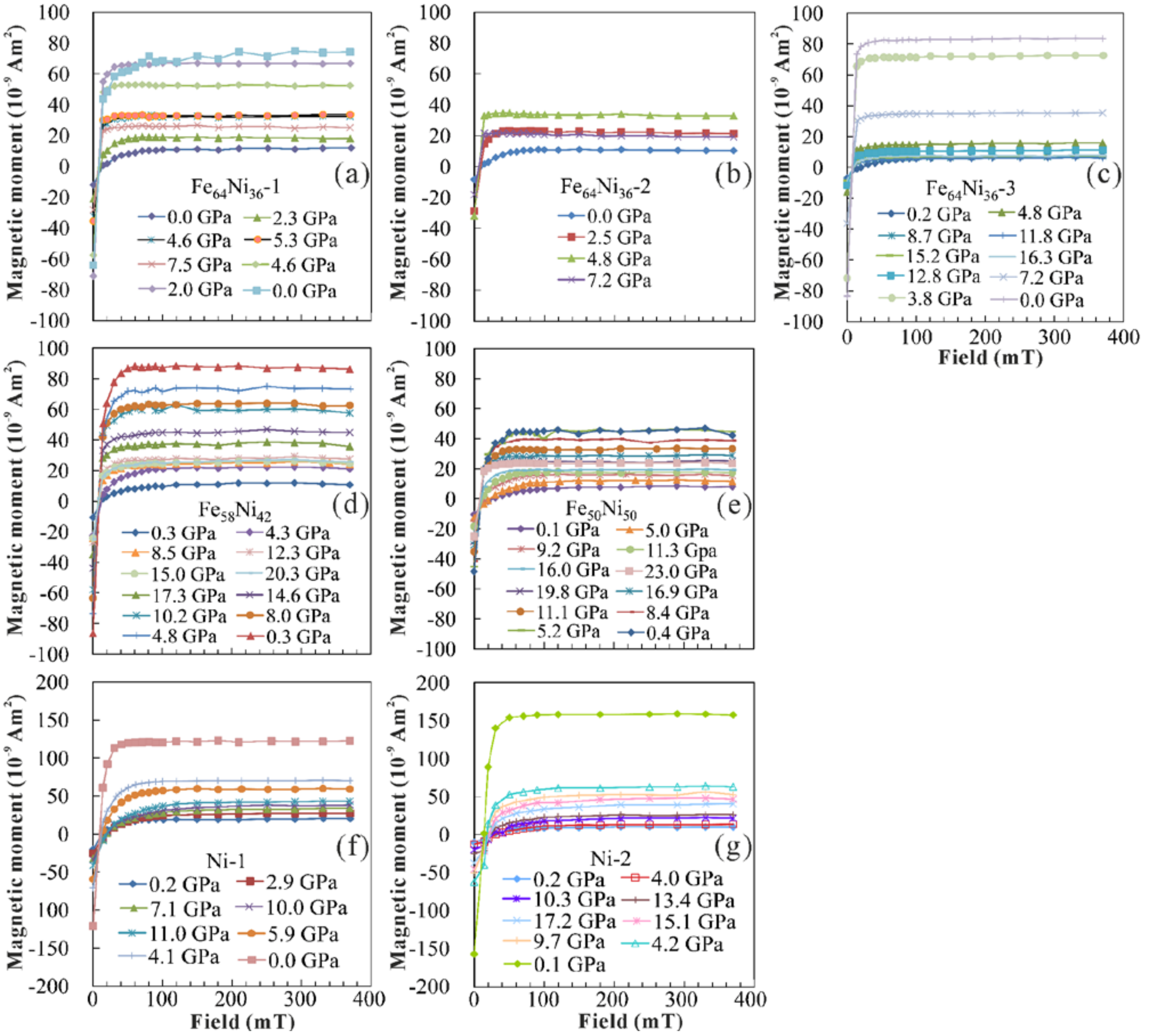

Figure 3.3 Backfield magnetization curves for iron-nickel alloys and nickel. (**a-c**) Backfield magnetization curves for three independent experiments on $Fe_{64}Ni_{36}$ powder. (**d-g**) Backfield magnetization curves for $Fe_{58}Ni_{42}$, $Fe_{50}Ni_{50}$, Ni-1 and Ni-2 powder, respectively. Some pressure steps are omitted to make the curves visible/distinguishable; all pressure steps are given in Table 3.1. Labels showed in figures is in sequence of top to bottom.

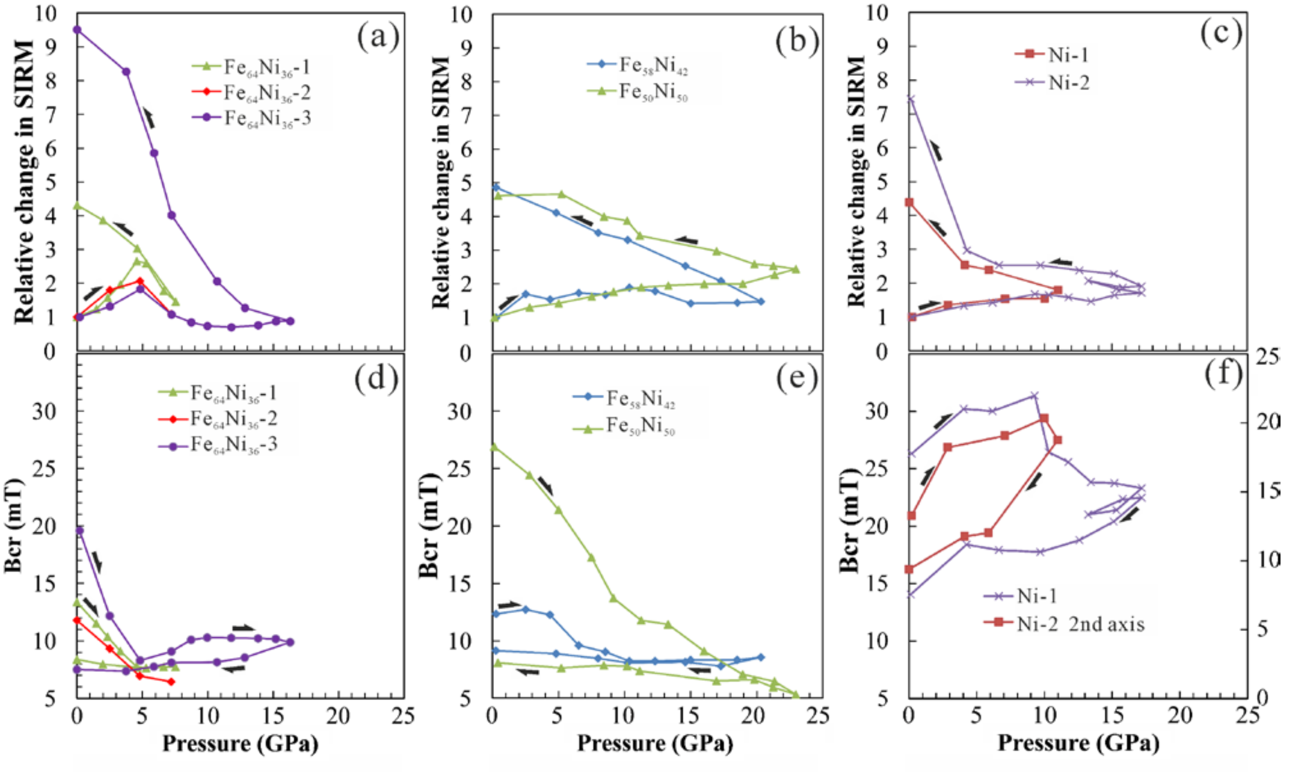

Figure 3.4 SIRM and Bcr as function of pressure for iron-nickel alloys and nickel. (**a-c**) Normalized saturation isothermal remanent magnetization (SIRM), and (**d-f**) coercivity of remanence (Bcr) as function of pressure for $Fe_{64}Ni_{36}$, $Fe_{58}Ni_{42}$, $Fe_{50}Ni_{50}$, Ni-1 and Ni-2. SIRM was normalized after shape correction. Arrows indicate the pressure path; data from Table 3.1.

The three experiments on $Fe_{64}Ni_{36}$ show a high degree of reproducibility with a two to three fold increase in SIRM by 5 GPa, whereafter SIRM decreases to near-initial (pre-compression) values by 6-7 GPa. That SIRM decreases above ca. 5 GPa should be expected based on prior work suggesting the Curie temperature decreases by 35 K/GPa. Experiment #3 that goes to the highest pressure contains our most unexpected observations as the magnetization significantly increases immediately upon decompression-- by 10.7 GPa, the magnetization is already two times greater than the initial value. In all experiments with $Fe_{64}Ni_{36}$, Bcr decreases until 5 GPa whereafter it remains fairly constant, including upon decompression. Because the applied magnetic field increments are 15, 20, 30, 40,... mT, uncertainties on the Bcr data depend on the magnetization intensity crossing the y axis going from negative to positive values. We cannot achieve fields lower than 15 mT due to an intrinsic, permanent remanence of the electromagnet.

SIRM of $Fe_{58}Ni_{42}$ increases two fold until ~11 GPa, whereafter it slightly decreases upon further compression. SIRM moments of $Fe_{50}Ni_{50}$ and Ni_{100} increase fairly continuously with pressure during compression; all phases exhibit significant increases in magnetization upon decompression. Magnetization for $Fe_{58}Ni_{42}$ and $Fe_{50}Ni_{50}$ increases fairly linearly upon decompression, becoming 4-5 times stronger than initially. In contrast SIRM of Ni increases abruptly at the last decompression step. Typical of most magnetic phases, the amount of increase upon full decompression relative to starting depends on the maximum pressure. Bcr for $Fe_{58}Ni_{42}$ and $Fe_{50}Ni_{50}$ decreases with increasing pressure until plateauing; it stays low and fairly constant upon decompression. Bcr for Ni_{100} increases until 10 GPa, followed by a continuous decrease. For the invar compositions, up to 20% of the initial decrease in Bcr can be attributed to changes in shape, which is not accounted for in Figure 3.4.

3.3 Discussion

3.3.1 Magnetization and Curie temperature

All three experiments on $Fe_{64}Ni_{36}$ show a marked decrease in magnetization from 5 to 7 GPa, which is consistent among most studies of similar composition regardless of technique used to quantify magnetic effects under pressure (Abd-Elmeguid et al., 1988; Hausch, 1973; Leger et al., 1972a; Matsumoto et al., 2011; Nataf et al., 2009; Rueff et al., 2001). That magnetization remains finite well above 7 GPa matches the results of Rueff et al. (2001) and Nataf et al. (2009). Unlike previous work, we also measured magnetization during decompression; the marked increase in magnetization during the initial stages of decompression at 12.7 and 10.8 GPa appears to be a new finding. The slight increase in SIRM during compression beginning at 13 GPa is likely significant and should be further explored to higher pressures.

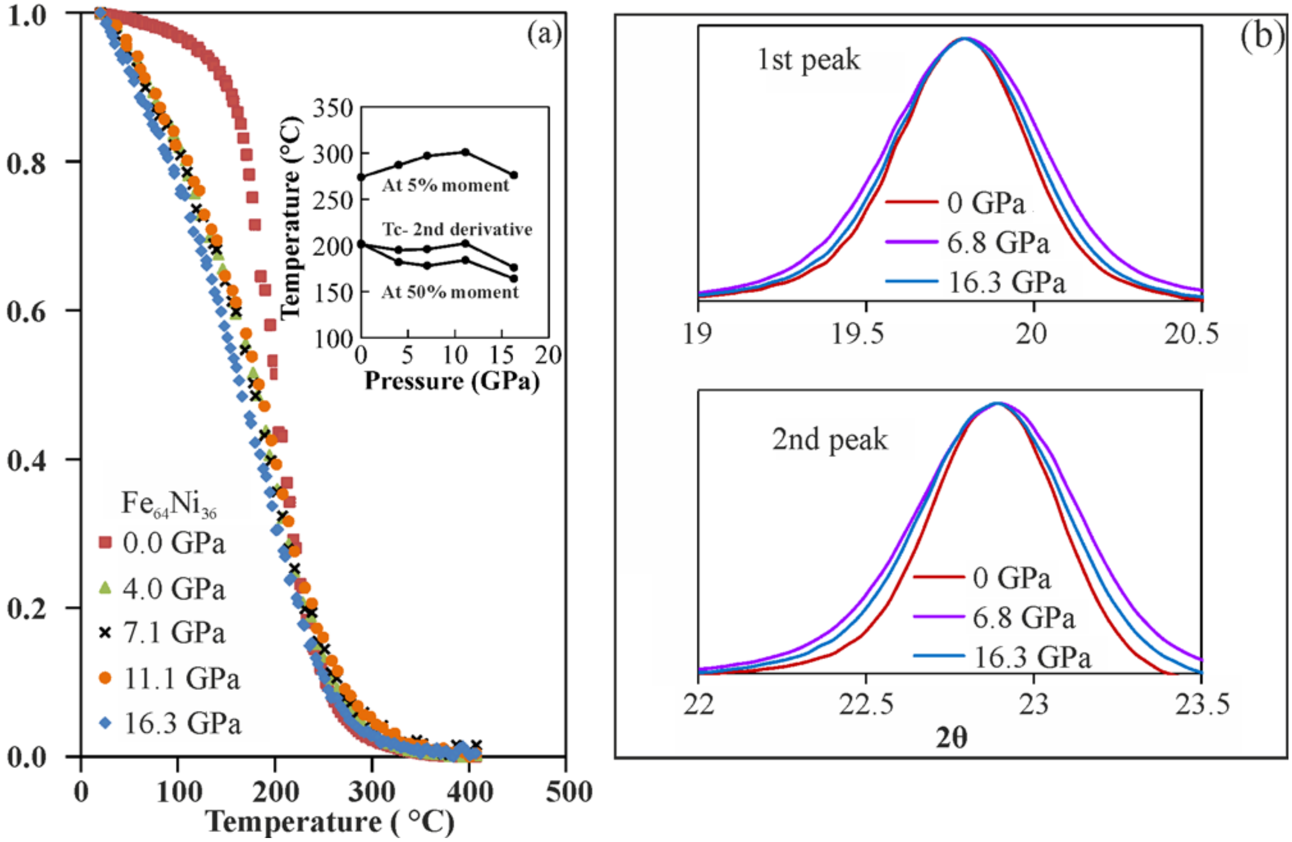

Figure 3.5 Curie temperature and X-ray spectra of pressure cycled $Fe_{64}Ni_{36}$. (**a**) Remanent magnetization normalized to the initial (25°C) value versus temperature for $Fe_{64}Ni_{36}$ at 0 GPa (starting material) and discrete samples measured after decompression from the indicated peak pressure. The inset shows the temperature after 50 and 95% loss in magnetization as a function of pressure. (**b**) Comparison of the first and second peaks between the non-compressed (0 GPa) sample with two that pressure cycled peak pressures of 6.8 GPa and 16.3 GPa- the one to 16.3 GPa was measured after heating to 407°C; and that to 6.8 GPa was never heated.

What could cause the increase in magnetization during decompression? Using a high-energy ball mill, (Gorria et al., 2009) mechanically stressed $Fe_{64}Ni_{36}$ powder for 30 hours. They found that the strained invar had a 150 K higher Curie temperature (650 K) than the non-strained equivalent (500 K). From neutron diffraction spectra, they found that the lattice parameter of the strained invar slightly increased Fe-Fe interatomic distances. We therefore postulated that the pressure cycling in our experiments likewise raised the Curie temperature, thereby accounting for our decompression data. To test this, we pressurized several sub-samples of $Fe_{64}Ni_{36}$ to different peak pressures (4.0, 7.1, 11.1 and 16.3 GPa) and measured their Curie temperatures after decompression (Figure 3.5a).

Pressure cycling broadens the spectra. Seen at 50% decay in magnetization, the Curie temperature obviously decreases with increasing pressure; whereas at 95% decay, Curie temperatures generally rise. Defining the Curie temperature using the second derivative resembles the trend at 50% decay.

A comparison of X-ray diffraction patterns between the pressure-cycled (16.3 GPa) and non-compressed samples reveals virtually identical peak positions yet are broader for the strained sample (Figure 3.2d and 3.4b). This could be due to grain size reduction; however if this were the case, we would expect coercivity (Bcr) to increase since reduced grain sizes should shift multidomain material toward the single domain state. Another possibility is that martinsitic effects from strain accounts for the X-ray peak broadening and the smearing out of the Curie temperatures (Figure 3.5a). Likely strain-induced martensitic effects explain the enhanced magnetization during decompression around 10 to 13 GPa. In this way, the higher the maximum pressure, the greater the effect.

Curie temperatures change at a rate of -29 and -21 K/GPa for $Fe_{58}Ni_{42}$ and $Fe_{50}Ni_{50}$, which predicts a loss in magnetization at room temperature at ~11.0 and 23.4 GPa. For $Fe_{58}Ni_{42}$, we do observe slightly diminished SIRMs above 10 GPa compared to those below 10 GPa during compression, somewhat mimicking the curves for $Fe_{64}Ni_{36}$. We likely did not reach high enough pressures to see a measurable decrease in SIRM for $Fe_{50}Ni_{50}$. We interpret the enhanced magnetizations during decompression again to martensitic effects.

3.3.2 Magnetovolume effects on magnetic remanence

With some exception, pressure raises the remanent saturation magnetization of multidomain Fe-Ni alloys and Ni, both upon compression and especially upon decompression (Figure 3.4), as it does for titanomagnetite, pyrrhotite and pure iron (Gilder and Le Goff, 2008; Gilder et al., 2011; Wei and Gilder, 2013). A marked difference between the magnetic behavior with high pressure for Fe-Ni metals (ferromagnets) versus iron oxides or iron sulphides (ferrimagnets) is that coercivity decreases or changes little in ferromagnets, yet, with few exceptions, markedly increases in ferrimagnets.

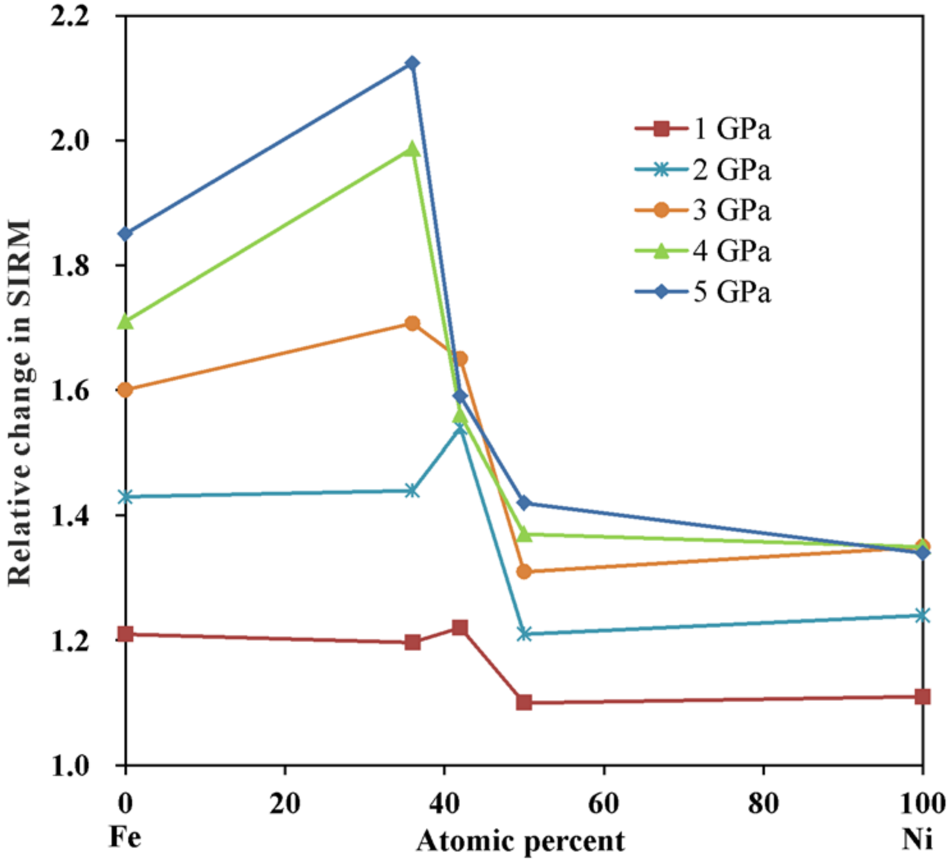

Figure 3.6 Normalized saturation isothermal remanent magnetization (SIRM) versus Ni concentration during compression to 5 GPa for Fe, Fe-Ni alloys, and Ni. Pure iron data from Wei and Gilder (2013).

Stress can influence magnetization by raising the magnetic anisotropy energy (E_{anis}), where $E_{anis} = (3/2)\lambda_s\sigma\bullet\cos^2\theta$, with λ_s being the net magnetostriction constant, σ the applied stress, and θ, the angle between the magnetization vector of the grain relative to the applied stress direction (Kittel, 1949). From this equation one would predict that the magnetizations of materials possessing higher magnetostriction coefficients will be more stress-sensitive. For example, in the iron-titanium oxide solid solution series (titanomagnetite) ($Fe_{3-x}Ti_xO_4$, with x from 0 to 1), an abrupt rise in magnetostriction occurs when x exceeds 0.2 (Syono, 1965), which coincides with pressure-induced changes in magnetization (see Figure 12 in Gilder and Le Goff (2005)). Hence, one would also predict that the magnetization of the invar phases that possess higher magnetostriction coefficients than other Fe-Ni alloys will be more sensitive to an imposed stress. This is indeed what we observe

(Figure 3.6)—an equivalent imposed stress has a greater relative effect on the magnetizations of $Fe_{58}Ni_{42}$ and $Fe_{64}Ni_{36}$ than the other alloys.

3.4 Conclusions

Our experiments show that pressure generally enhances the remanent magnetization intensities of Fe-Ni alloys and Ni at room temperature, whereas magnetic coercivity initially decreases then remains constant at relatively low values (~ <20 mT). If the increase in remanent magnetization were due to a decrease in magnetic grain size, going from multidomain to a more single domain like state, then one would expect coercivity to increase—opposite to what we observe. Increased magnetic interactions could decrease coercivity, but magnetic interactions would also lower the slope in magnetization approaching saturation (Cisowski, 1981), which is likewise not observed. The widening of the X-ray diffraction spectra can be explained either by a decrease in grain size or by an increase in strain. Given the sum of our results, the latter should be preferred, thus we conclude that the diffusionless, structural transition produced by internal shear (martensitic transformation) in the metal best accounts for the changes in magnetic remanence for all Fe-Ni metals.

Why the magnetic remanence significantly increases upon decompression in the third experiment on $Fe_{64}Ni_{36}$ remains unknown, but it is also likely due to martensitic effects. Cycling to sequentially higher pressures can test this. The implications are that the energy governing the process that enhances the magnetization largely exceeds the effect causing the decrease around 6 GPa. Gorria et al. (2009) interpreted the suppression due to an increase in Curie temperature. Our results contradict this explanation although the strains imposed in our experiments are much more hydrostatic than in Gorria et al. (2009). Further experiments exploring how non-hydrostatic stresses influence the Curie temperature should bear interesting results. Future work should also ascertain the pressure when the increase in magnetic remanence ceases for *fcc* phases with high Ni concentrations.

Table 3.1 Magnetic data for iron-nickel alloys and pure nickel under pressure. P_{ave}, average pressure; P_{max}, maximum pressure; SIRM, saturation isothermal remanent magnetization; Bcr, coercivity of remanence

P_{ave} (GPa)	P_{max} (GPa)	SIRM ($\times 10^9 Am^2$)	Bcr (mT)	S_{corr} $\times 10^{-3}$	$SIRM_{norm}$	h/d
			$Fe_{64}Ni_{36}$-1			
0.0	0.0	11.6	13.4	1.2	1.0	0.6
1.5	1.5	14.3	11.5	1.2	1.2	0.6
2.3	2.6	18.2	10.3	1.2	1.6	0.6
3.3	3.7	22.7	9.1	1.2	2.0	0.6
4.6	5.2	32.5	7.8	1.2	2.7	0.6
5.3	6.3	33.4	7.6	1.3	2.6	0.5
6.6	8.1	29.3	7.7	1.7	1.8	0.4
7.5	9.4	25.1	7.7	1.7	1.5	0.3
4.6	5.7	52.3	7.7	1.7	3.0	0.3
2.0	2.6	66.6	8.0	1.7	3.9	0.3
0.0	0.0	74.3	8.4	1.7	4.3	0.3
			$Fe_{64}Ni_{36}$-2			
0.0	0.0	10.4	11.8	1.1	1.0	0.7
2.5	2.8	21.4	9.3	1.3	1.8	0.5
4.8	5.9	32.9	6.9	1.7	2.1	0.3
7.2	9.2	19.2	6.4	1.7	1.1	0.3
			$Fe_{64}Ni_{36}$-3			
0.2	0.2	7.0	19.6	1.1	1.0	0.7
2.5	2.6	9.7	12.2	1.1	1.3	0.6
4.8	5.0	15.8	8.3	1.3	1.8	0.5
7.2	7.4	9.3	9.1	1.3	1.1	0.5
8.7	9.0	7.3	10.1	1.3	0.8	0.5
10.0	10.5	6.4	10.3	1.4	0.7	0.5
11.8	12.7	6.1	10.3	1.4	0.7	0.5
13.8	15.0	6.6	10.2	1.4	0.8	0.5
15.2	16.8	7.6	10.2	1.4	0.9	0.5
16.3	18.7	7.7	9.9	1.4	0.9	0.5
12.8	15.4	11.1	8.5	1.4	1.3	0.5
10.7	12.3	18.1	8.1	1.4	2.1	0.5
7.2	9.0	35.3	8.1	1.4	4.0	0.5
5.9	7.2	51.4	7.8	1.4	5.9	0.5
3.8	4.6	72.6	7.4	1.4	8.3	0.5
0.0	0.0	83.5	7.5	1.4	9.5	0.5

To be continued

Continuing

P_{ave} (GPa)	P_{max} (GPa)	SIRM ($\times10^9$Am^2)	Bcr (mT)	S_{corr} $\times10^{-3}$	$SIRM_{norm}$	h/d
			$Fe_{58}Ni_{42}$			
0.3	0.3	11.3	12.3	1.00	1.00	0.8
2.5	2.6	19.2	12.7	1.00	1.70	0.8
4.3	4.6	21.8	12.3	1.25	1.50	0.5
6.5	6.7	25.0	9.6	1.27	1.70	0.5
8.5	9.1	24.9	9.0	1.31	1.70	0.5
10.4	10.6	29.0	8.2	1.35	1.90	0.5
12.3	12.7	28.3	8.2	1.39	1.80	0.5
15.0	15.8	25.3	8.3	1.57	1.40	0.4
18.5	20.4	25.7	8.3	1.57	1.40	0.4
20.3	22.7	26.4	8.6	1.57	1.50	0.4
17.3	19.6	37.2	7.8	1.57	2.10	0.4
14.6	17.1	45.2	8.2	1.57	2.50	0.4
10.2	12.2	59.1	8.1	1.57	3.30	0.4
8.0	9.5	62.9	8.5	1.57	3.50	0.4
4.8	5.6	73.5	8.9	1.57	4.10	0.4
0.3	0.3	86.9	9.2	1.57	4.90	0.4
			$Fe_{50}Ni_{50}$			
0.1	0.1	8.1	26.9	0.93	1.00	0.9
2.8	2.9	10.8	24.4	0.95	1.30	0.8
5.0	5.2	12.1	21.4	0.97	1.40	0.8
7.5	7.6	14.0	17.3	0.99	1.60	0.8
9.2	9.3	15.8	13.7	1.03	1.80	0.7
11.3	11.4	17.5	11.8	1.06	1.90	0.7
13.3	13.5	18.5	11.4	1.09	1.90	0.7
16.0	16.5	19.5	9.1	1.12	2.00	0.6
18.9	19.6	19.5	7.1	1.12	2.00	0.6
21.3	22.2	22.1	6.5	1.12	2.30	0.6
23.0	24.0	23.8	5.3	1.12	2.40	0.6
21.2	22.7	24.7	6.0	1.12	2.50	0.6
19.8	21.2	25.2	6.6	1.12	2.60	0.6
16.9	17.9	29.0	6.5	1.12	3.00	0.6
11.1	12.3	33.5	7.4	1.12	3.40	0.6
10.2	11.4	37.8	7.8	1.12	3.90	0.6
8.4	9.3	39.0	7.9	1.12	4.00	0.6
5.2	6.1	45.5	7.6	1.12	4.70	0.6
0.4	0.4	45.1	8.1	1.12	4.60	0.6

To be continued

Continuing

P_{ave} (GPa)	P_{max} (GPa)	SIRM ($\times10^{9}$Am^{2})	Bcr (mT)	S_{corr} $\times10^{-3}$	$SIRM_{norm}$	h/d
			Ni-1			
0.2	0.2	20.0	13.3	0.91	1.0	0.9
2.9	3.1	27.1	18.2	0.91	1.4	0.9
7.1	7.5	33.4	19.1	1.14	1.3	0.6
10.0	10.6	41.3	20.3	1.31	1.4	0.5
11.0	13.2	42.9	18.8	1.35	1.5	0.5
5.9	6.6	59.3	12.0	1.02	2.7	0.7
4.1	4.6	70.4	11.8	1.02	3.2	0.7
0.0	0.0	122.0	9.4	1.02	5.5	0.7
			Ni-2			
0.2	0.2	9.8	26.3	0.90	1.0	0.8
4.0	4.1	13.0	30.2	0.90	1.3	0.8
6.2	6.2	14.3	30.0	1.00	1.4	0.8
9.3	9.6	18.5	31.4	1.10	1.7	0.7
10.3	10.7	21.7	26.4	1.30	1.7	0.5
11.8	12.5	23.8	25.6	1.40	1.6	0.4
13.4	14.5	25.7	23.8	1.70	1.5	0.3
15.2	16.9	29.9	23.7	1.70	1.6	0.3
17.2	19.6	33.5	23.3	1.90	1.7	0.3
15.3	17.7	37.1	21.4	1.90	1.8	0.3
13.2	15.6	42.0	21.0	1.90	2.1	0.3
15.8	18.0	38.0	22.4	1.90	1.9	0.3
17.2	19.7	39.8	22.5	2.00	1.9	0.3
15.1	17.9	47.3	20.4	2.00	2.3	0.3
12.6	15.3	50.2	18.8	2.00	2.4	0.3
9.7	12.0	53.6	17.8	2.00	2.5	0.3
6.6	8.3	53.8	17.9	2.00	2.5	0.3
4.2	4.8	63.0	18.4	2.00	3.0	0.3
0.1	0.1	158.3	14.1	2.00	7.4	0.3

Abbreviations are: P_{ave}, average pressure; P_{max}, maximum pressure; SIRM, saturation isothermal remanent magnetization; Bcr, coercivity of remanence; S_{corr}, correction made to the SIRM data to account for the change in demagnetizing factor due to the increasing degree of oblateness. $SIRM_{norm}$ is the SIRM normalized by the initial value after accounting for S_{corr}, e.g., $(SIRM_{p=n}/S_{corr})/(SIRM_{p=i}/S_{corr})$. h/d, height to average diameter ratio of sample chamber.

4. Magnetism of body-centered cubic Fe-Ni and Fe-Si alloys under high pressure[3]

We measured the acquisition of magnetic remanence of body-centered cubic Fe-Ni alloys ($Fe_{92}Ni_{08}$, $Fe_{87}Ni_{13}$, and $Fe_{84}Ni_{16}$) and Fe-Si alloys ($Fe_{91}Si_{09}$, and $Fe_{83}Si_{17}$) under pressures up to 24.1 GPa at room temperature. Magnetization of $Fe_{92}Ni_{08}$, $Fe_{87}Ni_{13}$, and $Fe_{84}Ni_{16}$ increases and then decreases with pressure at 15.1 GPa, and still ferromagnetic up to 24.1 GPa, which the Fe-Ni alloys are already in hexagonal-close-packed structure at room temperature. Magnetization of $Fe_{91}Si_{09}$, and $Fe_{83}Si_{17}$ increases with pressure up to the maximum pressure of experiments 21.9 GPa, the body-centered cubic structure is stabilized by silicon to pressure higher than our maximum pressure of experiments. The magnetic coercivity of remanence increases greatly between 10-15 GPa for Fe-Ni alloys; and keeps constant at relatively low values (9-13 mT) under pressure for Fe-Si alloys, at room temperature.

4.1 Introduction

After iron, metallic nickel comprises the second major constituent in the cores of terrestrial planets, as well as Earth’s moon and Jupiter’s moon Ganymede (Anderson, 1989; Bottke et al., 2006; Ringwood, 1966). Nickel concentrations vary from 5 to 60% in iron meteorites, which once formed the cores of differentiated proto-planets (Albertsen et al., 1983; Goldstein et al., 2009). Silicon is one of favored candidates as lighter elements in Earth’s outer core (Li and Fei, 2007; Poirier, 1994) and also in Earth’s inner core (Badro et al., 2006; Kuwayama et al., 2009; Lin et al., 2005; Liu et al., 2014).

---

[3] *Preparing for publication.*

Pure iron has a body-centered cubic (*bcc*) structure at ambient condition, and has a hexagonal-closed-packed (*hcp*) structure at room temperature above 13 GPa (Takahashi and Bassett, 1964). For Fe-rich Fe-Ni alloys, face-centered cubic (*fcc*) structure is stabilized at high pressure and high temperature (Huang et al., 1988; Lin et al., 2002; Mao et al., 2006). At room temperature, phase transition pressure from *bcc* to *hcp* lowered to ~11 GPa and ~8 GPa for 10% Ni and 25% Ni Fe-Ni alloys (Huang et al., 1988). For Fe-rich Fe-Si alloys, *bcc* structure is stabilized at higher P-T conditions with slight Si alloyed into iron at high pressure and temperature (Fischer et al., 2012; Fischer et al., 2013; Lin et al., 2009; Lin et al., 2002). At room temperature, phase transition pressure in range 16-36 GPa for 8-9% Si Fe-Si alloys (Hirao et al., 2004; Lin, 2003); and no phase transition occur up to 124 GPa for 17.8% Si Fe-Si alloy (Hirao et al., 2004).

Magnetic remanence of pure iron increases with pressure at room temperature until 14-17 GPa for iron foil and powder respectively (Wei and Gilder, 2013), and then decreases with pressure when pressure goes even higher; the transition pressure of pressure versus magnetic remanence is consistent with the pressure of *bcc*-to-*hcp* phase transition for iron at room temperature. The difference on phase changing pressures at room temperature for Fe-Ni and Fe-Si alloys, because of the nickel and silicon alloying effect, maybe also revealed by their magnetization under pressure. In this paper, we document magnetic measurements made under compression and decompression on Fe-Ni alloys ($Fe_{92}Ni_{08}$, $Fe_{87}Ni_{13}$, and $Fe_{84}Ni_{16}$) up to 19.4-24.1 GPa, and on Fe-Si alloys ($Fe_{91}Si_{09}$, and $Fe_{83}Si_{17}$) up to 19.3-21.9 GPa, at room temperature.

4.2 Experimental Procedure and Results

Iron (Sigma-Aldrich, 97% pure) and nickel powders (Goodfellow, purity >99.5%) were mixed in Ni atomic percent of 6%, 10% and 15%, and synthesized at 1600 °C in an argon atmosphere for more than 1 hour, then quenched in an alumina crucible. Electron probe analysis shows atomic Ni percentage of 8.4 ± 0.7 % , 12.7 ± 0.9 % and 16.4 ± 0.8 % in the alloys, which are named $Fe_{92}Ni_{08}$, $Fe_{87}Ni_{13}$, and $Fe_{84}Ni_{16}$ respectively. In the experiments, many small pieces (each about 80 µm in length) of $Fe_{92}Ni_{08}$, $Fe_{87}Ni_{13}$, and $Fe_{84}Ni_{16}$ were used; $Fe_{91}Si_{09}$, and $Fe_{83}Si_{17}$ (Goodfellow) samples are polycrystalline, with maximum particle sizes of 45 µm. Magnetic hysteresis loops measured on a PCM Micromag 3900 vibrating sample magnetometer at room temperature yield remanence ratios (remanent magnetization after saturation [Mrs] / saturation magnetization [Ms]) <0.02 and coercivity ratios (coercivity of remanence [Bcr] / bulk coercivity [Bc]) >3.6, characteristic of multidomain material. Curie temperatures measured with a Petersen Instruments, variable field translation balance in a 30 mT field, and defined by the second derivative of the data, are 723 °C, 674 °C, 625 °C, 648 °C and 416 °C (Figure 4.1) for $Fe_{92}Ni_{08}$, $Fe_{87}Ni_{13}$, $Fe_{84}Ni_{16}$, $Fe_{91}Si_{09}$, and $Fe_{83}Si_{17}$ respectively. The Curie temperature of $Fe_{92}Ni_{08}$, $Fe_{87}Ni_{13}$, and $Fe_{84}Ni_{16}$ decrease with Ni concentration increasing, which is consistent with the calculated Curie temperature of the *bcc* Fe-Ni alloys (Chuang et al., 1986), indicating *bcc* phase dominated in samples. Powder x-ray diffraction using an x-ray source wavelength of 0.709 Å (Mo kα1) identifies solely *bcc* structure for $Fe_{91}Si_{09}$, and $Fe_{83}Si_{17}$ powder (Figure 4.2).

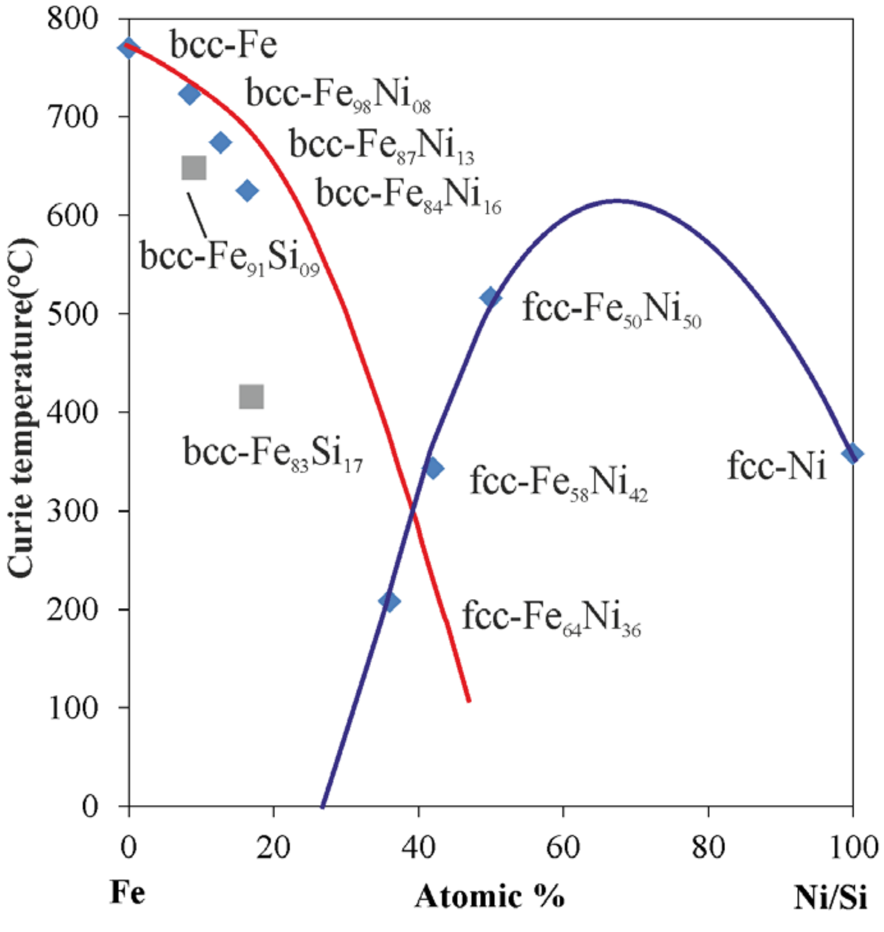

Figure 4.1 Curie temperature of Fe-Ni and Fe-Si alloys at ambient pressure. Blue diamonds represent Fe-Ni alloys; gray squares represent Fe-Si alloys, derived from the second derivative *fcc* Fe-Ni alloys and Ni data from Wei et al. (2014). Curie temperature trends for *bcc* (red curve- Chuang et al. (1986)) and *fcc* (blue curve- Crangle and Hallam (1963)).

In each experiment, the sample was loaded together with ruby spheres and silica gel into a cylindrical chamber drilled in a rhenium gasket that was contained within a pressure cell consisting of Be-Cu metal and moissanite anvils. The culet diameter of moissanite anvils is about ~400 µm. Rhenium gasket of initial thickness 250 µm pre-compressed to thickness of 150-180 µm for creating a indentation; then a hole of diameter 150-200 µm was drilled in the center as sample chamber. Although less hydrostatic than some pressure media (methanol, etc.), silica gel is preferable because the sample can be loaded into the cell while insuring none rests outside the chamber. Pressure was measured before and after each experiment using ruby fluorescence spectroscopy with a Coherent, Cube 405 nm laser and a Princeton Instruments (PIXIS) charged coupled device connected to a 150 mm, ARC SpectraPro spectrometer. Rubies placed near the center and edge of the sample chamber helped monitor potential pressure gradients. Discussion below reports the average, not peak, pressures.

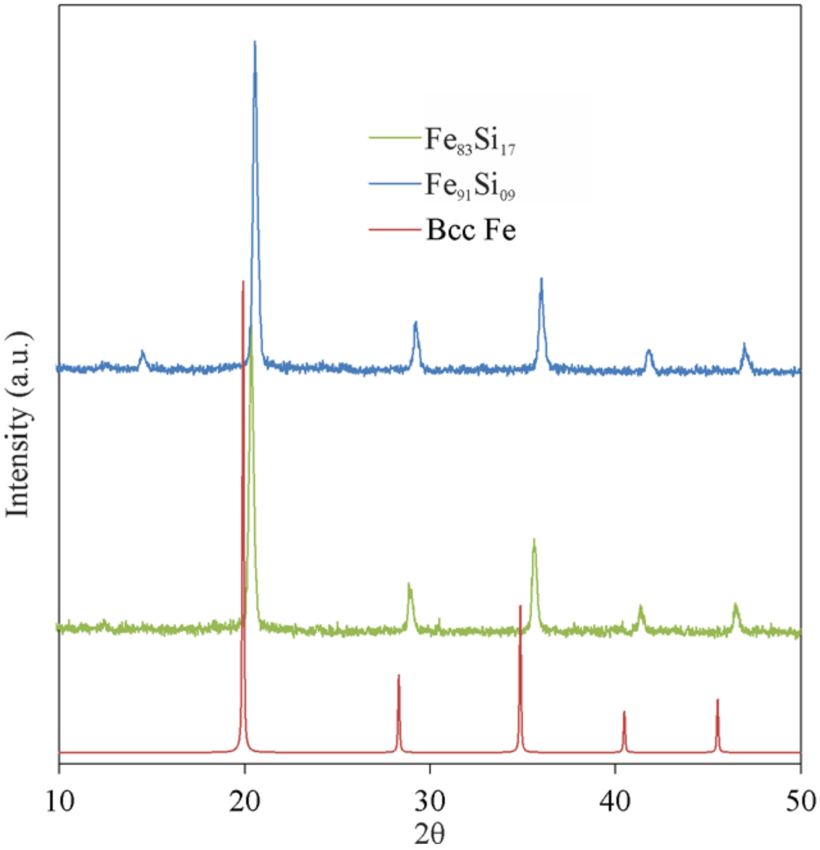

Figure 4.2 X-ray diffraction pattern of Fe-Si alloys. X-ray powder diffraction using a Mo-Kα_1 source (wavelength 0.709 Å), with a Stoe diffractometer. *Bcc* Fe is simulated X-ray diffraction signal corresponding Mo-Kα_1 source.

For each experiment at successive pressure steps, we measured the stepwise acquisition of isothermal remanent magnetization (Figures 4.3 and 4.4). A static field was directed perpendicular to the axis of the moissanite pistons with an electromagnet whose pole pieces slide through the cell's housing until they abut the pistons. First we applied a magnetic field of 370 mT along the –y axis direction. The cell was removed from the electromagnet and then placed into the bore of a 2G Enterprises Inc., three-axis, superconducting quantum interference device (SQUID) magnetometer to measure the full magnetic vector. This first data point is considered as a starting point (0 mT). We then stepwise increased the applied field intensity in the +y axis direction until reaching 370 mT, each time measuring the corresponding remanence with the magnetometer. The same type of experiment is made before loading the sample into the gasket in order to measure the contribution from the empty cell. These data are subtracted from the back-field curves measured with the loaded cell (Figure 4.3 and Figure 4.4). Once completed, the pressure is raised or lowered and then the process is repeated on the same sample. Two magnetic parameters can be extracted from the backfield curves: the coercivity of remanence (Bcr), defined as the magnetic field in mT required to null the remanent magnetization, and the saturation isothermal remanent magnetization (SIRM, in units of Am^2), which is defined here as the average moment from the last three steps of the backfield curves. This definition assumes the sample becomes fully saturated by the last three steps, consistent with the data. The goal is to see how Bcr and SIRM change as a function of pressure.

Measured data showed in Table 4.1. In experiments pressure were progressively raised to maximum of 19.3-24.1 GPa for $Fe_{92}Ni_{08}$, $Fe_{87}Ni_{13}$, $Fe_{84}Ni_{16}$, $Fe_{91}Si_{09}$ and $Fe_{83}Si_{17}$ and then progressively decompressed to ambient conditions. Figure 4.5 plot the relative change in SIRM ($SIRM_{norm}$ in Table 4.1) and the absolute change in Bcr as function of pressure at room temperature. Magnetization is mass dependent whereas coercivity is not. Because the samples' masses are unknown in our experiments, relative values are used for SIRM in order to compare the results. The SIRM data require a shape correction because sample geometry influences magnetization intensity depending on the degree of oblateness and the direction of the applied field relative to the plane of the oblate spheroid (Wei and Gilder, 2013). For this reason we measured the horizontal cell dimensions (front and back sides) at each pressure step with a Leica MZ12.5 microscope fitted with a DSC295 digital camera (1 µm resolution).

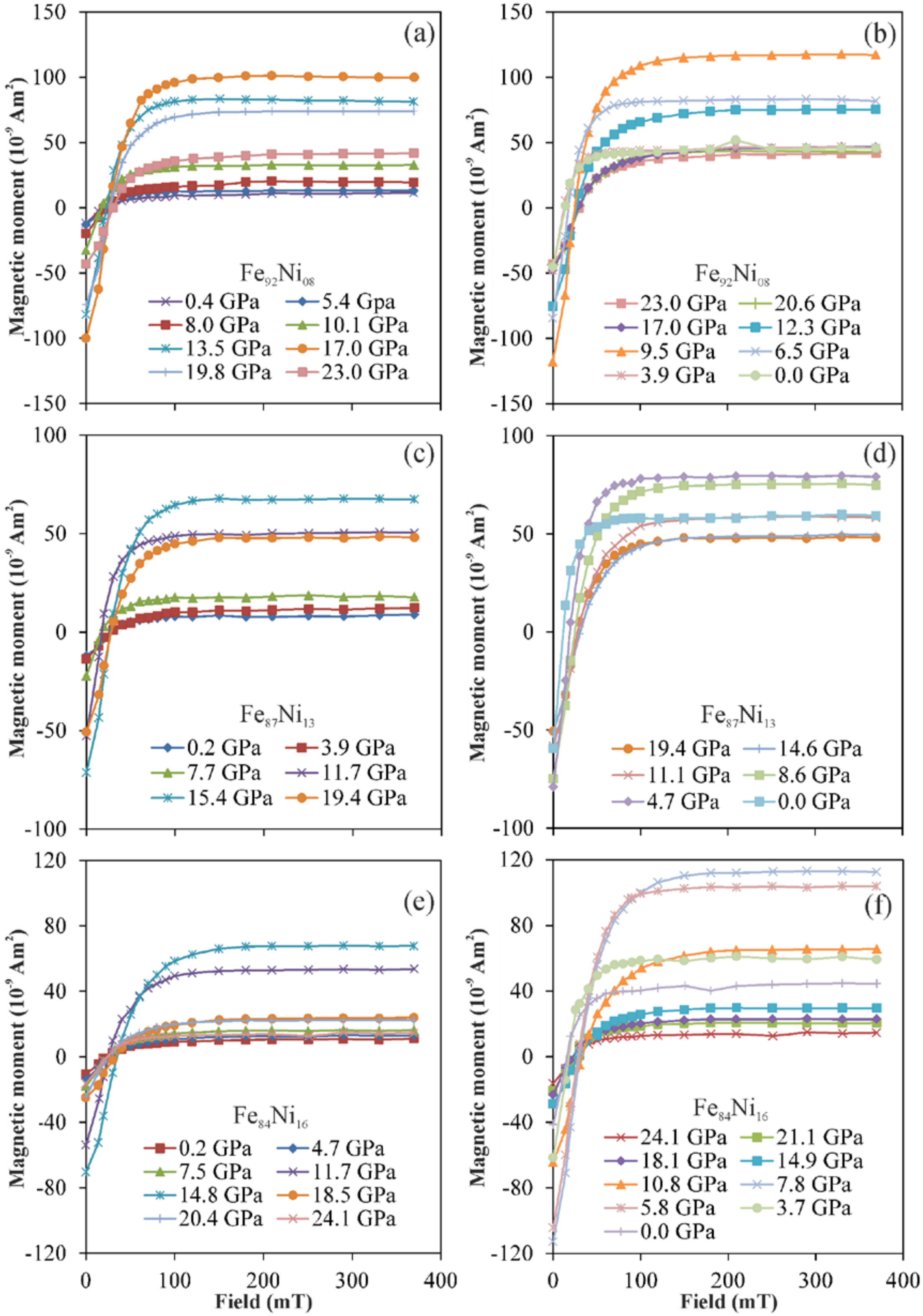

Figure 4.3 Backfield magnetization curves of Fe-Ni alloys. (**a-b**) Backfield magnetization curves for Fe$_{92}$Ni$_{08}$. (**c-d**) Backfield magnetization curves for Fe$_{87}$Ni$_{13}$. (**e-f**) Backfield magnetization curves for Fe$_{84}$Ni$_{16}$. All data from Table 4.1.

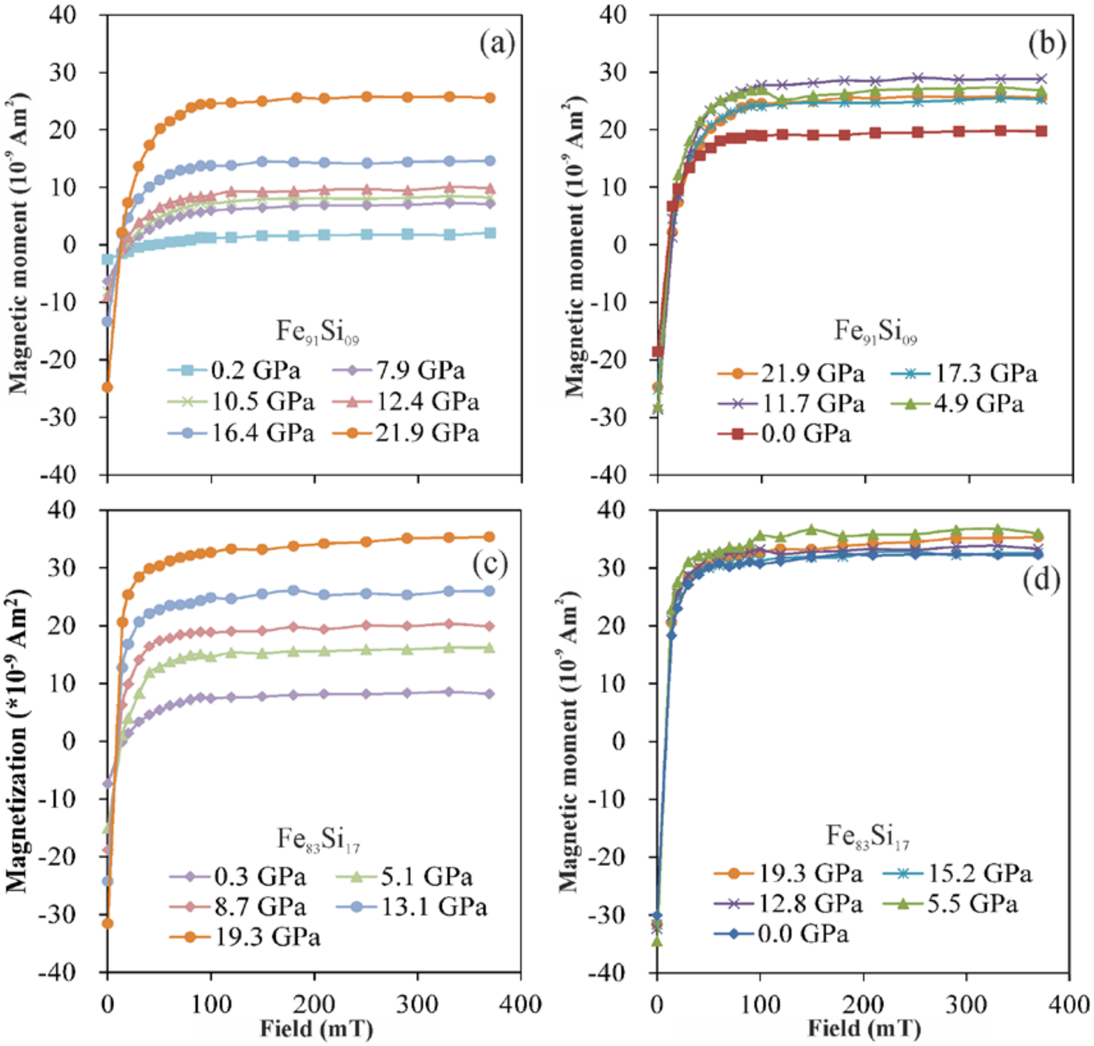

Figure 4.4 Backfield magnetization curves of Fe-Si alloys.. (**a-b**) Backfield magnetization curves for $Fe_{91}Si_{09}$ powder. (**c-d**) Backfield magnetization curves for $Fe_{83}Si_{17}$ powder. All data from Table 4.1.

The initial height to diameter ratio (h/d) of the sample chambers ranged from 0.8-1.0. Higher pressures decrease h/d, resulting in higher degrees of oblateness and lower demagnetization factors in the long axis direction. Because the applied field direction lies along the long axis of the sample, increasing the maximum to minimum axis ratio will have the apparent effect of decreasing Bcr while increasing SIRM (Dunlop and Özdemir, 1997). We can correct for the change in demagnetization factor by normalizing the SIRM values for the change in shape (S_{corr}) via a power function $S_{corr}= 8.36x10^{-4}(h/d)^{-0.66}$ (Wei and Gilder, 2013). In other words, if h/d is flattened from 0.8 to 0.3, a sample will have 1.9 times greater SIRM and 20% lower Bcr in the long axis plane. Sample geometry changes insignificantly during decompression with respect to that obtained at the highest pressure, so changes in magnetization observed along the decompression path can be directly compared with respect to the highest pressure step. The shape contribution was accounted for in SIRM data in Figure 4.4a and Figure 4.4c. Those data are used in the subsequent discussion.

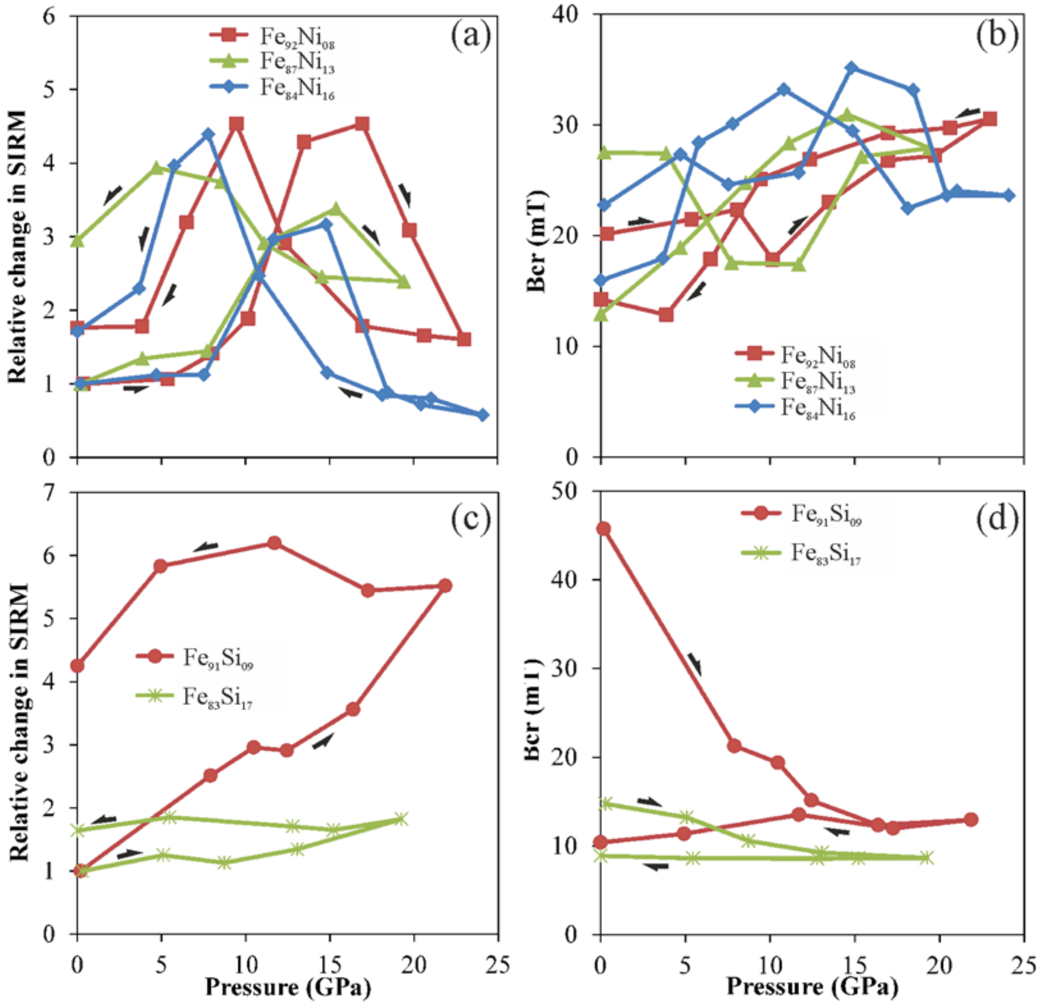

Figure 4.5 SIRM and Bcr for Fe-Ni and Fe-Si alloys. (**a**) Normalized saturation isothermal remanent magnetization (SIRM) and (**b**) coercivity of remanence (Bcr) as function of pressure for $Fe_{92}Ni_{08}$, $Fe_{87}Ni_{13}$ and $Fe_{84}Ni_{16}$. (**c**) Normalized saturation isothermal remanent magnetization (SIRM), and (**d**) coercivity of remanence (Bcr) as function of pressure for $Fe_{91}Si_{09}$ and $Fe_{83}Si_{17}$. SIRM was normalized after shape correction. Arrows indicate the pressure path; data from Table **4.1**. It should be noted that the SIRM data for $Fe_{91}Si_{09}$ is preliminary as the moment at 0 GPa was equal to the cell. Because the relative change in SIRM highly depends on this first point, an independent experiment is underway to calibrate this curve. Once this is done, the results can be considered final.

The experiments for $Fe_{92}Ni_{08}$, $Fe_{87}Ni_{13}$ and $Fe_{84}Ni_{16}$ show SIRM (Figure 4.4a) increases until 17-15 GPa with ~4 times to initial values during compression steps; SIRM starts increases with pressure decreasing until 10-5 GPa with also ~4 times to initial values during decompression steps; at their maximum pressure steps SIRM are 1.6, 2.4 and 0.6 times to initial values. In compression steps Bcr has sharp decrease around 8-4 GPa and starts to increase again around 10-12 GPa; Bcr decrease again for $Fe_{87}Ni_{13}$ and $Fe_{84}Ni_{16}$ around 15 GPa. With pressure decrease in decompression steps, Bcr decrease for $Fe_{92}Ni_{08}$; while Bcr for $Fe_{87}Ni_{13}$ and $Fe_{84}Ni_{16}$ first increase and then starts to decrease at around 11-15 GPa. The decrease in Bcr at lower pressure during compression can be attributed to changes in shape, which is not accounted for in Figure 4.4b.

The experiments for $Fe_{91}Si_{09}$ and $Fe_{83}Si_{17}$ show SIRM increases with pressure with 5.5-1.8 times to initial values (Figure 4.5c) at their maximum pressure steps during compression; SIRM slight increased higher and then decrease again with pressure decrease during decompression steps. Bcr of $Fe_{91}Si_{09}$ and $Fe_{83}Si_{17}$ decrease at low pressure steps during compression and show fairly constant value (9-13 mT) when pressure up to 16-13 GPa and whole decompression steps. The sharp decrease in Bcr at lower pressure during compression can be attributed to changes in shape, which is not accounted for in Figure 4.5d. The very high Bcr of $Fe_{91}Si_{09}$ at the first step (0.2 GPa) is partially contributed from empty cell, because of the relative low magnetization of the sample compared to the empty cell. A final correction must be made to account for the volume contribution to the moment in each cell as a function of pressure. For example, the median pressure in the cell, taken at on-half the total radius means that 1/3 of the volume is above the median pressure and 2/3 is below. This volumetric correction will be performed before final submission.

4.3 Discussion

Fe-Ni alloys

The starting pressure of *bcc*-to-*hcp* phase transition is about 1-5 GPa lower (Figure 4.6c) for Fe-Ni alloys (Huang et al., 1988) than pure iron (Takahashi and Bassett, 1964). At room temperature, complete *bcc*-to-*hcp* phase transition for pure iron is ~17.8 ± 0.8 GPa, when using NaCl pressure medium in diamond anvil cell (Von Barge and Boehler, 1990). Silica gel, used as pressure medium in our experiments, is more hydrostatic than NaCl (Klotz et al., 2009), implying completion transition pressures should be lower than 17.8 GPa. Our data shows that $Fe_{92}Ni_{08}$, $Fe_{87}Ni_{13}$ and

$Fe_{84}Ni_{16}$ are still ferromagnetic up to 24.1 GPa. The results are highly consistent and comparable with *hcp*-Fe (Figure 2.2c) up to 21.5 GPa (Wei and Gilder, 2013), in these experiments the same experimental methods and moissanite anvil cell was used. Like ferromagnetic *hcp* Fe, ferromagnetic *hcp* Fe-Ni alloys could be ferromagnetic initially and the magnetization disappear when pressure is high, the magnetization could be caused by distorted structure around martensitic transition zone (Bassett and Huang, 1987; Wang and Ingalls, 1998).

Figure 4.5a shows that SIRM vs pressure curves are hysteretic for compression and decompression paths; in the compression paths, SIRM starts decreasing at 16.2 GPa, 14.6 GPa, and 12.9 GPa for $Fe_{92}Ni_{08}$, $Fe_{87}Ni_{13}$ and $Fe_{84}Ni_{16}$ respectively; and in the decompression paths, SIRM starts decreasing at 9.5 GPa, 4.7 GPa, and 7.8 GPa for $Fe_{92}Ni_{08}$, $Fe_{87}Ni_{13}$ and $Fe_{84}Ni_{16}$ respectively (Figure 4.6). Figure 4.6 shows that the change in transition pressure decreases with increasing nickel concentration. Pressures corresponding to the *bcc*-to-*hcp* phase transition starting versus nickel concentration also decreases as nickel concentration increases; it is known that the *bcc*/*hcp* phase transition in iron is hysteretic for compression and decompression paths (Taylor et al., 1991). It indicates that the discontinuity in pressure induced SIRM for Fe-Ni alloys is related to the phase transition. On the other hand it indicates that at same pressure the pressure induced SIRM changing for *bcc* and *hcp* phase of Fe-Ni alloy is different: magnetization of *bcc* Fe-Ni alloys will increase with pressure and magnetization of *hcp* Fe-Ni alloys will decrease with pressure.

Synchrotron Mössbauer spectroscopy on *hcp*-$Fe_{92}Ni_{08}$ at 21 GPa under room temperature and 11 K was interpreted as non-magnetic (Papandrew et al., 2006), just like Mössbauer spectroscopy did not find magnetism of *hcp*-Fe (Cort et al., 1982; Nasu et al., 2002; Pipkorn et al., 1964; Taylor, 1982). X-ray magnetic circular dichroism (XMCD) technique combined with X-ray absorption and emission spectroscopy (Iota et al., 2007; Mathon et al., 2004) also did not find a magnetic signal for *hcp*-Fe, while X-ray emission spectroscopy found that magnetic *hcp*-Fe persists up to 30 GPa (Rueff et al., 2008) and 43 GPa (Monza et al., 2011). It needs to be mentioned that Mössbauer spectroscopy reveals the magnetic field around the atoms, >7 Tesla (Nasu et al., 2002); X-ray magnetic circular dichroism (XMCD), X-ray absorption and emission spectroscopy reveals the magnetic field around the atoms at the sample's surface. The relationship between magnetization around atoms and net magnetization may not linearly related. Magnetization around atoms of *hcp*-Fe could be so weak that Mössbauer spectroscopy, XMCD and X-ray absorption spectroscopy techniques are too insensitive to detect a signal, whereas a net magnetization persists and remains above detection limits.

Bcr of $Fe_{92}Ni_{08}$, $Fe_{87}Ni_{13}$ and $Fe_{84}Ni_{16}$ increases with pressure (Figure 4.5b). Pressure induced Bcr increases was also found for pure Ni (Figure 3.4f), while the Bcr of Fe and $Fe_{64}Ni_{36}$ are relatively constant (Figure 2.2b and Figure 3.4d) with pressure. The reason for pressure induced Bcr changes is unclear.

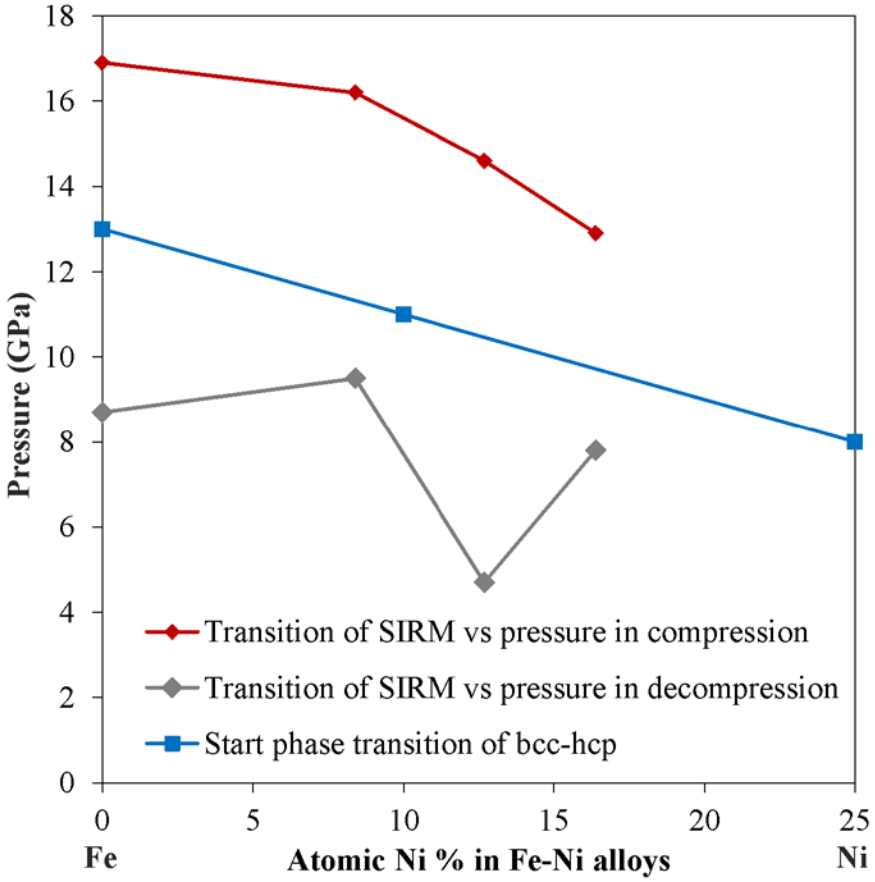

Figure 4.6 Transition pressures for Fe and Fe-Ni alloys. Blue squares are pressures for initial *bcc*-out to *hcp*-in during compression (Huang et al., 1988), phase transition pressure of *bcc-hcp* iron data is from Von Barge and Boehler (1990). Red diamonds (this study) are transition of SIRM vs pressure during compression; and gray diamonds (this study) are transition of SIRM vs pressure during decompression.

Fe-Si alloys

The relative increase in SIRM of $Fe_{91}Si_{09}$ and $Fe_{83}Si_{17}$ (Figure 4.5c) with pressure up to 21.9 GPa and 19.3 GPa exhibits no sign of phase change like seen in the iron rich Fe-Ni alloys. This is likely because silicon stabilizes the *bcc* phase to pressures higher than the maximum pressure in our experiments (Hirao et al., 2004; Lin, 2003). The slight decrease in SIRM at 12.4 GPa and 8.7 GPa for $Fe_{91}Si_{09}$ and $Fe_{83}Si_{17}$ respectively could be attributed to uncertainty in the shape anisotropy correction (Table 4.1).

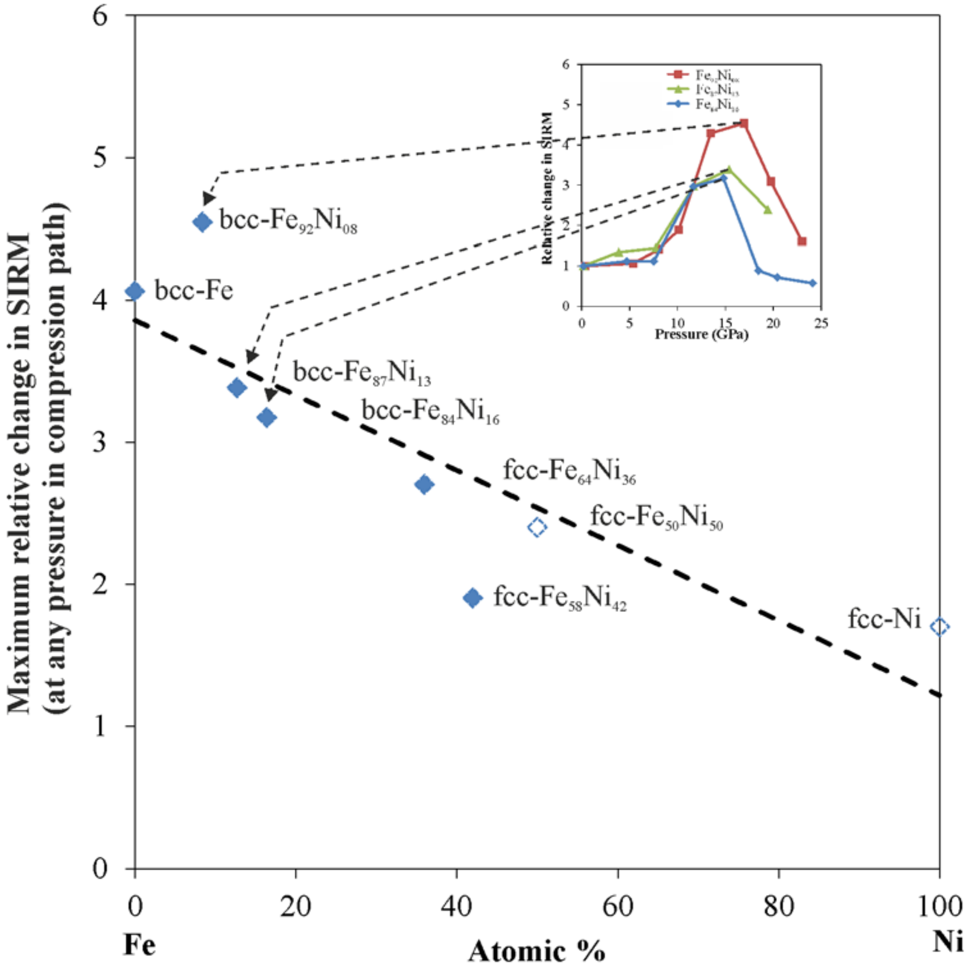

Figure 4.7 Maximum relative changing in SIRM of Fe-Ni alloys. Maximum relative changing in SIRM data is at any pressure in their compression path: for *bcc* phase $Fe_{92}Ni_{08}$, $Fe_{87}Ni_{13}$ and $Fe_{84}Ni_{16}$ (this study) are at pressure of 16.2 GPa, 14.6 GPa, and 12.9 GPa respectively, also showed in Figure 4.5(a) and Table 4.1; for *bcc*-Fe is at 16.9 GPa for iron powder, also shown in Figure 2.2(c) and Table 2.1, and in Wei and Gilder (2013); for *fcc* phase $Fe_{64}Ni_{36}$, $Fe_{58}Ni_{42}$, $Fe_{50}Ni_{50}$, Ni are at 4.6 GPa ($Fe_{64}Ni_{36}$ -1), 10.4 GPa, 23.0 GPa, and 17.2 GPa (Ni-2) respectively, which also showed in Figure 3.4 (a-c) and Table 3.1. SIRM of $Fe_{50}Ni_{50}$ and Ni increases with pressure, so their maximum SIRM is unknown, here SIRM values at our maximum experimental pressures are used, and in Wei et al. (2014). Dash line is a trend line based on all points.

SIRM of Fe-Ni alloys and Fe-Si alloys in *bcc* phase enhanced by pressure, as it also does for titanomagnetite (Gilder and Le Goff, 2008), pyrrhotite (Gilder et al., 2011), pure iron (Wei and Gilder, 2013), *fcc* Fe-Ni alloys and Ni (Wei et al., 2014). The increase in SIRM could be attributed to an increase in the magnetic anisotropy energy, which is likely augmented by strain (Wei et al., 2014) under pressure. The enhancement effect on different materials (Figure 4.7) show that the maximum relative change in SIRM decrease linearly as more Ni is incorporated into iron, from 4.1 for pure iron to 1.7 for pure nickel. Interestingly, this consistent with their relative magnetic moments at ambient condition. The magnetic moments of the Fe-Ni, Fe-Si alloys systematically decrease from ~2.2 Bohr magnetons for pure Fe to ~0.6 in pure Ni, and ~0 in pure Si (Crangle and Hallam, 1963; Glaubitz et al., 2011; Marchal et al., 1977). The amplitude of the pressure enhancement on SIRM for Fe, Fe-Ni alloys, Fe-Si alloys, and Ni is Bohr magnetons related.

4.4 Conclusions

Our experiments data shows that at room temperature, hexagonal close packed structure (*hcp*) Fe-Ni alloys are ferromagnetic up to 24.1 GPa; saturation isothermal remanent magnetization (SIRM) is enhanced with pressure for body-centered structure (*bcc*) Fe-Ni and Fe-Si alloys; and saturation isothermal remanent magnetization (SIRM) decrease with pressure for hexagonal close packed structure (*hcp*) Fe-Ni alloys. The coercivity of remanence (Bcr) increases with pressure for Fe-Ni alloys; and keep constant with pressure for Fe-Si alloys.

The maximum SIRM at any pressure during compression for Fe, Fe-Ni alloys, Fe-Si alloy and Ni, regardless their phase, is related to the number of Bohr magnetons.

Magnetization changing is usually following after the structural changing, further experiments exploring on Fe-Si alloys over their *bcc*/*hcp* phase transition pressure at room temperature will be interesting. Before these data are considered final, the $Fe_{91}Si_{09}$ results will be better calibrated and the volumetric contribution of low and high pressure phases will be made.

Table 4.1 Magnetic Data for iron rich Fe-Ni and Fe-Si alloys. P, average pressure; SIRM, saturation isothermal remanent magnetization; Bcr, coercivity of remanence Scorr, correction made to the SIRM data to account for the change in demagnetizing factor due to the increasing degree of oblateness. SIRMnorm is the SIRM normalized by the initial value after accounting for S_{corr}, e.g., $(SIRM_{p=n}/S_{corr})/(SIRM_{p=i}/S_{corr})$. h/d, height to average diameter ratio of sample chamber.

P (GPa)	SIRM ($\times 10^{9}$Am^{2})	Bcr (mT)	S_{corr} ($\times 10^{-3}$)	$SIRM_{norm}$	h/d
			$Fe_{92}Ni_{08}$		
0.4	11.1	20.2	0.89	1.0	0.9
5.4	12.9	21.5	0.98	1.1	0.8
8.0	19.6	22.3	1.12	1.4	0.6
10.1	30.4	17.8	1.30	1.9	0.5
13.5	81.6	23.0	1.53	4.3	0.4
17.0	99.9	26.8	1.77	4.5	0.3
19.8	73.9	27.2	1.92	3.1	0.3
23.0	41.4	30.5	2.08	1.6	0.3
20.6	42.9	29.7	2.08	1.7	0.3
17.0	46.4	29.3	2.09	1.8	0.3
12.3	75.3	26.9	2.08	2.9	0.3
9.5	117.4	25.1	2.08	4.5	0.3
6.5	82.7	17.9	2.08	3.2	0.3
3.9	46.0	12.8	2.08	1.8	0.3
0.0	45.6	14.2	2.08	1.8	0.3
			$Fe_{84}Ni_{16}$		
0.2	10.8	22.8	0.85	1.0	1.0
4.7	13.0	27.3	0.91	1.1	0.9
7.5	16.1	24.6	1.13	1.1	0.6
11.7	53.4	25.7	1.42	3.0	0.5
14.8	67.7	35.1	1.68	3.2	0.3
18.5	23.7	33.1	2.11	0.9	0.2
20.4	18.4	23.6	2.02	0.7	0.3
24.1	14.6	23.6	2.00	0.6	0.3
21.1	20.4	24.0	2.01	0.8	0.3
18.1	23.0	22.5	2.14	0.8	0.2
14.9	29.6	29.4	2.03	1.1	0.3
10.8	65.5	33.2	2.08	2.5	0.3
7.8	112.9	30.1	2.02	4.4	0.3
5.8	103.6	28.4	2.05	4.0	0.3
3.7	59.9	17.9	2.05	2.3	0.3
0.0	44.5	15.9	2.05	1.7	0.3

To be continued

Continuing

P (GPa)	SIRM ($\times 10^9$Am^2)	Bcr (mT)	S_{corr} ($\times 10^{-3}$)	SIRM$_{norm}$	h/d
			$Fe_{87}Ni_{13}$		
0.2	8.4	27.5	0.89	1.0	0.9
3.9	11.9	27.4	0.94	1.3	0.8
7.7	18.0	17.5	1.32	1.4	0.5
11.7	50.5	17.4	1.80	3.0	0.3
15.4	67.6	27.1	2.11	3.4	0.2
19.4	48.0	27.9	2.13	2.4	0.2
14.6	49.4	30.9	2.13	2.5	0.2
11.1	58.6	28.4	2.13	2.9	0.2
8.6	75.3	24.8	2.13	3.7	0.2
4.7	79.2	18.9	2.13	3.9	0.2
0.0	59.3	12.9	2.13	3.0	0.2
			$Fe_{91}Si_{09}$		
0.2	1.9	45.7	0.84	1.0	1.0
7.9	7.1	21.3	1.25	2.5	0.5
10.5	8.3	19.4	1.24	3.0	0.6
12.4	9.8	15.1	1.49	2.9	0.4
16.4	14.5	12.3	1.81	3.6	0.3
21.9	25.6	13.0	2.06	5.5	0.3
17.3	25.3	12.0	2.06	5.4	0.3
11.7	28.8	13.5	2.06	6.2	0.3
4.9	27.1	11.4	2.06	5.8	0.3
0.0	19.7	10.4	2.06	4.3	0.3
			$Fe_{83}Si_{17}$		
0.3	8.3	14.7	0.96	1.0	0.8
5.1	16.1	13.2	1.48	1.3	0.4
8.7	20.0	10.6	2.04	1.1	0.3
13.1	25.7	9.2	2.20	1.3	0.2
19.3	35.2	8.7	2.23	1.8	0.2
15.2	32.4	8.6	2.27	1.6	0.2
12.8	33.6	8.6	2.27	1.7	0.2
5.5	36.4	8.6	2.27	1.9	0.2
0.0	32.3	8.9	2.27	1.6	0.2

5. Curie temperature study of TM60 and $Fe_{64}Ni_{36}$ Invar by laser heating

The Curie temperatures of TM60 (titanomagnetite- $Fe_{2.4}Ti_{0.6}O_4$) and $Fe_{64}Ni_{36}$ invar under pressure were studied with a laser heating technique. Our preliminary experimental data shows that Curie temperature of TM60 increases with pressure, which is consistent with former studies; Curie temperature of $Fe_{64}Ni_{36}$ also increases with pressure, which is inconsistent with former studies.

5.1 Introduction

Magnetization intensity, magnetic coercivity, and Curie temperature are three critical parameters for describing properties of magnetic materials. Through the former chapter we learned that pressure enhances remanent magnetization by many fold with only relatively modest changes in coercivity of remanence for Fe-Ni and Fe-Si alloys. We now question how the Curie temperature behaves under pressure. Curie temperature with pressure goes from sharply negative at the low Ni invar compositions (−35 K/GPa for $Fe_{64}Ni_{36}$) to negative yet with lower slopes as Ni increases (−29 and −21 K/GPa for $Fe_{58}Ni_{42}$ and $Fe_{50}Ni_{50}$); the slope becomes positive for *fcc* compositions above ~65% Ni and is 4 K/GPa for Ni_{100} (Hausch, 1973; Kouvel and Wilson, 1961; Leger et al., 1972a; Patrick, 1954). The Curie temperature of magnetite and titanomagnetite increase with pressure (Schult, 1970), by about 12.5 K/GPa.

The technique previously used to measure Curie temperature was that two coils were put around the samples under pressure, a frequency signal input from one coil, the voltage signal detected on the second coil is proportional to the magnetic susceptibility. Here we study the Curie temperature of $Fe_{64}Ni_{36}$ (Invar) and TM60 (titanomagnetite, $Fe_{2.4}Ti_{0.6}O_4$), by laser heating method at high pressure in a non-magnetic moissanite anvil cell. Fast laser heating can avoid the thermal expansion influence from the moissanite anvil cell, which looses pressure with temperature increase by normal heating, such as using resistant wires. Preliminary results are shown and discussed.

5.2 Experimental Procedure and Results

Our experiments used polycrystalline samples of $Fe_{64}Ni_{36}$ (*Goodfellow,* purity >99.5%, max particle size 45 µm) and few pieces of single crystal TM60. Magnetic hysteresis loops measured on all samples with a Petersen Instruments, variable field translation balance at ambient conditions yield remanence ratios (remanent magnetization after saturation (Mrs) / saturation magnetization (Ms)) <0.1 and coercivity ratios (coercivity of remanence (Bcr) / bulk coercivity (Bc)) >7, characteristic of multidomain material. Curie temperatures were measured with a Petersen Instruments, variable field translation balance in a 30 mT field, and defined by the second derivative of the data, are 208°C and 153°C for $Fe_{64}Ni_{36}$ and TM60, respectively.

In each experiment, samples were loaded together with ruby spheres and silica gel into a cylindrical chamber drilled in a rhenium or work hardened beryllium copper gasket that was contained within a pressure cell consisting of Be-Cu metal and moissanite anvils. The culet diameter of moissanite anvils is about ~400 µm. Gaskets of initial thickness 250 µm were pre-compressed to thicknesses of 150-180 µm; then a hole of diameter 150-200 µm was drilled in the center to be used as a sample chamber. Pressure was measured at room temperature using ruby fluorescence spectroscopy with a Coherent, Cube 405 nm laser and a Princeton Instruments (PIXIS) charged coupled device connected to a 150 mm, ARC SpectraPro spectrometer. Rubies placed near the center and edge of the sample chamber helped monitor potential pressure gradients. Discussion below reports the average, not peak, pressures.

A JK50FL fiber laser (maximum output power 50 W) is connected with a microscopic focusing laser process head (Figure 1.7) for heating. The focused laser beam (diameter is <35 µm) is powerful enough to burn steel in air, even using minimum fiber laser power (1%, ~2W- minimum output). Power across the laser beam is Gaussian profile, and can be lowered by defocusing. So in our experiments the power density of laser spot is controlled by the laser output power and distance that the sample lies away from the focusing point. The lens for laser focus is 20.0 mm in diameter at a focal distance of 76.0 mm. The laser spot seen by the sample will be 263 µm in diameter (larger than the diameter of the sample chamber, 150-200 µm) if the sample is put 1 mm away from the focusing point of the laser. The off focusing distance is precisely controlled by a XYZ stage (resolution 0.01 mm), and focusing status can be monitored by the camera integrated on the laser head. The average power density of the entire laser spot is calculated simply by the output power of the laser divided by the laser spot area (Figure 5.1).

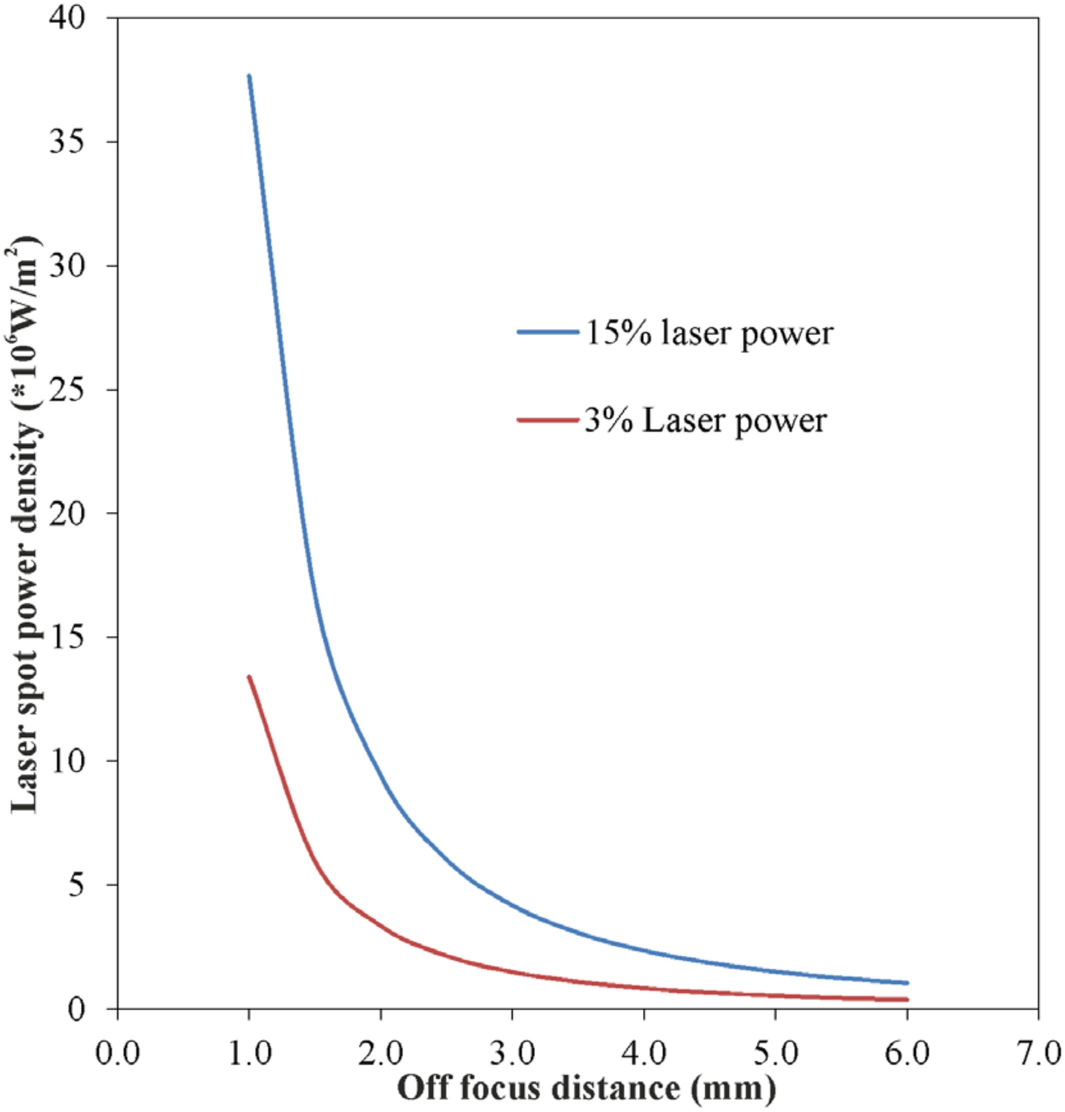

Figure 5.1 Power density of the defocused laser beam. The power density is calculated that output power of laser (Power output= 0.439* (laser power percentage) + 1.5967, in unit Watt) divides the laser spot area (= 0.2173*Off focus distance^2, in unit 10^{-6} m^2).

For each experiment at successive pressure steps, we measured the stepwise saturation magnetization. A static field was directed perpendicular to the axis of the moissanite pistons with an electromagnet whose pole pieces slide through the cell's housing until they abut the pistons. In the first step, we applied a magnetic field of 370 mT along the y axis direction; at such field sample is magnetically saturated (Figure 3.3a&b). The cell was removed from the electromagnet and then placed into the bore of a 2G Enterprises Inc., three-axis, superconducting quantum interference device (SQUID) magnetometer to measure the full magnetic vector. This data is the saturation remanent magnetization at room temperature. In a second step, both sides of the sample were heated by laser at a specified power (Figure 1.7) through the moissanite anvil window, then the remanent magnetization was measured again with the SQUID magnetometer. The laser heating were applied in Earth magnetic field. The second data point is the demagnetized remanent magnetization, corresponding to the laser power. We repeat the first and second step for laser heating with different laser power densities (0.4-37.7 $*10^6$ W/m^2). Once completed, the pressure is raised or lowered and then the whole process is repeated. Remanent magnetization versus laser heating power curves at different pressures were measured (Figure 5.3). The experiment for $Fe_{64}Ni_{36}$ used pressure steps of 0.2 GPa, 5.5 GPa, 9.4 GPa, 6.8 GPa, 5.2 GPa and 0.0 GPa; and the experiment for TM60 used pressure steps of 0.6 GPa, 7.2 GPa, and 0.0 GPa. The experiment data is listed in Table 5.1.

SIRM of $Fe_{64}Ni_{36}$ and TM60 before each laser heating is constant at a given pressure (Figure 5.2a&b; Table 5.1). For both TM60 and $Fe_{64}Ni_{36}$, the SIRM is enhanced by pressure at room temperature (Figure 5.2c), which is consistent with the former studies (Gilder and Le Goff, 2008; Wei et al., 2014). When laser heated for 10 seconds, with a laser output power of 8.2 W (Watt) at 1 mm from the focusing point (average power density of the laser spot for such set is 37.7 $*10^6$ W/m^2), the remnant magnetization ratio after laser heating M_{rh}/ SIRM decreases with the average power density of the laser spot (Figure 5.3). M_{rh}/SIRM decreases from ~1 to 0.3-0.7 for TM60 and from ~1 to 0.6-0.8 for $Fe_{64}Ni_{36}$.

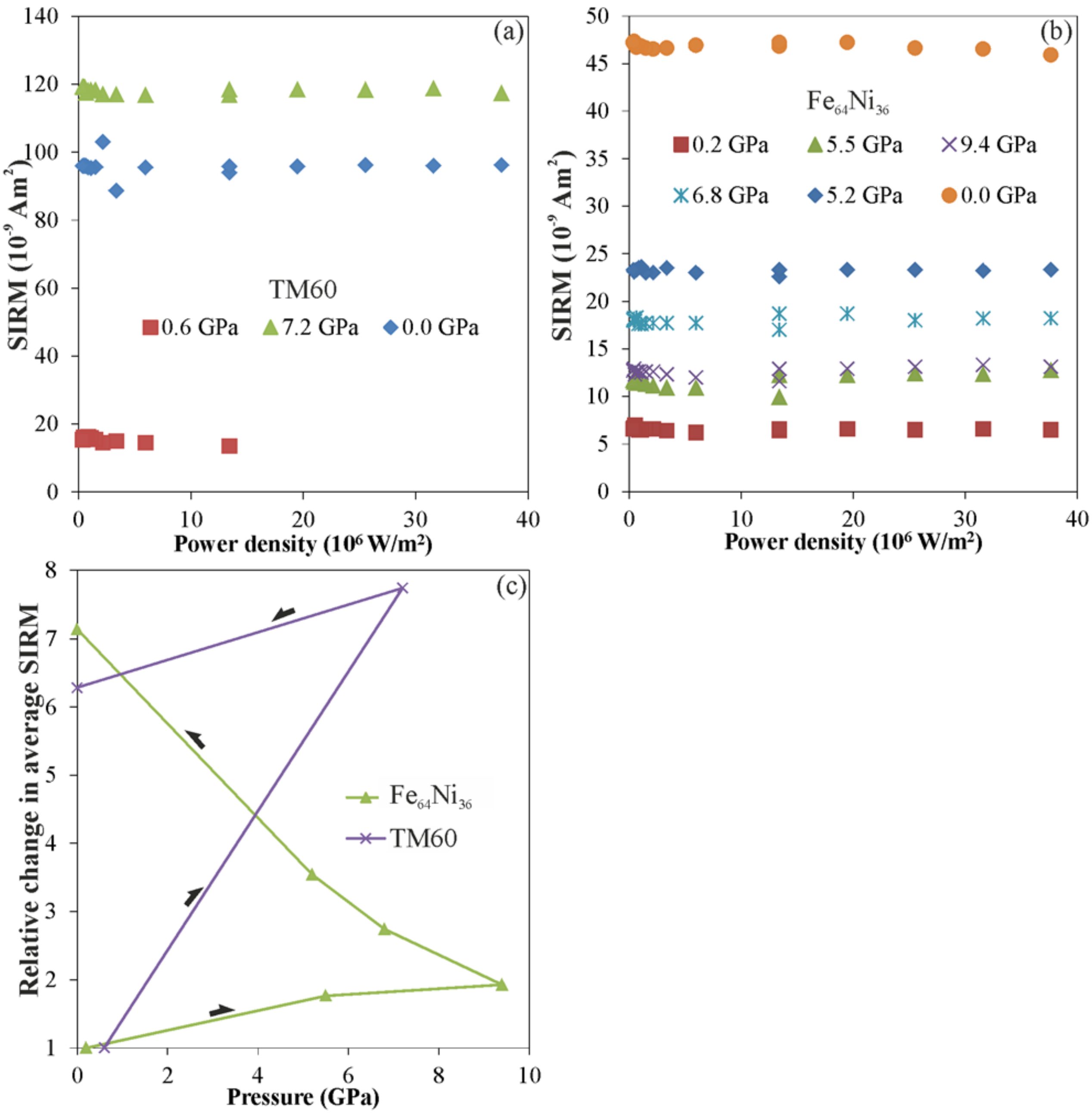

Figure 5.2 SIRM of $Fe_{64}Ni_{36}$ and TM60 under pressure. (**a-b**) Saturation isothermal remanent magnetization (SIRM) of TM60 and $Fe_{64}Ni_{36}$ corresponding to the average power density of the laser spot before each laser heating. (**c**) Average SIRM of $Fe_{64}Ni_{36}$ of TM60 and $Fe_{64}Ni_{36}$ as function of pressure. Data is listed in Table 5.1. Arrows indicate the pressure path.

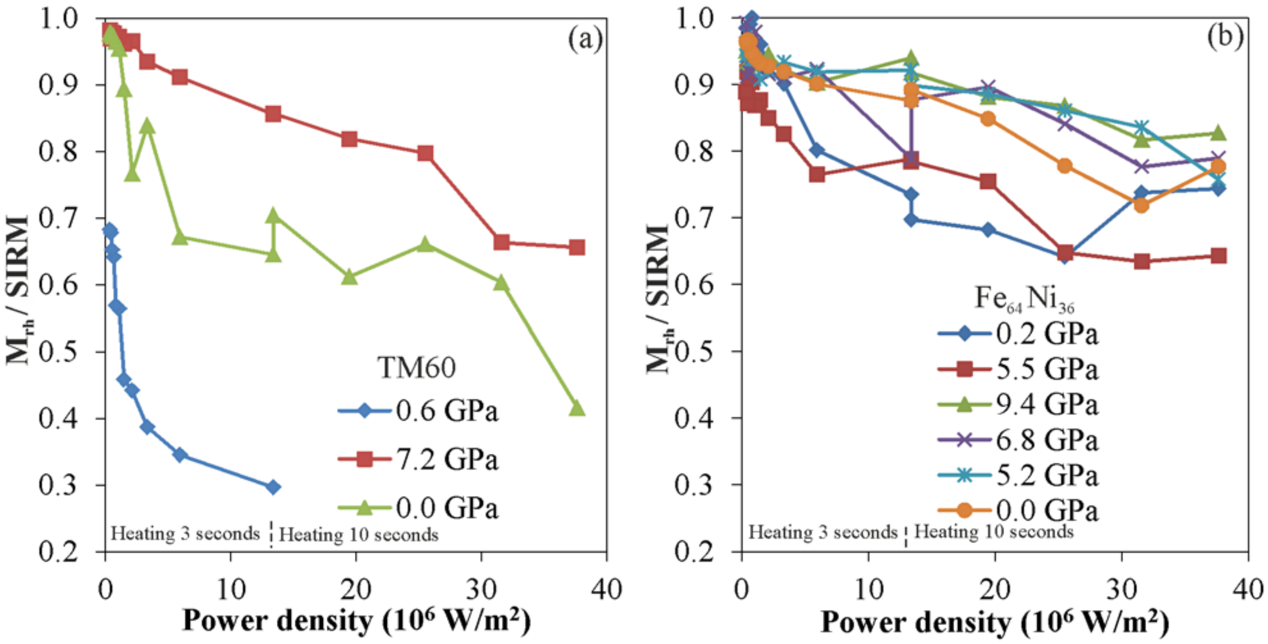

Figure 5.3 Magnetic data of TM60 and $Fe_{64}Ni_{36}$ after laser heating. **(a)** M_{rh} (remnant magnetization after laser heating) / SIRM (isothermal saturation remnant magnetization) versus power density of the laser beam for TM60 under pressure; **(b)** M_{rh} (remnant magnetization after laser heating) / SIRM (saturation isothermal remnant magnetization) versus power density of the laser beam for $Fe_{64}Ni_{36}$ invar under pressures. Heating time last of 3 and 10 seconds for power density of 0.4 -13.4 $*10^6$ W/m^2 and 13.4-37.7 $*10^6$ W/m^2 respectively.

5.3 Discussion

Remnant magnetization of ferromagnetic material decreases with temperature at ambient pressure; as well, the remnant magnetization decreases more rapidly approaching the Curie temperature. The laser passes through the moissanite anvil and the light energy is absorbed on the sample’s surface producing heat. Higher laser power and longer heating times induce higher temperatures. Mrh/SIRM of TM60 and $Fe_{64}Ni_{36}$ decrease with increasing power density, which corresponds to thermal demagnetization of the sample. Considering a Gaussian profile of power across the laser spot, the hottest place is in the spot’s center. Mrh/SIRM of TM60 at 0.6 GPa decreases greatly around laser power density 3.4$*10^6$ W/m^2, suggesting that the temperature corresponds to around 150 °C (20% magnetization remaining in Figure 5.4a). Except for TM60 at 0.6 GPa, Mrh/SIRM ratio (Figure 5.3) for TM60 and $Fe_{64}Ni_{36}$ is still high (>0.4) after laser heating with laser power density 37.7$*10^6$ W/m^2; it could indicate that only part of the sample was heated above the Curie temperature. A reason for this is that most of the energy from laser heating was transferred to the anvil and body of the cell, because thermal conductivity of moissanite anvil is much higher (200-500 W/m K) than the sample (~10 W/m K). Supposedly part of the sample is heated over its Curie temperature during laser heating, and the higher the laser powder density, the larger the fraction of the sample was heated. At constant pressure, SIRM for each sample is relatively constant before and after laser heating, which suggests no alteration (oxidization) occurred during heating.

Heating time lasted 3 and 10 seconds for power densities between 0.4-13.4 $*10^6$ W/m^2 and 13.4-37.7 $*10^6$ W/m^2 respectively. Different heating time caused slight discontinuity on M_{rh}/SIRM versus power density curves (Figure 5.3) at power density 13.4 $*10^6$ W/m^2. The trends of curves for power density between 0.4-13.4 $*10^6$ W/m^2 and 13.4-37.7 $*10^6$ W/m^2 are relatively consistent when the power density is near 13.4 $*10^6$ W/m^2. No absolute values of Curie temperature were measured, only relative (higher or lower) changes when compared to the Curie temperature at ambient pressure. So in the following discussion, we only talk about the relationship of relative remnant magnetization with power density, which is then related to Curie temperature.

Figure 5.3a shows the demagnetization spectra of TM60 at 7.2 GPa compared against that for 0.6 GPa (initial, near non-compressed). It means that using the same heating power, less demagnetization occurs at higher pressure. This implies that the Curie temperature of TM60 increases with pressure. It is consistent with a former study (Schult, 1970), which concluded that Curie temperature of TM60 increases by about 12.5 K/GPa. After pressure release from 7.2 to 0.0 GPa, the curve for pressure at 0.0 GPa is above the curve for pressure at 0.6 GPa for TM60 in Figure 5.3a. It means that Curie temperature of pressure-cycled TM60 is higher than non-compressed TM60. To verify that the Curie temperature of the pressure-cycled TM60, which was recovered at 0.0 GPa after the high pressure experiment, was measured in a Petersen Instruments, variable field translation balance Variable Field Translation Balance (VFTB) using a static magnetic field of 30 mT with heating and cooling rate 10 °C/minute. The signal in Figure 5.4a is averaged (50 neighbor values, temperature range 40°C) and normalized. Compared to non-compressed TM60, the Curie temperature curve (Figure 5.4a) was shift to higher temperature by about 10 °C at 50% magnetization moment for the heating up curves (Figure 5.4a). The increased Curie temperature value in our study (10 °C) is much lower than that of the former study, about 30 °C (Schult, 1970) in which TM60 was compressed up to ~5.5 GPa and released.

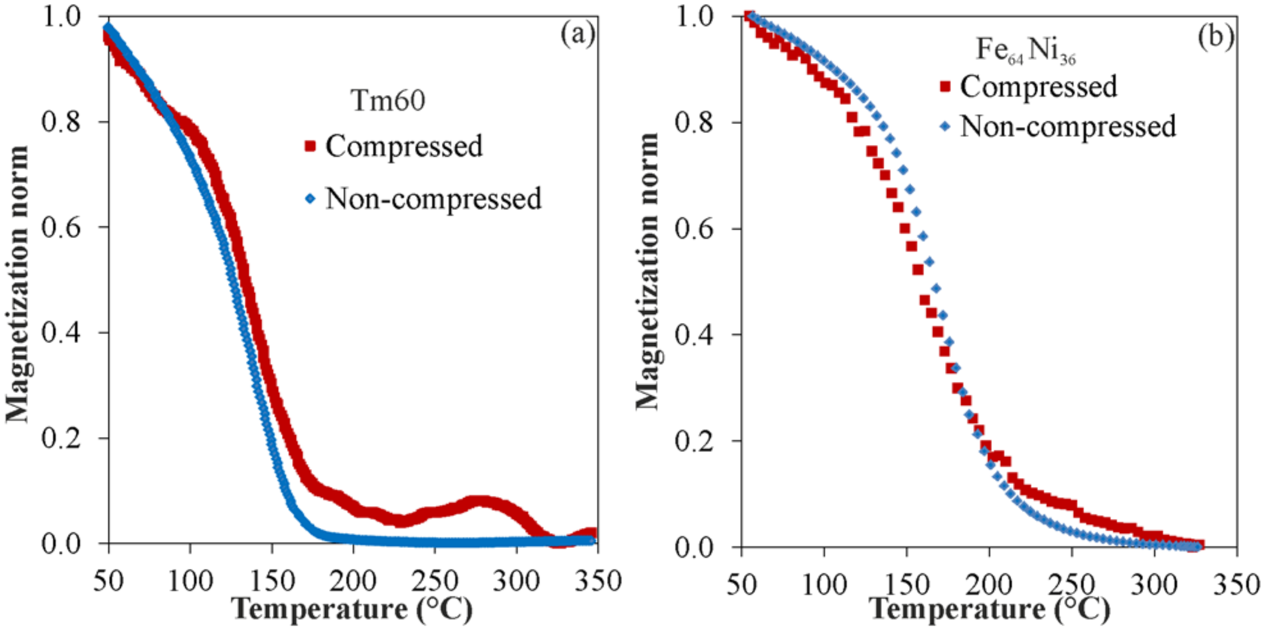

Figure 5.4 Curie temperature of TM60 and $Fe_{64}Ni_{36}$. **(a)** Curie temperature measurement for non-compressed and pressure-cycled TM60 (same sample in Figure 5.3a); **(b)** Curie temperature measurement for of non-compressed and pressure-cycled $Fe_{64}Ni_{36}$ (same sample in Figure 5.3b). The Curie temperature was measured in a Petersen Instruments, variable field translation balance (VFTB) under a static magnetic field of 30 mT with a heating rate of 10 °C/minute and 50 °C/minute for TM60 and $Fe_{64}Ni_{36}$ respectively. The raw data is noisy, but in all cases were averaged and normalized in same way.

For $Fe_{64}Ni_{36}$, most of the curves for pressure at 5.5 GPa below those at 0.2 GPa (initial, near non-compressed) in Figure 5.3b, except the part when the power density is near 13.4-25.5 $*10^6$ W/m^2. It indicates that the Curie temperature of $Fe_{64}Ni_{36}$ is slightly decreased at 5.5 GPa. Former susceptibility studies (Hausch, 1973; Kouvel and Wilson, 1961; Leger et al., 1972a; Patrick, 1954) on $Fe_{64}Ni_{36}$ concluded that the Curie temperature of $Fe_{64}Ni_{36}$ decreases, about -35 K/GPa, Curie temperature of $Fe_{64}Ni_{36}$ will be lower than room temperature and will lose their magnetization around 6 GPa. In our experiment, $Fe_{64}Ni_{36}$ is still ferromagnetic at 5.5 GPa (Figure 5.2, similar experiment results also showed in Figure 3.4a). There is 64% of the relative SIRM moment left at 5.5 GPa (Figure 5.3b) after laser heating for 10 seconds with laser beam power density of 37.7 $*10^6$ W/m^2. It may suggest that the Curie temperature of $Fe_{64}Ni_{36}$ is lowered very little at 5.5 GPa.

Curves for pressure at 9.4 GPa, 6.8 GPa, 5.2 GPa and 0.0 GPa are above those at 0.2 GPa (initial, near non-compressed) and 5.5 GPa for $Fe_{64}Ni_{36}$ in Figure 5.3b. Curves in Figure 5.3b shows that after the Curie temperature was slightly decreased at 5.5 GPa during compression, Curie temperature increased when further compressed to higher pressure (up to 9.4 GPa); the Curie temperature is relatively constant during decompression for pressures between 9.4-5.2 GPa, and decreases during decompression for pressures between 5.2-0.0 GPa. The Curie temperature at 0.0 GPa (after decompression) is higher than at 0.2 GPa (initial, near non-compressed). To verify that the Curie temperature of the pressure-cycled $Fe_{64}Ni_{36}$ sample, which was recovered at 0.0 GPa after the high pressure experiment, was measured in a Petersen Instruments, variable field translation balance Variable Field Translation Balance (VFTB) using a static magnetic field of 30 mT with heating rate of 50 °C/minute. The noise level for $Fe_{64}Ni_{36}$ is lower when using a heating rate of 50 °C/minute than 10 °C/minute. The signal in Figure 5.4b is averaged (50 neighbor values) and normalized. Seen at 50% decay in magnetization, the Curie temperature decreases for pressure-cycled $Fe_{64}Ni_{36}$, which is similar to that shown in Figure 3.5a in chapter 3 (Wei et al., 2014). However, the results in Figures 5.3b and 5.4b on pressure-cycled and non-compressed $Fe_{64}Ni_{36}$ are contradictory; the Curie temperature of $Fe_{64}Ni_{36}$ under pressure need to be further studied in the future.

5.4 Conclusions

Our experiments data shows preliminary result that Curie temperature of TM60 increases with pressure, which is consistent with former studies; The Curie temperature of $Fe_{64}Ni_{36}$ is inconsistent with former studies and needs to be further studied in the future.

Table 5.1 Magnetic data for TM60 and $Fe_{64}Ni_{36}$. SIRM, isothermal remanent magnetization after saturation; M_{rh}, remnant magnetization after laser heating from SIRM; Power, laser output; Power D, power density of off focused laser spot.

SIRM (10^{-9}Am^2)	Off focus (mm)	Power (W)	Time (s)	Power D (10^6 W/m^2)	M_{rh} (10^{-9}Am^2)	M_{rh}/SIRM
			$Fe_{64}Ni_{36}$ - 0.2 GPa			
6.4	1.0	2.9	3	13.4	4.7	0.7
6.2	1.5	2.9	3	6.0	5.0	0.8
6.4	2.0	2.9	3	3.4	5.8	0.9
6.6	2.5	2.9	3	2.1	6.1	0.9
6.6	3.0	2.9	3	1.5	6.3	1.0
6.5	3.5	2.9	3	1.1	6.2	1.0
6.5	4.0	2.9	3	0.8	6.5	1.0
6.6	4.5	2.9	3	0.7	6.5	1.0
7.0	5.0	2.9	3	0.5	6.8	1.0
6.7	5.5	2.9	3	0.4	6.5	1.0
6.6	6.0	2.9	3	0.4	6.5	1.0
6.6	1.0	2.9	10	13.4	4.6	0.7
6.6	1.0	4.2	10	19.5	4.5	0.7
6.5	1.0	5.5	10	25.5	4.2	0.6
6.6	1.0	6.9	10	31.6	4.9	0.7
6.5	1.0	8.2	10	37.7	4.8	0.7
			$Fe_{64}Ni_{36}$ - 5.5 GPa			
9.9	1.0	2.9	3	13.4	7.8	0.8
10.9	1.5	2.9	3	6.0	8.3	0.8
10.9	2.0	2.9	3	3.4	9.0	0.8
11.1	2.5	2.9	3	2.1	9.4	0.8
11.3	3.0	2.9	3	1.5	9.9	0.9
11.4	3.5	2.9	3	1.1	9.9	0.9
11.4	4.0	2.9	3	0.8	10.3	0.9
11.4	4.5	2.9	3	0.7	10.3	0.9
11.7	5.0	2.9	3	0.5	10.2	0.9
11.5	5.5	2.9	3	0.4	10.6	0.9
11.7	6.0	2.9	3	0.4	10.4	0.9
12.2	1.0	2.9	10	13.4	9.6	0.8
12.2	1.0	4.2	10	19.5	9.2	0.8
12.4	1.0	5.5	10	25.5	8.0	0.6
12.3	1.0	6.9	10	31.6	7.8	0.6
12.7	1.0	8.2	10	37.7	8.2	0.6

To be continued

Continuing

SIRM ($10^{-9}Am^2$)	Off focus (mm)	Power (W)	Time (s)	Power D ($10^6 W/m^2$)	M_{rh} ($10^{-9}Am^2$)	M_{rh}/SIRM
			$Fe_{64}Ni_{36}$ - 9.4 GPa			
11.6	1.0	2.9	3	13.4	10.9	0.9
12.0	1.5	2.9	3	6.0	10.8	0.9
12.3	2.0	2.9	3	3.4	11.3	0.9
12.6	2.5	2.9	3	2.1	11.9	0.9
12.6	3.0	2.9	3	1.5	11.7	0.9
12.5	3.5	2.9	3	1.1	11.8	0.9
12.6	4.0	2.9	3	0.8	11.9	0.9
12.6	4.5	2.9	3	0.7	12.0	1.0
12.3	5.0	2.9	3	0.5	11.8	1.0
12.9	5.5	2.9	3	0.4	12.0	0.9
12.7	6.0	2.9	3	0.4	12.1	1.0
12.9	1.0	2.9	10	13.4	11.8	0.9
12.9	1.0	4.2	10	19.5	11.4	0.9
13.1	1.0	5.5	10	25.5	11.4	0.9
13.3	1.0	6.9	10	31.6	10.9	0.8
13.1	1.0	8.2	10	37.7	10.8	0.8
			$Fe_{64}Ni_{36}$ - 6.8 GPa			
17.0	1.0	2.9	3	13.4	13.4	0.8
17.7	1.5	2.9	3	6.0	16.3	0.9
17.7	2.0	2.9	3	3.4	16.1	0.9
17.7	2.5	2.9	3	2.1	16.2	0.9
17.7	3.0	2.9	3	1.5	16.3	0.9
17.6	3.5	2.9	3	1.1	17.2	1.0
17.6	4.0	2.9	3	0.8	16.7	0.9
18.3	4.5	2.9	3	0.7	16.8	0.9
17.9	5.0	2.9	3	0.5	16.9	0.9
18.2	5.5	2.9	3	0.4	16.6	0.9
18.0	6.0	2.9	3	0.4	17.9	1.0
18.7	1.0	2.9	10	13.4	16.4	0.9
18.7	1.0	4.2	10	19.5	16.1	0.9
18.0	1.0	5.5	10	25.5	15.3	0.8
18.2	1.0	6.9	10	31.6	14.1	0.8
18.2	1.0	8.2	10	37.7	14.4	0.8

To be continued

Continuing

SIRM (10^{-9}Am^2)	Off focus (mm)	Power (W)	Time (s)	Power D (10^6 W/m^2)	M_{rh} (10^{-9}Am^2)	M_{rh}/SIRM
$Fe_{64}Ni_{36}$ - 5.2 GPa						
22.6	1.0	2.9	3	13.4	20.8	0.9
23.0	1.5	2.9	3	6.0	21.1	0.9
23.5	2.0	2.9	3	3.4	21.9	0.9
23.0	2.5	2.9	3	2.1	21.2	0.9
23.0	3.0	2.9	3	1.5	20.9	0.9
23.6	3.5	2.9	3	1.1	22.1	0.9
23.5	4.0	2.9	3	0.8	22.0	0.9
23.3	4.5	2.9	3	0.7	22.0	0.9
23.2	5.0	2.9	3	0.5	22.1	1.0
23.1	5.5	2.9	3	0.4	22.0	1.0
23.3	6.0	2.9	3	0.4	22.0	0.9
23.3	1.0	2.9	10	13.4	20.9	0.9
23.3	1.0	4.2	10	19.5	20.6	0.9
23.3	1.0	5.5	10	25.5	20.0	0.9
23.2	1.0	6.9	10	31.6	19.5	0.8
23.3	1.0	8.2	10	37.7	17.8	0.8
$Fe_{64}Ni_{36}$ - 0.0 GPa						
46.8	1.0	2.9	3	13.4	41.0	0.9
46.9	1.5	2.9	3	6.0	42.2	0.9
46.6	2.0	2.9	3	3.4	42.8	0.9
46.5	2.5	2.9	3	2.1	43.1	0.9
46.6	3.0	2.9	3	1.5	43.4	0.9
46.8	3.5	2.9	3	1.1	44.0	0.9
46.9	4.0	2.9	3	0.8	44.4	0.9
46.7	4.5	2.9	3	0.7	45.0	1.0
46.9	5.0	2.9	3	0.5	45.3	1.0
47.3	5.5	2.9	3	0.4	45.4	1.0
47.2	6.0	2.9	3	0.4	45.5	1.0
47.2	1.0	2.9	10	13.4	42.1	0.9
47.2	1.0	4.2	10	19.5	39.5	0.8
46.6	1.0	5.5	10	25.5	36.2	0.8
46.5	1.0	6.9	10	31.6	33.0	0.7
45.9	1.0	8.2	10	37.7	35.6	0.8

To be continued

Continuing

SIRM (10^{-9}Am^2)	Off focus (mm)	Power (W)	Time (s)	Power D (10^6 W/m^2)	M_{rh} (10^{-9}Am^2)	M_{rh}/SIRM
			TM60 - 0.6 GPa			
13.5	1.0	2.9	3	13.4	4.0	0.3
14.5	1.5	2.9	3	6.0	5.0	0.3
15	2.0	2.9	3	3.4	5.8	0.4
14.5	2.5	2.9	3	2.1	6.4	0.4
15.5	3.0	2.9	3	1.5	7.1	0.5
15.8	3.5	2.9	3	1.1	8.9	0.6
16.2	4.0	2.9	3	0.8	9.2	0.6
15.6	4.5	2.9	3	0.7	10.0	0.6
15.5	5.0	2.9	3	0.5	10.1	0.7
16.1	5.5	2.9	3	0.4	10.9	0.7
15.4	6.0	2.9	3	0.4	10.5	0.7
			TM60 - 7.2 GPa			
116.7	1.0	2.9	3	13.4	99.8	0.9
116.8	1.5	2.9	3	6.0	106.4	0.9
116.9	2.0	2.9	3	3.4	109.2	0.9
117	2.5	2.9	3	2.1	112.9	1.0
118.2	3.0	2.9	3	1.5	113.6	1.0
118.2	3.5	2.9	3	1.1	114.9	1.0
118	4.0	2.9	3	0.8	114.3	1.0
117.4	4.5	2.9	3	0.7	114.7	1.0
119.1	5.0	2.9	3	0.5	116.4	1.0
119.1	5.5	2.9	3	0.4	115.4	1.0
119.2	6.0	2.9	3	0.4	117.0	1.0
118.4	1.0	2.9	10	13.4	101.4	0.9
118.4	1.0	4.2	10	19.5	96.9	0.8
118.3	1.0	5.5	10	25.5	94.3	0.8
118.7	1.0	6.9	10	31.6	78.7	0.7
117.3	1.0	8.2	10	37.7	76.9	0.7

To be continued

Continuing

SIRM ($10^{-9}Am^2$)	Off focus (mm)	Power (W)	Time (s)	Power D (10^6 W/m^2)	M_{rh} ($10^{-9}Am^2$)	M_{rh}/SIRM
			TM60 - 0 GPa			
94.0	1.0	2.9	3	13.4	60.6	0.6
95.5	1.5	2.9	3	6.0	64.1	0.7
88.7	2.0	2.9	3	3.4	74.4	0.8
103.0	2.5	2.9	3	2.1	78.9	0.8
95.6	3.0	2.9	3	1.5	85.4	0.9
95.3	3.5	2.9	3	1.1	90.9	1.0
95.5	4.0	2.9	3	0.8	92.1	1.0
95.9	4.5	2.9	3	0.7	93.2	1.0
96.0	5.0	2.9	3	0.5	93.5	1.0
95.9	5.5	2.9	3	0.4	93.7	1.0
96.0	6.0	2.9	3	0.4	93.8	1.0
95.8	1.0	2.9	10	13.4	67.4	0.7
95.8	1.0	4.2	10	19.5	58.6	0.6
96.2	1.0	5.5	10	25.5	63.5	0.7
96.0	1.0	6.9	10	31.6	57.9	0.6
96.2	1.0	8.2	10	37.7	40.0	0.4

References:

Abd-Elmeguid, M.M., Schleede, B., Micklitz, H., 1988. Pressure-induced antiferromagnetism in fcc Fe-Ni Invar alloys. Journal of Magnetism and Magnetic Materials 72, 253-257. doi:10.1016/0304-8853(88)90219-3.

Albertsen, J.F., Nielsen, H.P., Buchwald, V.F., 1983. On the Fine Structure of Meteoritical Taenite/Tetrataenite and its Interpretation. Physica Scripta 27, 314-320. doi:10.1088/0031-8949/27/4/015.

Alfè, D., Gillan, M.J., Price, G.D., 2007. Temperature and composition of the Earth's core. Contemporary Physics 48, 63-80. doi:10.1080/00107510701529653.

Allègre, C.J., Poirier, J.-P., Humler, E., Hofmann, A.W., 1995. The chemical composition of the Earth. Earth and Planetary Science Letters 134, 515-526. doi:10.1016/0012-821x(95)00123-t.

Anderson, D.L., 1989. Composition of the Earth. Science 243, 367-370. doi:10.1126/science.243.4889.367.

Anderson, O.L., Isaak, D.G., 2002. Another look at the core density deficit of Earth’s outer core. Physics of the Earth and Planetary Interiors 131, 19-27. doi:10.1016/s0031-9201(02)00017-1.

Andrault, D., 1997. The Orthorhombic Structure of Iron: An in Situ Study at High-Temperature and High-Pressure. Science 278, 831-834. doi:10.1126/science.278.5339.831.

Anzellini, S., Dewaele, A., Mezouar, M., Loubeyre, P., Morard, G., 2013. Melting of iron at Earth's inner core boundary based on fast X-ray diffraction. Science 340, 464-466. doi:10.1126/science.1233514.

Asano, H., 1969. Magnetism of γ Fe-Ni Invar Alloys with Low Nickel Concentration. Journal of the Physical Society of Japan 27, 542-553. doi:10.1143/jpsj.27.542.

Badro, J., Fiquet, G., Guyot, F., 2006. Effect of light elements on the sound velocities in solid iron: Implications for the composition of earth’s core. Geochimica et Cosmochimica Acta 70, A28. doi:10.1016/j.gca.2006.06.165.

Bassett, W.A., Huang, E., 1987. Mechanism of the body-centered cubic--hexagonal close-packed phase transition in iron. Science 238, 780-783. doi:10.1126/science.238.4828.780.

Baudelet, F., Pascarelli, S., Mathon, O., Itié, J.P., Polian, A., Astuto, M.d., Chervin, J.C., 2005. X-ray absorption spectroscopy and x-ray magnetic circular dichroism simultaneous measurements under high pressure: the iron bcc-hcp transition case. J. Phys.: Condens Matter 17, S957-S966. doi:10.1088/0953-8984/17/11/028.

Bezaeva, N.S., Gattacceca, J., Rochette, P., Sadykov, R.A., Trukhin, V.I., 2010. Demagnetization of terrestrial and extraterrestrial rocks under hydrostatic pressure up to 1.2GPa. Physics of the Earth and Planetary Interiors 179, 7-20. doi:10.1016/j.pepi.2010.01.004.

Birch, F., 1952. Elasticity and constitution of the Earth's interior. Journal of Geophysical Research 57, 227-286. doi:10.1029/JZ057i002p00227.

Birch, F., 1964. Density and composition of mantle and core. Journal of Geophysical Research 69, 4377-4388. doi:10.1029/JZ069i020p04377.

Boehler, R., 1993. Temperatures in the Earth's core from melting-point measurements of iron at high static pressures. Nature 363, 534-536. doi:10.1038/363534a0.

Bottke, W.F., Nesvorny, D., Grimm, R.E., Morbidelli, A., O'Brien, D.P., 2006. Iron meteorites as remnants of planetesimals formed in the terrestrial planet region. Nature 439, 821-824. doi:10.1038/nature04536.

Bozorth, R., Walker, J., 1953. Magnetic Crystal Anisotropy and Magnetostriction of Iron-Nickel Alloys. Physical Review 89, 624-628. doi:10.1103/PhysRev.89.624.

Brown, J.M., McQueen, R.G., 1986. Phase transitions, Grüneisen parameter, and elasticity for shocked iron between 77 GPa and 400 GPa. Journal of Geophysical Research 91, 7485. doi:10.1029/JB091iB07p07485.

Bullen, K.E., 1952. Cores of Terrestrial Planets. Nature 170, 363-364. doi:10.1038/170363a0.

Bullen, K.E., 1973. Cores of the Terrestrial Planets. Nature 243, 68-70. doi:10.1038/243068a0.

Chabot, N.L., Wollack, E.A., Klima, R.L., Minitti, M.E., 2014. Experimental constraints on Mercury's core composition. Earth and Planetary Science Letters 390, 199-208. doi:10.1016/j.epsl.2014.01.004.

Chervin, J.C., Canny, B., Mancinelli, M., 2001. Ruby-spheres as pressure gauge for optically transparent high pressure cells. High Pressure Research 21, 305-314. doi:10.1080/08957950108202589.

Chuang, Y.-Y., Chang, Y.A., Schmid, R., Lin, J.-C., 1986. Magnetic contributions to the thermodynamic functions of alloys and the phase equilibria of Fe-Ni system below 1200 K. Metallurgical Transactions A 17, 1361-1372. doi:10.1007/bf02650117.

Cisowski, S., 1981. Interacting vs. non-interacting single domain behavior in natural and synthetic samples. Physics of the Earth and Planetary Interiors 26, 56-62. doi:10.1016/0031-9201(81)90097-2.

Collinson, D.W., 1983. Methods in Rock Magnetism and Palaeomagnetism Techniques and Instrumentation. Chapman and Hall, New York.

Cort, G., Taylor, R.D., Willis, J.O., 1982. Search for magnetism in hcp ε-Fe. Journal of Applied Physics 53, 2064. doi:10.1063/1.330745.

Crangle, J., Hallam, G.C., 1963. The Magnetization of Face-Centred Cubic and Body-Centred Cubic Iron + Nickel Alloys. Proceedings of the Royal Society A: Mathematical, Physical and Engineering Sciences 272, 119-132. doi:10.1098/rspa.1963.0045.

Dubovka, G.T., 1974. On the concentration dependence of the Curie points of Fe-Ni alloys. Physica Status Solidi (a) 24, 375-379. doi:10.1002/pssa.2210240135.

Dubrovinsky, L., Dubrovinskaia, N., Narygina, O., Kantor, I., Kuznetzov, A., Prakapenka, V.B., Vitos, L., Johansson, B., Mikhaylushkin, A.S., Simak, S.I., Abrikosov, I.A., 2007. Body-centered cubic iron-nickel alloy in Earth's core. Science 316, 1880-1883. doi:10.1126/science.1142105.

Dubrovinsky, L., Saxena, S., Tutti, F., Rekhi, S., LeBehan, T., 2000a. In Situ X-Ray Study of Thermal Expansion and Phase Transition of Iron at Multimegabar Pressure. Physical Review Letters 84, 1720-1723. doi:10.1103/PhysRevLett.84.1720.

Dubrovinsky, L.S., Saxena, S.K., Tutti, F., Rekhi, S., Lebehan, T., 2000b. In situ X-ray study of thermal expansion and phase transition of iron at multimegabar pressure. Phys.Rev.Lett. 84, 1720-1723. doi:10.1103/PhysRevLett.84.1720.

Dunlop, D.J., Özdemir, Ö., 1977. Rock Magnetism: Fundamentals and Frontiers. Cambridge University Press, Cambridge, New York, Port Chester, Melbourne, Sydney.

Dunlop, D.J., Özdemir, Ö., 1997. Rock Magnetism: Fundamentals And Frontiers. Cambridge University Press, Cambridge. doi:10.1017/CBO9780511612794.

Fischer, R.A., Campbell, A.J., Caracas, R., Reaman, D.M., Dera, P., Prakapenka, V.B., 2012. Equation of state and phase diagram of Fe–16Si alloy as a candidate component of Earth's core. Earth and Planetary Science Letters 357-358, 268-276. doi:10.1016/j.epsl.2012.09.022.

Fischer, R.A., Campbell, A.J., Reaman, D.M., Miller, N.A., Heinz, D.L., Dera, P., Prakapenka, V.B., 2013. Phase relations in the Fe–FeSi system at high pressures and temperatures. Earth and Planetary Science Letters 373, 54-64. doi:10.1016/j.epsl.2013.04.035.

Georg, R.B., Halliday, A.N., Schauble, E.A., Reynolds, B.C., 2007. Silicon in the Earth's core. Nature 447, 1102-1106. doi:10.1038/nature05927.

Gilder, S., Glen, J., 1998. Magnetic properties of hexagonal closed-packed iron deduced from direct observations in a diamond anvil cell. Science 279, 72-74.

Gilder, S., Le Goff, M., 2008. Systematic pressure enhancement of titanomagnetite magnetization. Geophys. Res. Lett. 35. doi:10.1029/2008GL033325.

Gilder, S.A., Egli, R., Hochleitner, R., Roud, S.C., Volk, M.W.R., Le Goff, M., de Wit, M., 2011. Anatomy of a pressure-induced, ferromagnetic-to-paramagnetic transition in pyrrhotite: Implications for the formation pressure of diamonds. Journal of Geophysical Research 116. doi:10.1029/2011JB008292.

Gilder, S.A., Le Goff, M., 2005. Pressure dependence on the magnetic properties of titanomagnetite using the reversible susceptibility method. Elsevier, in Advances in High-Pressure Technology for Geophysical Applications, edited by J.H. Chen, Y.B. Wang, T.S. Duffy, G.Y. Shen and L. Dobrzhinetskaya,. doi:10.1016/B978-044451979-5.50017-X.

Glaubitz, B., Buschhorn, S., Brüssing, F., Abrudan, R., Zabel, H., 2011. Development of magnetic moments in $Fe_{1-x}Ni_x$-alloys. Journal of Physics: Condensed Matter 23, 254210. doi:10.1088/0953-8984/23/25/254210.

Goldstein, J.I., Scott, E.R.D., Chabot, N.L., 2009. Iron meteorites: Crystallization, thermal history, parent bodies, and origin. Chemie der Erde - Geochemistry 69, 293-325. doi:10.1016/j.chemer.2009.01.002.

Gorria, P., Martínez-Blanco, D., Pérez, M., Blanco, J., Hernando, A., Laguna-Marco, M., Haskel, D., Souza-Neto, N., Smith, R., Marshall, W., Garbarino, G., Mezouar, M., Fernández-Martínez, A., Chaboy, J., Fernandez Barquín, L., Rodriguez Castrillón, J., Moldovan, M., García Alonso, J., Zhang, J., Llobet, A., Jiang, J., 2009. Stress-induced large Curie temperature enhancement in Fe64Ni36 Invar alloy. Physical Review B 80, 064421. doi:10.1103/PhysRevB.80.064421.

Hausch, G., 1973. Magnetovolume effects in invar alloys: Spontaneous and forced volume magnetostriction. Physica Status Solidi (a) 18, 735-740. doi:10.1002/pssa.2210180236.

Hirao, N., Ohtani, E., Kondo, T., Kikegawa, T., 2004. Equation of state of iron?silicon alloys to megabar pressure. Physics and Chemistry of Minerals 31. doi:10.1007/s00269-004-0387-x.

Huang, E., Bassett, W.A., Weathers, M.S., 1988. Phase relationships in Fe-Ni alloys at high pressures and temperatures. Journal of Geophysical Research 93, 7741. doi:10.1029/JB093iB07p07741.

Iota, V., Klepeis, J.-H.P., Yoo, C.-S., Lang, J., Haskel, D., Srajer, G., 2007. Electronic structure and magnetism in compressed 3d transition metals. Applied Physics Letters 90, 042505. doi:10.1063/1.2434184.

Jackson, J.M., Sturhahn, W., Lerche, M., Zhao, J., Toellner, T.S., Alp, E.E., Sinogeikin, S.V., Bass, J.D., Murphy, C.A., Wicks, J.K., 2013. Melting of compressed iron by monitoring atomic dynamics. Earth and Planetary Science Letters 362, 143-150. doi:10.1016/j.epsl.2012.11.048.

Javoy, M., 1995. The integral enstatite chondrite model of the Earth. Geophysical Research Letters 22, 2219-2222. doi:10.1029/95gl02015.

Jeanloz, R., 1979. Properties of iron at high pressures and the state of the core. Journal of Geophysical Research 84, 6059. doi:10.1029/JB084iB11p06059.

Kittel, C., 1949. Physical Theory of Ferromagnetic Domains. Reviews of Modern Physics 21, 541-583. doi:10.1103/RevModPhys.21.541.

Klotz, S., Chervin, J.C., Munsch, P., Le Marchand, G., 2009. Hydrostatic limits of 11 pressure transmitting media. Journal of Physics D: Applied Physics 42, 075413. doi:10.1088/0022-3727/42/7/075413.

Kouvel, J.S., Wilson, R.H., 1961. Magnetization of Iron - Nickel Alloys Under Hydrostatic Pressure Journal of Applied Physics 32, 435-441. doi:10.1063/1.1736020.

Kuwayama, Y., Hirose, K., Sata, N., Ohishi, Y., 2008. Phase relations of iron and iron–nickel alloys up to 300 GPa: Implications for composition and structure of the Earth's inner core. Earth and Planetary Science Letters 273, 379-385. doi:10.1016/j.epsl.2008.07.001.

Kuwayama, Y., Sawai, T., Hirose, K., Sata, N., Ohishi, Y., 2009. Phase relations of iron–silicon alloys at high pressure and high temperature. Physics and Chemistry of Minerals 36, 511-518. doi:10.1007/s00269-009-0296-0.

Leger, J., Loriers-Susse, C., Vodar, B., 1972a. Pressure Effect on the Curie Temperatures of Transition Metals and Alloys. Physical Review B 6, 4250-4261. doi:10.1103/PhysRevB.6.4250.

Leger, J.M., Loriers-Susse, C., Vodar, B., 1972b. Pressure effect on the Curie temperatures of transition metals and alloys. Phys.Rev.B 6, 4250-4261.

Li, J., Fei, Y., 2007. Experimental Constraints on Core Composition. 1-31. doi:10.1016/b0-08-043751-6/02014-4.

Li, Q., Wiedenmann, A., Wollenberger, H., 1997. Fractal morphologies from decomposition of Fe−Ni−Invar alloys. Journal of Materials Research 12, 83-92. doi:http://dx.doi.org/10.1557/JMR.1997.0014.

Lin, J.-F., 2003. Static compression of iron-silicon alloys: Implications for silicon in the Earth's core. Journal of Geophysical Research 108. doi:10.1029/2002jb001978.

Lin, J.-F., Scott, H.P., Fischer, R.A., Chang, Y.-Y., Kantor, I., Prakapenka, V.B., 2009. Phase relations of Fe-Si alloy in Earth's core. Geophysical Research Letters 36. doi:10.1029/2008gl036990.

Lin, J., Heinz, D.L., Campbell, A.J., Devine, J.M., Mao, W.L., Shen, G., 2002. Iron-Nickel alloy in the Earth's core. Geophysical Research Letters 29, 109-101-109-103. doi:10.1029/2002gl015089.

Lin, J., Sturhahn, W., Zhao, J., Shen, G., Mao, H.K., Hemley, R.J., 2005. Sound velocities of hot dense iron: Birch's law revisited. Science 308, 1892-1894. doi:10.1126/science.1111724.

Liu, J., Lin, J.-F., Alatas, A., Bi, W., 2014. Sound velocities of bcc-Fe and Fe0.85Si0.15 alloy at high pressure and temperature. Physics of the Earth and Planetary Interiors 233, 24-32. doi:10.1016/j.pepi.2014.05.008.

Mao, H.K., Wu, Y., Chen, L.C., Shu, J.F., Jephcoat, A.P., 1990. Static compression of iron to 300 GPa and Fe0.8Ni0.2alloy to 260 GPa: Implications for composition of the core. Journal of Geophysical Research 95, 21737. doi:10.1029/JB095iB13p21737.

Mao, H.K., Xu, J., Bell, P.M., 1986. Calibration of the ruby pressure gauge to 800 kbar under quasi-hydrostatic conditions. Journal of Geophysical Research 91, 4673. doi:10.1029/JB091iB05p04673.

Mao, W.L., Campbell, A.J., Heinz, D.L., Shen, G., 2006. Phase relations of Fe–Ni alloys at high pressure and temperature. Physics of the Earth and Planetary Interiors 155, 146-151. doi:10.1016/j.pepi.2005.11.002.

Marchal, G., Mangin, P., Peicuch, M., Janot, C., Hubsch, J., 1977. Magnetic measurements on amorphous FeSi alloys. Journal of Physics F: Metal Physics 7, L165-L168. doi:10.1088/0305-4608/7/6/004.

Mathon, O., Baudelet, F., Itié, J., Polian, A., d'Astuto, M., Chervin, J., Pascarelli, S., 2004. Dynamics of the Magnetic and Structural α-ε Phase Transition in Iron. Physical Review Letters 93. doi:10.1103/PhysRevLett.93.255503.

Matsumoto, K., Maruyama, H., Ishimatsu, N., Kawamura, N., Mizumaki, M., Irifune, T., Sumiya, H., 2011. Noncollinear Spin Structure in Fe–Ni Invar Alloy Probed by Magnetic EXAFS at High Pressure. Journal of the Physical Society of Japan 80, 023709. doi:10.1143/jpsj.80.023709.

McDonough, W.F., Sun, S.s., 1995. The composition of the Earth. Chemical Geology 120, 223-253. doi:10.1016/0009-2541(94)00140-4.

Melchior, P., 1986. The Model of the Earth. 6-43. doi:10.1016/b978-0-08-032606-1.50006-3.

Merkel, S., 2000. Raman Spectroscopy of Iron to 152 Gigapascals: Implications for Earth's Inner Core. Science 288, 1626-1629. doi:10.1126/science.288.5471.1626.

Merkel, S., Goncharov, A.F., Mao, H.K., Gillet, P., Hemley, R.J., 2000. Raman Spectroscopy of Iron to 152 Gigapascals: Implications for Earth's Inner Core. Science 288, 1626-1629. doi:10.1126/science.288.5471.1626.

Monnereau, M., Calvet, M., Margerin, L., Souriau, A., 2010. Lopsided growth of Earth's inner core. Science 328, 1014-1017. doi:10.1126/science.1186212.

Monza, A., Meffre, A., Baudelet, F., Rueff, J.P., d'Astuto, M., Munsch, P., Huotari, S., Lachaize, S., Chaudret, B., Shukla, A., 2011. Iron Under Pressure: "Kohn Tweezers" and Remnant Magnetism. Physical Review Letters 106. doi:10.1103/PhysRevLett.106.247201.

Nasu, S., Sasaki, T., Kawakami, T., Tsutsui, T., Endo, S., 2002. Mössbauer study of -Fe under an external magnetic field. Journal of Physics: Condensed Matter 14, 11167-11171. doi:10.1088/0953-8984/14/44/446.

Nataf, L., Decremps, F., Chervin, J., Mathon, O., Pascarelli, S., Kamarád, J., Baudelet, F., Congeduti, A., Itié, J., 2009. High-pressure magnetic study of Fe-Ni and Fe-Pt Invar alloys. Physical Review B 80. doi:10.1103/PhysRevB.80.134404.

Ono, S., Kikegawa, T., Hirao, N., Mibe, K., 2010. High-pressure magnetic transition in hcp-Fe. American Mineralogist 95, 880-883.

Papandrew, A., Lucas, M., Stevens, R., Halevy, I., Fultz, B., Hu, M., Chow, P., Cohen, R., Somayazulu, M., 2006. Absence of Magnetism in Hcp Iron-Nickel at 11 K. Physical Review Letters 97. doi:10.1103/PhysRevLett.97.087202.

Patrick, L., 1954. The Change of Ferromagnetic Curie Points with Hydrostatic Pressure. Physical Review 93, 384-392. doi:10.1103/PhysRev.93.384.

Pipkorn, D., Edge, C., Debrunner, P., De Pasquali, G., Drickamer, H., Frauenfelder, H., 1964. Mössbauer Effect in Iron under Very High Pressure. Physical Review 135, A1604-A1612. doi:10.1103/PhysRev.135.A1604.

Poirier, J.-P., 1994. Light elements in the Earth's outer core: A critical review. Physics of the Earth and Planetary Interiors 85, 319-337. doi:10.1016/0031-9201(94)90120-1.

Reuter, K.B., Williams, D.B., Goldstein, J.I., 1989. Determination of the Fe−Ni phase diagram below 400°C. Metallurgical Transactions A 20, 719-725. doi:10.1007/bf02667589.

Ringwood, A.E., 1966. Chemical evolution of the terrestrial planets. Geochimica et Cosmochimica Acta 30, 41-104. doi:10.1016/0016-7037(66)90090-1.

Rueff, J., Shukla, A., Kaprolat, A., Krisch, M., Lorenzen, M., Sette, F., Verbeni, R., 2001. Magnetism of Invar alloys under pressure examined by inelastic x-ray scattering. Physical Review B 63, 13249. doi:10.1103/PhysRevB.63.132409.

Rueff, J.P., Mezouar, M., Acet, M., 2008. Short-range magnetic collapse of Fe under high pressure at high temperatures observed using x-ray emission spectroscopy. Physical Review B 78. doi:10.1103/PhysRevB.78.100405.

Schult, A., 1970. Effect of pressure on the Curie temperature of titanomagnetites [(1 − x) ·Fe3O4 − x ·TiFe2O4]. Earth and Planetary Science Letters 10, 81-86. doi:10.1016/0012-821x(70)90067-1.

Siegfried, R.W., Solomon, S.C., 1974. Mercury: Internal structure and thermal evolution. Icarus 23, 192-205. doi:10.1016/0019-1035(74)90005-0.

Sohl, F., Schubert, G., 2007. Interior Structure, Composition, and Mineralogy of the Terrestrial Planets. 27-68. doi:10.1016/b978-044452748-6.00153-x.

Steinle-Neumann, G., Stixrude, L., Cohen, R.E., 2004. Magnetism in dense hexagonal iron. Proceedings of the National Academy of Sciences of the United States of America 101, 33-36. doi:10.1073/pnas.2237239100.

Stevenson, D.J., 1981. Models of the Earth's Core. Science 214, 611-619. doi:10.1126/science.214.4521.611.

Stevenson, D.J., 2001. Mars: Core and Magnetism. doi:10.1888/0333750888/5455.

Swartzendruber, L.J., Itkin, V.P., Alcock, C.B., 1991. The Fe-Ni (iron-nickel) system. Journal of Phase Equilibria 12, 288-312. doi:10.1007/bf02649918.

Syassen, K., 2008. Ruby under pressure. High Pressure Research 28, 75-126. doi:10.1080/08957950802235640.

Syono, Y., 1965. Magnetocrystalline Anisotropy and Magnetostriction of Fe3O4-Fe2TiO4 Series with Special Application to Rock Magnetism. Jap. J. Geophys 4, 71–143.

Takahashi, T., Bassett, W.A., 1964. High-Pressure Polymorph of Iron. Science 145, 483-486. doi:10.1126/science.145.3631.483.

Tateno, S., Hirose, K., Komabayashi, T., Ozawa, H., Ohishi, Y., 2012. The structure of Fe-Ni alloy in Earth's inner core. Geophysical Research Letters 39, n/a-n/a. doi:10.1029/2012gl052103.

Tateno, S., Hirose, K., Ohishi, Y., Tatsumi, Y., 2010. The structure of iron in Earth's inner core. Science 330, 359-361. doi:10.1126/science.1194662.

Taylor, R.D., 1982. Internal magnetic fields in hcp-iron. Journal of Applied Physics 53, 8199. doi:10.1063/1.330289.

Taylor, R.D., Cort, G., Willis, J.O., 1982. Internal magnetic field in hcp-iron. J.Appl. Phys. 53, 8199-8201. doi:10.1063/1.330289.

Taylor, R.D., Pasternak, M.P., Jeanloz, R., 1991. Hysteresis in the high pressure transformation of bcc- to hcp-iron. Journal of Applied Physics 69, 6126. doi:10.1063/1.348779.

van Schilfgaarde, M., Abrikosov, I.A., Johansson, B., 1999. Origin of the Invar effect in iron–nickel alloys. Nature 400, 46-49. doi:10.1038/21848.

Vocadlo, L., 2013. Earth science: Core composition revealed. Nature 495, 177-178. doi:10.1038/495177a.

Von Barge, N., Boehler, R., 1990. Effect of non-hydrostaticity on the α-ε transition of iron. High Pressure Research 6, 133-140. doi:10.1080/08957959008203204.

Wang, F., Ingalls, R., 1998. Iron bcc-hcp transition: Local structure from x-ray-absorption fine structure. Physical Review B 57, 5647-5654. doi:10.1103/PhysRevB.57.5647.

Wanke, H., Dreibus, G., 1988. Chemical Composition and Accretion History of Terrestrial Planets. Philosophical Transactions of the Royal Society A: Mathematical, Physical and Engineering Sciences 325, 545-557. doi:10.1098/rsta.1988.0067.

Wei, Q., Gilder, S.A., 2013. Ferromagnetism of iron under pressure to 21.5 GPa. Geophysical Research Letters 40, 5131-5136. doi:10.1002/grl.51004.

Wei, Q., Gilder, S.A., Maier, B., 2014. Pressure dependence on the remanent magnetization of Fe-Ni alloys and Ni metal. Physical Review B 90. doi:10.1103/PhysRevB.90.144425.

Weiss, R.J., 1963. The Origin of the `Invar' Effect. Proceedings of the Physical Society 82, 281-288. doi:10.1088/0370-1328/82/2/314.

White, W.M., 2013. Blackwell-Wiley, Oxford, UK.

Wieczorek, M.A., 2006. The Constitution and Structure of the Lunar Interior. Reviews in Mineralogy and Geochemistry 60, 221-364. doi:10.2138/rmg.2006.60.3.

Xu, J.-a., Mao, H.-k., Hemley, R.J., Hines, E., 2002. The moissanite anvil cell: a new tool for high-pressure research. Journal of Physics: Condensed Matter 14, 11543-11548. doi:10.1088/0953-8984/14/44/513.